

2 Higgs pair production in the four bottom quarks final state

3

Ana Luísa Moreira de Carvalho

4

Thesis to obtain the Master of Science Degree in

5

Physics Engineering

6

Supervisor(s): Dr. José Ricardo Gonçalo
Prof. Pedro Abreu

7

Examination Committee

8

Chairperson: Prof. Full Name

Supervisor: Prof. Full Name 1 (or 2)

Member of the Committee: Prof. Full Name 3

9

Month Year

10 Acknowledgments

11 I would like to express my sincere thanks to my supervisor Ricardo Gonçalo for his support, invaluable
12 scientific advise and inspirational enthusiasm, without which this work would not have been concluded.

13 To my co-supervisor, Pedro Abreu, I thank for ...

14 I acknowledge the funding of this research by Fundação para a Ciência e Tecnologia - FCT, through

15 ...

16 I am very thankful to Patricia Conde and Rute Pedro for fruitful discussions and very helpful advise.

17 To my master colleagues in the LIP ATLAS group, Aidan Kelly, António Costa and Ricardo Barrué, I
18 thank for the companionship and motivation throughout this journey.

19 I am thankful to Duarte Azevedo, Pedro Ferreira and Rui Santos for being our on-call theoreticians,
20 always available to help.

21 I would like to thank all my colleagues in the LIP ATLAS group for making me feel very welcome.

22 I extend my gratitude to everybody at LIP for making it a fantastic place to work. I would also like to
23 acknowledge the LIP IT and secretariat for their patience and technical support.

24 I would like to thank my boyfriend, João Augusto, for his never ending patience and unconditional
25 support. To my friends of Chafarrica I express my most sincere thanks for always being a great support,
26 source of joy and laughter.

27 To my sister I thank for always welcoming me home with a smile, for the numerous time she offered
28 to help and for all the memes that lighten up some of my days.

29 To my parents, I will never be able to thank enough. I thank them for their love, unconditional support,
30 inspiration, help in times of need

Resumo

- ³¹ Inserir o resumo em Português aqui com o mximo de 250 palavras e acompanhado de 4 a 6 palavras-chave...

- ³⁴ **Palavras-chave:** palavra-chave1, palavra-chave2,...

35 **Abstract**

36 The production of pairs of Higgs bosons is a key benchmark process for future colliders because it
37 provides crucial insight into the Electroweak Symmetry Breaking mechanism but it is out of the current
38 reach of the Large Hadron Collider.

39 CERN is currently leading a study that analyzes the feasibility of a 100 km circular collider located
40 in the Geneva area. The hadronic Future Circular Collider (FCC-hh) is expected to work at a center of
41 mass energy of $\sqrt{s} = 100$ TeV and to collect a total integrated luminosity of $O(30)$ ab $^{-1}$.

42 This thesis describes a Monte Carlo study targeting the search for $hh \rightarrow b\bar{b}$ in a boosted kinematic
43 regime, using proton-proton collisions at center of mass energy of $\sqrt{s} = 100$ TeV. The focus is on the im-
44 pact of the granularity of hadronic calorimeter on the significance, S/\sqrt{B} , targeting detector optimization
45 studies for future colliders. In addition to traditional kinematic variables, jet substructure observables are
46 also explored.

47 For the FCC-hh, the achieved significance is $S/\sqrt{B} = \dots$ for an integrated luminosity of $\mathcal{L} = 30$ ab $^{-1}$,
48 which is above the 5σ threshold. When using particle flow jets, the significance changes very little over
49 the range of detector configurations considered. The change is more accentuated when using pure
50 calorimeter jets.

51 **Keywords:** keyword1, keyword2,...

Contents

53	Acknowledgments	iii
54	Resumo	iv
55	Abstract	v
56	List of Tables	xi
57	List of Figures	xiii
58	Glossary	xvi
59	1 Introduction	1
60	2 The standard model and beyond	4
61	2.1 The Standard Model of Particle Physics	4
62	2.1.1 Higgs pair production	10
63	2.2 Going beyond	13
64	3 Collider experiments	17
65	3.1 Experimental aspects	18
66	3.2 The Large Hadron Collider	18
67	3.2.1 The ATLAS detector	20
68	3.3 Jet reconstruction	23
69	3.3.1 Jet properties and substructure observables	25
70	3.3.2 Jet grooming algorithms	26
71	3.4 Future Colliders	27
72	3.4.1 The hadronic Future Circular Collider	27
73	3.4.2 FCC-hh baseline detector	28
74	3.4.3 FCC-hh physics program	29
75	4 State of the art	31
76	4.1 Searches for Higgs pair production at the LHC	31
77	4.2 Feasibility studies for high-luminosity and future colliders	33
78	4.3 Hadronic calorimeter granularity studies	34

79	5 Sample generation and analysis tools	38
80	5.1 Fast simulation workflow	38
81	5.1.1 Particle flow and calorimeter reconstruction in Delphes	39
82	5.1.2 FCC-hh software	40
83	5.2 Signal and background samples	41
84	5.2.1 MadGraph	41
85	5.2.2 Pythia	43
86	5.2.3 Delphes	44
87	6 Analysis	47
88	6.1 Overview of the $hh \rightarrow b\bar{b}b\bar{b}$ channel	47
89	6.1.1 Event pre-selection	47
90	6.1.2 Signal characterization	48
91	6.1.3 Backgrounds	49
92	6.2 Analysis strategy	53
93	6.2.1 Implementation of b-tagging	53
94	6.2.2 Baseline analysis	54
95	6.2.3 Optimization	55
96	6.2.4 Handling of uncertainties	59
97	7 Results	61
98	7.1 Di-Higgs discovery potential at the FCC-hh	61
99	7.1.1 Statistical analysis	62
100	7.1.2 Comparing with the ATLAS detector	62
101	7.2 Hadronic calorimeter granularity studies for future colliders	65
102	7.2.1 Resolution of jet mass and N-subjetiness	65
103	7.2.2 Signal efficiency and significance	66
104	8 Conclusions	71
105	Bibliography	73
106	A Jet radius discussion	81
107	B Additional background processes	82
108	C Softdrop mass	83
109	D Samples generation: parameters	84
110	D.1 MadGraph	84
111	D.2 Pythia	84
112	E Cutflow tables	86

List of Tables

114	3.1 ATLAS tile and liquid argon hadronic calorimeters: summary of the pseudorapidity coverages and transversal segmentation (granularity).	21
115	3.2 Comparison between the working parameters of the LHC and of the FCC-hh. The values of the number bunches and of the number of events per bunch crossing are given assuming a bunch spacing of 25 ns.	28
116	3.3 Hadronic calorimeter layout, granularity and energy resolution.	29
117	5.1 Summary of the effective cross sections ($\sigma \times BR$) and k factors of the signal and background samples used in the analysis.	45
118	5.2 Summary of the benchmark granularity configurations of the HCAL.	46
119	5.3 Summary of some key detector parameters for the FCC-hh and ATLAS detectors.	46
120	6.1 b-Tagging (black), c (blue) and light (red) mistag probabilities as a function of η and p_T of the (sub)jet. The momentum dependent factor, $(1 - p_T/15000)$, is common to the three probabilities.	54
121	7.1 Cumulative efficiency, in percentage, of each event selection criterion for the signal samples (SM and 2HDM). The absolute value of expected events after some key selection cuts is shown in curved brackets. The number of expected events is normalized to $\mathcal{L} = 30 \text{ ab}^{-1}$. The double horizontal line marks the pre-selection cuts. These results were obtained using the FCC-hh baseline detector design, as implemented in Delphes by the FCC-hh study group.	62
122	7.2 Cumulative efficiency, in percentage, of each event selection criterion for the background samples ($4b + j$, $jj + 0/1/2j$ and $t\bar{t}+0/1/2 j$). The absolute value of expected events after some key selection cuts is shown in curved brackets. The number of expected events is normalized to $\mathcal{L} = 30 \text{ ab}^{-1}$. The double horizontal line marks the pre-selection cuts. These results were obtained using the FCC-hh baseline detector design, as implemented in Delphes by the FCC-hh study group.	63

140	7.3 Cumulative efficiency, in percentage, of each event selection criterion for the signal sam-	
141	ples (SM and 2HDM). The absolute value of expected events after some key selection	
142	cuts is shown in curved brackets. The number of expected events is normalized to	
143	$\mathcal{L} = 30 \text{ ab}^{-1}$. The double horizontal line marks the pre-selection cuts. These results	
144	were obtained using the ATLAS detector design, as implemented in Delphes.	63
145	7.4 Cumulative efficiency, in percentage, of each event selection criterion for the background	
146	samples ($4b + j$, $jj + 0/1/2j$ and $t\bar{t}+0/1/2 j$). The absolute value of expected events after	
147	some key selection cuts is shown in curved brackets. The number of expected events	
148	is normalized to $\mathcal{L} = 30 \text{ ab}^{-1}$. The double horizontal line marks the pre-selection cuts.	
149	These results were obtained using the ATLAS detector design, as implemented in Delphes. 64	
150	7.5 Significances achieved with the ATLAS and FCC-hh detector configurations for $\mathcal{L} = 30 \text{ ab}^{-1}$	
151	for the three benchmark signal models: SM, 1 TeV DM mediator and 2HDM with $m_H = 900$	
152	GeV.	64
153	B.1 Effective cross section ($\sigma \times \text{BR} \times \text{k-factor}$), efficiency and expected number of events for	
154	$\mathcal{L} = 30 \text{ ab}^{-1}$ for the $t\bar{t}h + 0/1 j(h \rightarrow b\bar{b})$ and $h + 0/1/2 j(h \rightarrow b\bar{b})$ backgrounds.	82
155	D.1 Generator (MadGraph5) level cuts for the signal and background samples.	85
156	D.2 Pythia settings for the signal and background samples.	85
157	E.1 oi	86
158	E.2 oi	87

¹⁵⁹ List of Figures

160	2.1 Schematic representation of the Standard Model of elementary particles. Particle are 161 represented inside squares. The electric and color charge are shown in the right upper 162 corner of each square. The spin is shown in the right lower corner. The mass of the 163 particles is also shown, in electron Volt.	5
164	2.2 Postulated shape of the Higgs potential for $\mu^2 > 0$ (left) and $\mu^2 < 0$ (right).	8
165	2.3 Feynman diagrams of Higgs pair production from gluon fusion. Triple vertex diagram 166 (left) and box diagram (right). The minus sign between the diagrams indicates that they 167 interfere destructively.	11
168	2.4 Total cross sections at the NLO in QCD for the six largest HH production channels at 169 pp colliders. The thickness of the lines corresponds to the scale and PDF uncertainties 170 added linearly.	13
171	2.5 Here, α_1 , α_2 and α_3 represent the coupling constants of $U(1)$, $SU(2)$ and $SU(3)$, respec- 172 tively. What is shown is the variation of the inverse of the coupling with the energy: on the 173 left for the SM and on the right for the MSSM. Plots from [23].	14
174	2.6 BSM contributions to Higgs pair production from the spin-2 Kaluza-Klein graviton (a) and 175 from the SUSY partner of the top quark (b). Figures from Refs. [26, 27].	16
176	3.1 ATLAS detector.	22
177	3.2 FCC detector baseline concept.	30
178	4.1 Exclusion limits (at 95% CL) on the cross section of resonant Higgs pair production from 179 the decay of heavy scalar particles. These results were obtained using proton-proton 180 collision data collected with the CMS (a) and ATLAS (b) detector at a CM energy of $\sqrt{s} = 8$ 181 TeV and result from the combination of different channels. Plots from [70] and [74].	33
182	4.2 Azimuthal distribution of the energy deposits in the ECAL and HCAL for a pair of K_L^0 with 183 $E = 100$ GeV for an hadronic calorimeter with $20 \text{ cm} \times 20 \text{ cm}$ (a) and $5 \text{ cm} \times 5 \text{ cm}$ (b). 184 Figures from [79] (based on [78]).	35
185	4.3 Jet mass (a) and jet mass resolution (b) plots in $t\bar{t}$ events for eflow jets with $p_T > 3$ TeV for 186 three different HCAL and ECAL configurations: HCAL(ECAL) 0.1(0.025) $\eta \times 5.6(1.4)$ deg ϕ , 187 HCAL(ECAL) 0.05(0.012) $\eta \times 2.8(0.7)$ deg ϕ and HCAL(ECAL) 0.025(0.006) $\eta \times 1.4(0.35)$ deg ϕ . 188 Plots from Ref. [79].	36

189	4.4	τ_{32} resolution plots for QCD dijet events reconstructed using eflow jets (a) and tower jets (b). Plots from Ref. [80].	37
190			
191	4.5	τ_{21} variable for 20 TeV W (black) and QCD jets (red) for three HCAL granularities: $\Delta\eta \times \Delta\phi = 0.1 \times 0.1$ (left), $\Delta\eta \times \Delta\phi = 0.022 \times 0.022$ (middle) and $\Delta\eta \times \Delta\phi = 0.005 \times 0.005$ (right). Plots from Ref. [79].	37
192			
193			
194	6.1	Higgs pairs branching ratios (left) and event topology targeted by this analysis (right).	48
195	6.2	$\Delta\phi$ between the Higgs candidates, $\Delta\phi(hh)$, (left) and ΔR between the b quarks coming from the decay of the leading Higgs candidate, h_1 (right). To obtain this plot the cut $ M - 125 < 40$ GeV was applied in addition to the pre-selection cuts..	50
196			
197	6.3	Example of diagrams that contribute to the QCD multijet background: five final state jets, four of which are b-jets (left), three final state jets (middle) and four final state jets (right). Here, q stands for a light quark/jet.	51
198			
199	6.4	Dominant diagrams of $pp \rightarrow t\bar{t}$ at LO.	51
200			
201	6.5	p_T distributions for the leading (left) and sub leading (right) Higgs candidates. The signal is the SM $hh \rightarrow b\bar{b}$ process. The histograms are normalized to unit area.	52
202			
203	6.6	η distribution for the leading Higgs candidate (left) and softdrop mass distribution for the leading Higgs candidate (right). The signal is the SM $hh \rightarrow b\bar{b}$ process. The histograms are normalized to unit area.	52
204			
205	6.7	Distributions of the $\Delta\eta$ between the Higgs candidates (left) and of the τ_{21} variable for the leading Higgs candidate (right). The histograms are normalized to unit area.	52
206			
207	6.8	Minimun ΔR between b quarks and subjets of the $R = 0.8$ jets.	53
208			
209	6.9	p_T distributions for the leading (a) and sub leading Higgs candidates (b). The histograms are normalized to $\mathcal{L} = 30 \text{ ab}^{-1}$	55
210			
211	6.10	(a) p_T distribution for the Higgs pair, (b) τ_{21} variable for the leading Higgs candidate. The histograms are normalized to $\mathcal{L} = 30 \text{ ab}^{-1}$	56
212			
213	6.11	(a) H_2 variable for the leading Higgs candidate, (b) softdrop mass distribution for the leading Higgs candidate. The histograms are normalized to $\mathcal{L} = 30 \text{ ab}^{-1}$	56
214			
215	6.12	S/\sqrt{B} as a function of the cut on the p_T of the leading Higgs candidate, $p_T(h_1)$ (left) after the pre-selection cuts and of the sub leading Higgs candidate, $p_T(h_2)$ (right) after the cut on $p_T(h_1)$	58
216			
217	6.13	S/\sqrt{B} as a function of the cut on the p_T of the Higgs pair, $p_T(hh)$ (left) after the cut on $p_T(h_1)$ and as a function of the τ_{21} variable for leading Higgs candidate, $\tau_{21}(h_1)$ (right) after the cut on $p_T(hh)$	58
218			
219	6.14	S/\sqrt{B} as a function of the cut on the $\Delta\eta$ between the Higgs candidates, $\Delta\eta(hh)$ (left) after the cuts on the transverse momentums and on the τ_{21} variables and as a function of the second Fox-Wolfram momentum for the leading Higgs candidate, $H_l(h_1)$ (right) after the cuts on the transverse momentums, τ_{21} and $\Delta\eta$	58
220			
221			
222			
223			
224			
225			

226	7.1	Leading Higgs candidate softdrop mass after the pre-selection cuts for particle flow (a)				
227		and calorimeter (b) jets. The colors indicate the different detector configurations. The				
228		x axis range is from 80 GeV to 160 GeV in order to make the differences between the				
229		histograms more clear.				67
230	7.2	Invariant mass of the Higgs pair for the SM signal. The plots include the events that pass				
231		all the analysis cuts. The colors indicate the different detector configurations.				67
232	7.3	(a) Invariant mass of the Higgs pair for the 1 TeV DM mediator, (b) Invariant mass of the				
233		Higgs pair for the 2HDM with $m_H = 900$ GeV. The plots include the events that pass all				
234		the analysis cuts. The colors indicate the different detector configurations.				68
235	7.4	(a) Leading Higgs candidate τ_{21} distribution for eflow jets, (b) Leading Higgs candidate τ_{21}				
236		distribution for HCAL jets. The colors indicate the different detector configurations. The				
237		distributions are shown for the signal (filled lines) and for the $4b + j$ background (dashed				
238		lines).				68
239	7.5	(a) Signal efficiency as a function of the detector configuration for particle flow jets, (b)				
240		Signal efficiency as a function of the detector configuration for calorimeter jets. Three				
241		signal models are shown: SM (filled squares), 1 TeV DM mediator (empty squares) and				
242		type II 2HDM with $m_H = 900$ GeV (crosses). The error bars are drawn but are smaller				
243		than the markers.				69
244	7.6	Significance as a function of the detector configuration for the SM signal, for the baseline				
245		(a) and optimized (b) analyses. The significances are shown for eflow jets (squares) and				
246		pure HCAL jets (triangles).				69
247	7.7	Significance as a function of the detector configuration for the DM mediator signal, for				
248		the baseline (a) and optimized (b) analyses. The significances are shown for eflow jets				
249		(squares) and pure HCAL jets (triangles).				70
250	7.8	Significance as a function of the detector configuration for the 2HDM signal, for the base-				
251		line (a) and optimized (b) analyses. The significances are shown for eflow jets (squares)				
252		and pure HCAL jets (triangles).				70
253	A.1	$\Delta R(b, \bar{b})$ distributions for $p_T(h_1) > 200/300$ GeV (solid blue/black) and for $p_T(h_1, h_2) >$				
254		200/300 GeV (dashed blue/black).				81
255	C.1	Correlation between the maximum ΔR between the Higgs candidate jet and one of the b				
256		quarks (y axis) and the jet's mass (x axis). The horizontal line corresponds to $\Delta R = 0.8$. .				83
257	F.1	. The histograms are normalized to $\mathcal{L} = 30 \text{ ab}^{-1}$				89

Glossary

2HDM	Two Higgs Doublet Model
ATLAS	A Toroidal LHC Apparatus
BR	Branching Ratio
BSM	Beyond the Standard Model
CERN	European Organization for Nuclear Research
CMS	Compact Muon Solenoid
ECAL	Electromagnetic Calorimeter
EM	Electromagnetic
HCAL	Hadronic Calorimeter
ID	Inner Detector
LHC	Large Hadron Collider
LO	Leading Order
NLO	Next to Leading Order
QCD	Quantum Chromodynamics
QED	Quantum Electrodynamics
QFT	Quantum Field Theory
SM	Standard Model
SUSY	Super Symmetry
TileCal	Tile Calorimeter
VEV	Vacuum Expectation Value

259 **Chapter 1**

260 **Introduction**

261 It is the ultimate goal of particle physics to discover and study all of Nature's fundamental particles and
262 to understand their interactions. Through a joint endeavor of theorists and experimentalists, models that
263 describe particle's dynamics and properties can be precisely probed at collider experiments such as the
264 Large Hadron Collider (LHC).

265 We know today that matter particles interact by means of four fundamental forces: electromagnetic,
266 weak, strong and gravitational, each associated with a mediator particle. We even know that a very
267 special particle, the Higgs boson, is responsible for generating the mass of these particles through
268 a mechanism called Electroweak Symmetry Breaking (EWSB). Through Yukawa couplings, the Higgs
269 boson is also responsible for the masses of matter particles. This knowledge is beautifully summarized
270 in the Standard Model of Particle Physics (SM) that was developed in the 1960's, long before many of
271 the particles it predicts were discovered. The extraordinary precision of the predictions it delivers make
272 it a very successful model. Its most recent prediction, the Higgs boson, was discovered in 2012 at
273 the LHC which marks an important point in the history of particle physics: we have now found all the
274 particles predicted by the SM and yet we know that it cannot be the whole story. Mainly because there
275 are experimental evidences of physics that it cannot explain.

276 From the theoretical point of view, this is enough motivation to construct models that extend the SM
277 but that can still deliver predictions that are compatible with experimental data. From the experimental
278 standpoint, this is an indication that we need to keep increasing the precision of our measurements and
279 probing new kinematic regimes in the hope of finding some discrepancy with the SM or some hint that
280 some new phenomenon might be taking place.

281 A higher precision requires a larger integrated luminosity and the exploration of new kinematic
282 regimes asks for a larger center of mass energy. Very recently, work towards the upgrade of the LHC to
283 its High-Luminosity (HL) version has began. It is expected to work for a period of ten years between 2026
284 and 2036 and it will extend the experimental reach of the LHC. In order to keep extending the physics
285 reach of the LHC and HL-LHC, new colliders with unprecedentedly high center of mass (CM) energies
286 are currently being designed in the hope that they begin to deliver data shortly after the HL-LHC has
287 reached its full discovery potential. One of these projects is the hadronic Future Circular Collider (FCC-

288 hh) that consists of a 100 km ring located in the Geneva area and it is expected to work at a CM energy
289 of 100 TeV. The FCC-hh will deliver a peak luminosity of $\mathcal{L} = 30 \times 10^{34} \text{ cm}^{-2}\text{s}^{-1}$ in its ultimate phase.
290 This will result in $O(30) \text{ ab}^{-1}$ per experiment which corresponds to ten times the expected integrated
291 luminosity by the end of the HL-LHC operation.

292 The next milestone for the FCC-hh project is the submission of a Conceptual Design Report by the
293 end of 2018. This document will be used as input for the next meeting of the European Strategy for
294 Particle Physics that will take place in the beginning of 2019. It should present a baseline design for the
295 detector, a first cost estimate and preliminary analysis for physics benchmark processes demonstrating
296 the physics reach of such a machine.

297 Both in the HL-LHC and in future colliders, one of the most important benchmark processes is the
298 production of pairs of Higgs bosons. Firstly, this process is predicted by the SM but has not yet been
299 measured which is due to its very small cross section and overwhelming backgrounds. Furthermore,
300 it provides unique insight into the EWSB mechanism because it is sensitive to the shape of the Higgs
301 potential and can also be used to probe physics beyond the SM (BSM).

302 In this work we study Higgs pair production at a center of mass energy of $\sqrt{s} = 100 \text{ TeV}$ using the
303 final state with four b quarks. We choose this final state because it benefits from the large branching frac-
304 tion of the Higgs boson to a pair of b quarks. However, in this channel, the multijet production through
305 Quantum Chromodynamics (QCD) interactions is extremely overwhelming. Nonetheless, it is a well
306 known feature of QCD interactions that the partons (and jets) produced tend to have a low transverse
307 momentum (p_T). This indicates that exploring a high p_T region of the phase space could be the key to
308 suppress this background. In this kinematic regime, traditional jet reconstruction techniques, that estab-
309 lish a one-to-one correspondence between partons and jets, begin to fail because the decay products
310 of heavy, highly boosted particle become more collimated as the p_T of the mother particle increases.
311 State of the art jet reconstruction techniques make use of jets with a larger radius parameter to recon-
312 struct both decay products as a single jet that can then be used as a proxy for the original particle. In
313 order to recover as much information as possible from these jets, it is important to analyze their intrinsic
314 structure, referred to as substructure.

315 Jet substructure techniques explore the existence of subjets inside the large- R jets. For example, a
316 jet containing the two b quarks from the decay of a Higgs boson is expected to be more consistent with
317 having two subjets than a jet produced by a QCD process. From the standpoint of detector design for
318 the FCC-hh, as well as future upgrades of existent detectors, the ability to resolve the substructure of
319 large- R jets is a key requirement that is greatly influenced by the granularity of the hadronic calorimeter
320 (HCAL).

321 The main goal of this thesis is to use boosted di-Higgs production in the four b quarks final state to
322 study the influence of the granularity of the HCAL in the significance that can be achieved.

323 Chapter 2 presents an overview of the SM. It summarizes its particle content and interactions and
324 introduces the mathematical formulation of the EWSB breaking mechanism. The successes and short-
325 comings of the SM are presented and several BSM models are introduced and their motivations dis-
326 cussed. Finally, a theoretical description of the production of Higgs pairs is provided.

327 The FCC-hh baseline accelerator and detector were highly based on LHC and its current experiments,
328 namely ATLAS and CMS. In chapter 3, after a brief discussion of the general features of particle
329 accelerators, we introduce the LHC and the ATLAS experiment. A discussion of jet reconstruction is
330 included. We then introduce the FCC-hh accelerator and its current baseline detector design. Some key
331 detector parameters are compared to ATLAS.

332 In chapter 4 we present the state of the art of searches for Higgs pair production at the LHC and
333 of feasibility studies targeting searches for this process at future colliders (High Luminosity LHC and
334 FCC-hh). We also review previous studies that focus on the impact of the HCAL granularity on the jet
335 mass and jet substructure observables resolution.

336 In chapter 5 we describe in detail the Monte Carlo samples that were used in this work. In addition,
337 the different detector configurations that were tested are described. Chapter 6 entails the description
338 of the analysis strategy and its optimization. A comprehensive characterization of the signal and back-
339 grounds processes is provided.

340 In chapter 7 we present and discuss the main results. We focus on the resolution of the jet mass
341 and of the ratio of N-subjetiness variables, namely, τ_{21} . In addition, we analyze how the significance
342 chances as the granularity of the HCAL is varied. The results obtained using particle flow jets and pure
343 calorimeter jets are compared.

344 Finally, conclusions are drawn in chapter 8.

345 **Chapter 2**

346 **The standard model and beyond**

347 The Standard Model (SM) is the theoretical framework that summarizes our present knowledge of particle physics. In section 2.1, we provide an overview of this model, focusing on the Higgs mechanism. In 348 section 2.2, we motivate the need to explore models beyond the SM (BSM) and introduce some of the 349 most well known BSM models. In section 2.1.1, we provide a theoretical description of the production of 350 Higgs boson pairs which is the physical process that is under study throughout this work.

352 **2.1 The Standard Model of Particle Physics**

353 The Standard Model of particle physics summarizes our present knowledge of fundamental particles 354 and their interactions. It is formulated in the framework of Quantum Field Theory (QFT) and describes 355 the subatomic world in terms of fields whose excitations are the particles we can detect. The particle 356 content of the SM is summarized in figure 2.1. Each particle is represented inside a square. The electric 357 and color charge are shown in the right upper corner and the spin in the right lower corner. The mass 358 of the particles are given in electron Volt on top of each square. There are two types of fundamental 359 particles: matter particles and force carriers.

360 Matter particles are the building blocks of all the matter in our world. They come in two groups, 361 leptons and quarks. Quarks make up atomic nuclei and leptons, namely electrons and muons, can 362 orbit atomic nuclei forming atoms. Quarks and leptons are fermions which means they have half-integer 363 spin. There are six quarks: three of the 'up type' (up, charm and top represented by u , d and t) with 364 electric charge of $+2/3$ and three of 'down type' (down, strange and bottom represented by d , s and b) 365 with electric charge of $-1/3$. Similarly, we have three leptons with charge -1 (electron, muon and tau 366 represented by e , μ and τ) and three neutral leptons (electron, muon and tau neutrinos represented by 367 ν with the symbol of the corresponding charged lepton as subscript) that are, within the SM, massless. 368 We can classify quarks and leptons in three generations, each composed of an up type and down type 369 quark or of a charged lepton and the corresponding neutrino.

370 The force carriers, technically called gauge bosons, are particles associated with the fundamental

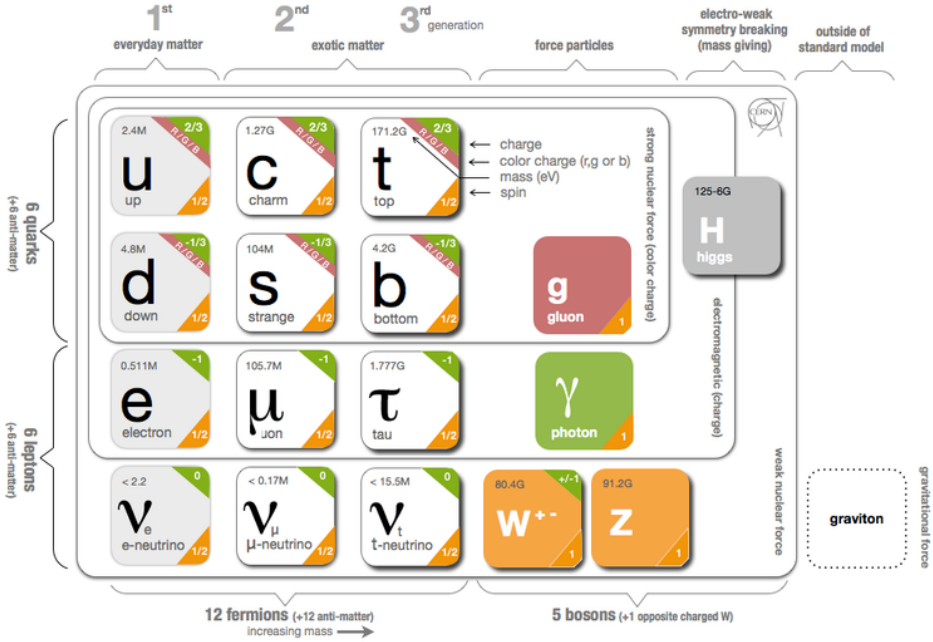


Figure 2.1: Schematic representation of the Standard Model of elementary particles. Particle are represented inside squares. The electric and color charge are shown in the right upper corner of each square. The spin is shown in the right lower corner. The mass of the particles is also shown, in electron Volt.

interactions: strong, electromagnetic, weak and gravitational ¹. Each interaction can be interpreted as the result of the exchange of the corresponding gauge boson. Gluons (g) and photons (γ) are the mediators of the strong and electromagnetic interactions, respectively. They are massless, electrically neutral and have spin 1. The W^+ , W^- and Z bosons are the mediators of the weak interaction and have a mass of 82 and 91 GeV, respectively. The W^+ and W^- bosons have electric charges of +1 and -1, respectively and spin 1. The Z boson is electrically neutral and also has spin 1. The gauge bosons can also be referred to as vector bosons because they have spin equal to one.

In addition to matter particles and gauge bosons, the theoretical formulation of the SM rests on the existence of the Higgs boson that is an electrically neutral and spin 0 particle. It has a mass of 125 GeV and it interacts with every particle that has mass.

Historically, an empirically successful quantum theory of electromagnetism, Quantum Electrodynamics (QED), was developed in the late 1940's. In the early 1950's there were high hopes that quantum theories could also be formulated for the weak and strong interactions. This is the context in which Yang-Mills theories emerged. They extend the concept of gauge theory from abelian groups, that lead to the development of QED, to non-abelian gauge groups. However, the quanta of the fields predicted by these theories must be massless in order to maintain gauge invariance. Therefore, they were set aside until the 1960's when the idea of particles acquiring mass through symmetry breaking in massless theories was put forward by Goldstone [1], Nambu and Jona-Lasinio [2]. In the following paragraphs we discuss in more detail the caveats of Yang-Mills theories and the phenomenon of Spontaneous Symmetry

¹ The gauge boson that corresponds to the gravitational force has not yet been found. In addition we still do not have a theory that successfully describes gravitation in the framework of QFT so we will not include the gravitational force or its gauge boson in any of the following discussions.

try Breaking (SSB) as the basis of the modern Higgs mechanism. We then describe this mechanism in the framework of the SM.

On the one hand, if one takes a Yang-Mills theory, it becomes clear that it is not possible to include in the Lagrangian a mass term for the gauge bosons because it is not invariant under a gauge transformation. This would not be a problem if we just wanted to describe electromagnetic or strong interactions because the gauge bosons associated with these interactions, the photon and the gluon, are indeed massless. However, for the weak interactions this is not the case. Even before the discovery of the Z and W^\pm bosons [3, 4] there were experimental evidence of the short range character of the weak interactions which indicated that the corresponding gauge bosons should be massive.

On the other hand, spontaneous symmetry breaking (SSB) is a phenomenon through which the invariance of a system under a certain symmetry group is destroyed [5]. The system may then be invariant under a subgroup of the initial symmetry but the invariance under the original symmetry group is no longer present. In particle physics, this happens because the vacuum of the system (lowest energy states) does not share the symmetry of the Lagrangian. The SSB mechanism predicts the existence of scalar massless particles, the Nambu-Goldstone bosons, as a consequence of the Goldstone theorem [1] (the number depends on the number of generators of the original and final symmetry groups). Though, when considering this mechanism we get once again massless particles which does not seem to be a step in the right direction if we wish to describe weak interactions.

However, the real breakthrough occurs when we combine a theory with local gauge invariance with the mechanism of SSB. In this case the Nambu-Goldstone bosons do not appear and it is possible to give mass to the gauge bosons. This is the Higgs mechanism, proposed independently by P.W. Higgs [6], F. Englert and R. Brout [7] and by G. Guralnik, C. R. Hagen and T. Kibble [8] in 1964.

The SM is a non-abelian gauge theory with spontaneous symmetry breaking. It is locally invariant under the following symmetry group:

$$SU_{color}(3) \times SU_L(2) \times U_Y(1), \quad (2.1)$$

where the $SU_{color}(3)$ group describes the strong interactions (QCD) and the $SU_L(2) \times U_Y(1)$ group describes the electroweak interactions. Here, L stands for left and Y stands for hypercharge. In the SM the Higgs mechanism, which we now describe, is realized in the $SU_L(2) \times U_Y(1)$ group. The Lagrangian corresponding to the Higgs and gauge sectors of this theory is given by:

$$\mathcal{L} = (D_\mu \phi)^\dagger (D^\mu \phi) - V(\phi^\dagger \phi) - \frac{1}{4} W_{\mu\nu}^a W^{a\mu\nu} - \frac{1}{4} B_{\mu\nu} B^{\mu\nu}, \quad (2.2)$$

where the Higgs potential, $V(\phi^\dagger \phi)$, is given by:

$$V(\phi^\dagger \phi) = \mu^2 \phi^\dagger \phi + \lambda (\phi^\dagger \phi)^2. \quad (2.3)$$

$W_{\mu\nu}^a$ and $B_{\mu\nu}$ are the field tensors, defined as a function of the gauge fields of $SU(2)$ and $U(1)$, respectively, W_μ^a ($a = 1, 2, 3$) and B_μ :

$$W_{\mu\nu}^a = \partial_\mu W_\nu^a - \partial_\nu W_\mu^a - g\epsilon^{abc}W_\mu^b W_\nu^c \quad (2.4)$$

$$B_{\mu\nu} = \partial_\mu B_\nu - \partial_\nu B_\mu \quad (2.5)$$

420 where g is the coupling constant associated with the $SU(2)$ group and ϵ^{abc} is the completely anti-
 421 symmetric tensor in 3 dimensions. The covariant derivative, D_μ , is introduced to preserve local gauge
 422 invariance and is given by:

$$D_\mu \phi = \left(\partial_\mu + igW_\mu^a T^a + i\frac{g'}{2} B_\mu \right) \phi. \quad (2.6)$$

423 $T^a = \frac{\tau^a}{2}$ (where τ^a are the Pauli matrices) are the $SU(2)$ group generators in the fundamental representation
 424 and g' is the coupling constant associated with the $U(1)$ group.

Due to the requirement of Lorentz invariance, only the scalar field, ϕ , can have a vacuum expectation value (VEV), v , different from zero². The values of v are determined by the minima of the potential:

$$v = 0 \quad \text{or} \quad v = \sqrt{\frac{-\mu^2}{2\lambda}}. \quad (2.7)$$

425 For the equation on the right (for which we get $v \neq 0$) we only obtain a real value for v (which is a
 426 requirement for the VEV of a theory) if $\mu^2 < 0$. Therefore we conclude that the equation on the right
 427 corresponds to $\mu^2 \leq 0$ while the equation on the left corresponds to $\mu^2 \geq 0$. In both cases λ has to
 428 be larger than zero to guarantee that the energy is bounded from below³ because in Eq. 2.3 λ is the
 429 coefficient of the term with the highest power in ϕ and therefore determines the concavity of the potential.

430 The shapes of the Higgs potential for $\mu^2 > 0$ and $\mu^2 < 0$ are shown in Figures 2.2(a) and 2.2(b),
 431 respectively. For $\mu^2 > 0$ (left) we have a single minimum located at $\langle\phi\rangle = 0$. For $\mu^2 < 0$ (right)
 432 the potential has the shape of a 'Mexican hat'. There is an infinite number of minima located in a
 433 circumference centered at zero. In this case the minima occur for $\langle\phi\rangle, \langle\phi^\dagger\rangle \neq 0$. Therefore the fields
 434 acquire a VEV different than zero and this what leads to the SSB.

We can now write the scalar field in terms of its minimum value, v , and of oscillations around that minimum, h (which corresponds to the Higgs field):

$$\phi = \begin{bmatrix} 0 \\ v + \frac{h}{\sqrt{2}} \end{bmatrix} \quad (\text{unitary gauge}). \quad (2.8)$$

435 If we expand the first term of the Lagrangian shown in Eq. 2.2 using Eq. 2.6 and Eq. 2.8 and taking into
 436 consideration that $W_\mu^a T^a$ represents a sum over all values of a we get

²The other fields that appear in Eq. 2.2 are vector fields. If they were to acquire a VEV different from zero that would break Lorentz invariance.

³In a purely mathematical formulation this means that the function that represents the Higgs potential is concave upwards.

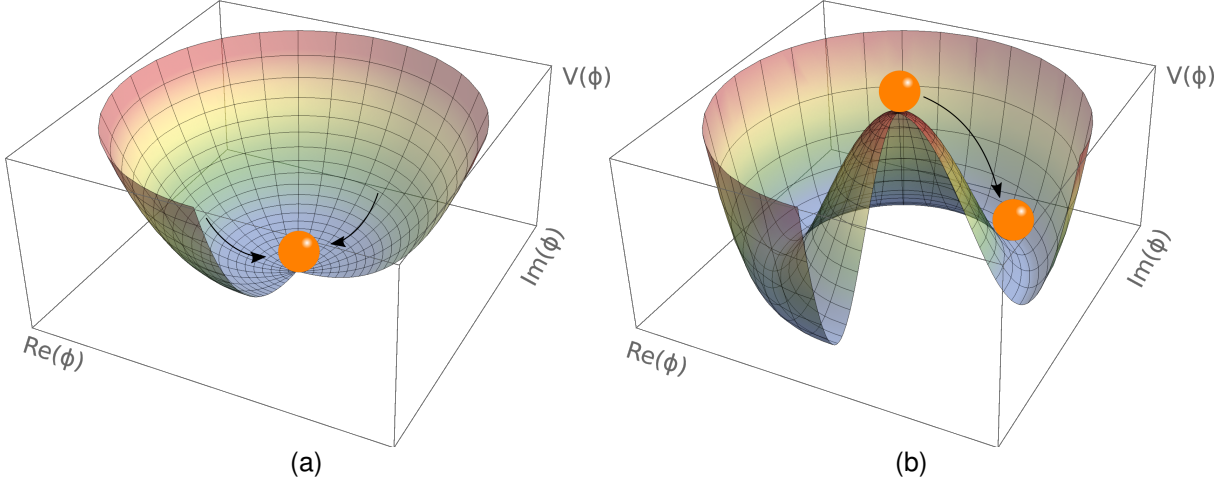


Figure 2.2: Postulated shape of the Higgs potential for $\mu^2 > 0$ (left) and $\mu^2 < 0$ (right).

$$\mathcal{L} = \frac{1}{4} \left(v^2 + \frac{h^2}{2} + \frac{2}{\sqrt{2}} vh \right) [g^2 (W_\mu^1 W^{1\mu} + W_\mu^2 W^{2\mu} + W_\mu^3 W^{3\mu}) - 2gg' B^\mu W_\mu^3 + g'^2 B_\mu B^\mu] + \dots . \quad (2.9)$$

We see that for the W_μ^1 and W_μ^2 fields we have only terms that are quadratic in these fields. These correspond to mass terms. However, for the W_μ^3 and B_μ fields there is a term that mixes the two fields. To obtain the physical states of the theory we need to transform these fields in order to get rid of the mixing term which is not physical. We can start by writing the last three terms of Eq. 2.9 in a matrix form and diagonalize the corresponding matrix:

$$\begin{bmatrix} g^2 & -gg' \\ -gg' & g'^2 \end{bmatrix} \begin{bmatrix} W_\mu^3 \\ B_\mu \end{bmatrix} \xrightarrow{\text{Diagonalization}} \begin{bmatrix} 0 & 0 \\ 0 & g^2 + g'^2 \end{bmatrix} \begin{bmatrix} A_\mu \\ Z_\mu \end{bmatrix}. \quad (2.10)$$

A_μ and Z_μ are the physical fields that are related with W_μ^3 and B_μ by means of a rotation matrix:

$$\begin{bmatrix} A_\mu \\ Z_\mu \end{bmatrix} = \begin{bmatrix} \cos \theta_W & -\sin \theta_W \\ \sin \theta_W & \cos \theta_W \end{bmatrix} \begin{bmatrix} W_\mu^3 \\ B_\mu \end{bmatrix} \quad (2.11)$$

where θ_W is the Weinberg angle. By inverting this relation we can write W_μ^3 and B_μ as a function of A_μ and Z_μ . Replacing in Eq. 2.9 and imposing that the A_μ field has zero mass we can determine θ_W : $\tan \theta_W = \frac{g'}{g}$. The Lagrangian of Eq. 2.9 takes then the form

$$\mathcal{L} = \frac{1}{2} (v^2 g^2) (W_\mu^1 W^{1\mu} + W_\mu^2 W^{2\mu}) + \frac{1}{2} (v^2 [g^2 + g'^2]) Z_\mu Z^\mu + \dots \quad (2.12)$$

⁴³⁷ where we show only the mass terms for the gauge bosons. Note that, by construction, there is no mass term for A_μ which allows us to identify this field with the photon. W_μ^1 and W_μ^2 are related to the W^\pm boson and Z_μ corresponds to the Z boson. We have shown that it is the fact that $v \neq 0$ that allows for ⁴⁴⁰ the existence of non-zero mass terms for the W^\pm and Z bosons.

If we now expand the second term of the Higgs potential (Eq. 2.3) using Eq. 2.8 we get, among other terms,

$$\mathcal{L} = -h^3 \sqrt{-\mu^2 \lambda} - h^4 \lambda + \dots . \quad (2.13)$$

441 These terms encode the Higgs self interactions and represent, respectively, the three and four point
442 interactions. We see that the coupling constants of these interactions depend on the parameters of the
443 Higgs potential, μ^2 and λ .

444 In addition to being responsible for giving mass to the gauge bosons, the Higgs field is also responsible
445 for the mass of the fermions. However, the mechanism through which this occurs is fundamentally
446 different. In the case of the leptons the mass terms are placed explicitly in the Lagrangian:

$$\mathcal{L}_{\text{fermions}} = G_1 \bar{L} \phi R + G_2 \bar{L} \phi_c R + \text{hermitian conjugate} \quad (2.14)$$

447 where L denotes a left-handed fermion doublet and R denotes a right-handed fermion singlet. Here,
448 left and right refer to helicity states. G_1 and G_2 are arbitrary coupling constants that can be written in
449 terms of the fermion's mass and the VEV. ϕ is given by Eq. 2.8 and ϕ_c is given by (after the spontaneous
450 symmetry breaking and in the unitary gauge):

$$\phi_c = \begin{bmatrix} v + \frac{h}{\sqrt{2}} \\ 0 \end{bmatrix}. \quad (2.15)$$

We now take a quick detour to motivate why fermions are represented as chiral states (left and right) of the $SU(2)$ symmetry. We base this discussion on [9]. In the context of the unification of the electromagnetic and weak forces, formalized by Weinberg, Glashow and Salam in 1960, both interactions are interpreted as manifestations of the electroweak force. Weak charged currents are axial vector currents which means they couple only to left handed fermions while weak neutral currents, as well as QED, couple to both helicity states. This suggested that fermions were better represented as left-handed doublets and right-handed singlets of the $SU(2)$ symmetry group. The left handed doublets, L , are defined as:

$$L : \begin{pmatrix} \nu_l \\ l \end{pmatrix}_L, \begin{pmatrix} u \\ d' \end{pmatrix}_L \quad (2.16)$$

where l represents an electron, muon or tau, u is any quark of the up type and d' is a quark of the down type. The right-handed states, R , are singlets, define as:

$$R : l_R, u_R, d'_R. \quad (2.17)$$

451 In 1956, C. S. Wu *et al.* showed that the weak interaction violates parity conservation [10]. In 1958, M.
452 Goldhaber *et al.* conducted an experiment that showed that neutrinos are left-handed and anti-neutrinos
453 are right-handed [11] which is why the SM does not include a right-handed state for neutrinos. We can
454 now continue the discussion of the mass generation mechanism for fermions.

455 The first term in Eq. 2.14 gives mass to down type fermions (electron, muon, tau, down, strange

456 and bottom quarks) and the second to up type fermions (up, charm and top quarks). In addition, these
 457 terms give rise to the interaction terms between the Higgs field and the fermions. Take, as an example,
 458 $\bar{L} = (\bar{t}, \bar{b})_L$ and $R = b_R$. For the first term of Eq. 2.14 we get:

$$G_1 \bar{L} \phi R = G_1 (\bar{t}, \bar{b})_L \begin{bmatrix} 0 \\ v + \frac{h}{\sqrt{2}} \end{bmatrix} b_R = G_1 v \bar{b}_L b_R + \frac{G_1}{\sqrt{2}} \bar{b}_L b_R h. \quad (2.18)$$

The first term is the mass term for b quarks. Therefore we can redefine $G_1 v = m_b$ and obtain:

$$G_1 \bar{L} \phi R = m_b \bar{b}_L b_R + \frac{m_b}{v \sqrt{2}} \bar{b}_L b_R h. \quad (2.19)$$

459 The second term gives the interaction between the Higgs boson and the fermions, in this case, the b
 460 quarks. The strength of this interaction is directly proportional to the mass of the corresponding fermion.

461 In the SM formalism, neutrinos as massless particles. However, there is no reason why they cannot
 462 acquire mass through the mechanism that we just described. Nonetheless, the usual argument is that it
 463 would be unnatural for the same mechanism to produce the mass of very heavy particles, such as the
 464 top quark, and the mass of very light particle, such as the neutrinos. Therefore, BSM models that try to
 465 explain the mass generation for neutrinos usually resort to a different mechanism.

466 The SM has delivered extremely accurate predictions about the existence and properties of new
 467 particles which make it a very successful theory. It predicted the existence of the W and Z bosons [12],
 468 the gluon, the charm and top quarks and the Higgs boson [6–8]. In addition, the SM prediction for the
 469 value of the anomalous magnetic dipole moment of the electron (calculated up to order α^5) agrees with
 470 the measured value up to the 11th decimal place, making it the most precise measurement in science.

471 2.1.1 Higgs pair production

472 Within the SM there are still some processes that have not been measured. One of these is the pro-
 473 duction of pairs of Higgs bosons. The experimental challenges and efforts related to this process are
 474 discussed in section 4.1. Here we provide a theoretical description of the process.

475 At the Large Hadron Collider (LHC), the main production process of Higgs pairs is gluon-gluon fusion
 476 (ggF). Higgs pairs can also be produced through vector boson (V) fusion (VBF), in association with a
 477 pair of top quarks ($t\bar{t}h$) or through Higgs strahlung (Vh) ⁴. At a center of mass (CM) energy of $\sqrt{s} = 13$
 478 TeV, the ggF production process has a cross section approximately seventeen times larger than the next
 479 most common production process which is VBF (approximately 30 fb *versus* 1.6 fb [13]). Therefore it
 480 is the dominant contribution when we study inclusive production. For this reason we focus the following
 481 discussion on this production mode. The leading order Feynman diagrams for Higgs pair production via
 482 ggF are shown in figure 2.3.

483 The diagram on the left has an off-shell (virtual) Higgs boson, h^* , that couples to gluons by the usual
 484 heavy quark triangle (same mechanism as in single Higgs production). h^* then decays to two on-shell
 485 Higgs bosons. This diagram contains the three point interaction between Higgs bosons and therefore it

⁴In this process, at LO, a Higgs boson is radiated from a vector boson

486 is the one that allows us to probe this coupling. In the diagram on the right, the two Higgs bosons couple
 487 to the gluons by a box of heavy quarks and are directly radiated from a quark. The largest contributions
 488 for these quantum loops come from heavy quarks, such as the top and bottom, because the coupling
 489 constant of the Higgs boson to fermions is directly proportional to the fermions mass (see section 2.1).

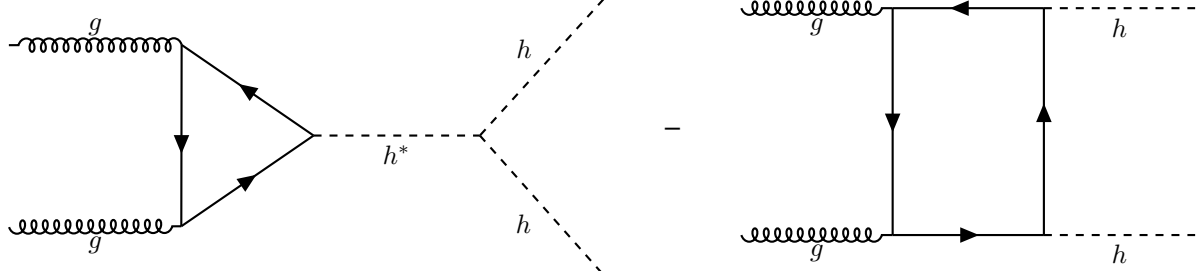


Figure 2.3: Feynman diagrams of Higgs pair production from gluon fusion. Triple vertex diagram (left) and box diagram (right). The minus sign between the diagrams indicates that they interfere destructively.

The amplitudes for the box, \mathcal{M}_\square , and triangle, \mathcal{M}_Δ , diagrams scale as [14]:

$$\mathcal{M}_\square \sim \frac{\alpha_s}{4\pi} y_t^2, \quad \mathcal{M}_\Delta \sim \lambda_{hhh} \frac{\alpha_s}{4\pi} y_t^2 \frac{m_h^2}{\hat{s}} \left(\log \frac{m_t^2}{\hat{s}} + i\pi \right)^2 \quad (2.20)$$

490 where \hat{s} is the CM energy, y_t is the Yukawa coupling of the top quark, α_s is the electroweak coupling
 491 constant, λ_{hhh} is the coupling constant of the Higgs boson three point self-interaction and m_h, m_t are
 492 the masses of the Higgs boson and top quark.

493 At a CM energy of $\sqrt{s} = 13$ TeV the cross section for Higgs pair production, as predicted by NLO
 494 calculations, is very small, approximately 30 fb [13]. It is suppressed due to the destructive interference
 495 between the LO diagrams that leads to a $\sim 50\%$ suppression of the total cross section [14]. Furthermore,
 496 the cross section of the triangle diagram is smaller than the one of the box diagram, approximately 4 fb
 497 compared to 30 fb⁵, and it is strongly suppressed for larger values of the CM energy which can be seen
 498 directly from the expression of the amplitude in Eq. 2.20. This means that the Higgs trilinear coupling
 499 mostly affects the Higgs pair production at threshold, in particular, the m_{hh} distribution. The tail of this
 500 distribution (high invariant mass of the Higgs pair), however, is mostly determined by the box diagram
 501 contribution [14].

The LO calculation for the cross section of Higgs pair production has been performed, for example, in [15]. A value of the order of 10 fb is reported. The NLO calculation is a theoretical challenge: several two-loop diagrams that take into account virtual and real radiation have to be considered. In addition, top quark mass effects can be included in various approximations. This leads to corrections with different signs which suggests that the uncertainty on the cross section due to top quark mass effects are of the order of $\pm 10\%$ at NLO. Therefore, a calculation including the full top mass dependence was of the utmost importance. This result became available recently [16]:

$$\sigma_{gg \rightarrow hh}^{\text{NLO}} = 27.80^{+13.8\%}_{-12.8\%} (\text{scale}) \pm 0.3\% (\text{stat.}) \pm 0.1\% (\text{int.}) \text{ fb} \quad (2.21)$$

⁵These values are obtained using MadGraph5. They are shown here to give a rough estimate of the difference between the values of the cross sections of both diagrams.

502 where the dependence of the result on the variation of the scales by a factor of two around the central
 503 scale, the statistical error coming from the limited number of phase space points evaluated and the error
 504 coming from the numerical integration of the amplitude are shown.

505 This result shows that the introduction of NLO contributions produces a significantly different result.
 506 Therefore the inclusion of such effects is necessary if we wish to obtain an accurate result that can be
 507 compared to experimental values. The analytical expressions for the NLO cross section are long and
 508 complex so we abstain from reproducing them here. Nonetheless, the LO cross section can be written in
 509 a compact form and it allows us to discuss some key features of the process. Therefore, we will present
 510 it here, based on [15] and [17].

The partonic LO cross section for $gg \rightarrow hh$ can be written

$$\hat{\sigma}_{gg \rightarrow hh}^{\text{LO}}(\hat{s}) \sim \int_{\hat{t}_-}^{\hat{t}_+} d\hat{t} \left(|C_\Delta F_\Delta + C_\square F_\square|^2 + |C_\square G_\square|^2 \right) \quad (2.22)$$

where \hat{s} and \hat{t} are the Mandelstam variables and, in addition, \hat{s} can be identified with the square of the partonic CM energy of the process. The integration limits, \hat{t}_\pm , are derived from a momentum parametrization in the CM frame, leading to $\hat{t}_\pm = m_h^2 - \frac{\hat{s}}{2}(1 \mp \beta_h)$, where $\beta_h^2 = 1 - 4\frac{m_h^2}{\hat{s}}$ and m_h is the mass of the Higgs boson [17]. F_Δ , F_\square and G_\square are form factors whose full expressions can be found, for example, in [15]. C_Δ and C_\square can be interpreted as generalized couplings and are given by

$$C_\Delta = \lambda_{hhh} \frac{m_Z^2}{\hat{s} - m_h^2}, \quad C_\square = 1, \quad (2.23)$$

where m_Z is the mass of the Z boson. If we take the limit $m_Q^2 \gg \hat{s} \sim m_h^2$ (where m_Q is the mass of the quarks that contribute to the quantum loops) we can get simple expressions for the remaining form factors:

$$F_\Delta = \frac{2}{3} + \mathcal{O}(\hat{s}/m_Q^2), \quad F_\square = -\frac{2}{3} + \mathcal{O}(\hat{s}/m_Q^2), \quad G_\square = \mathcal{O}(\hat{s}/m_Q^2). \quad (2.24)$$

In this limit, the partonic cross section is simply given by

$$\hat{\sigma}_{gg \rightarrow hh}^{\text{LO}}(\hat{s}) \sim \int_{\hat{t}_-}^{\hat{t}_+} d\hat{t} \left| \lambda_{hhh} \frac{m_Z^2}{\hat{s} - m_h^2} - 1 \right|^2. \quad (2.25)$$

511 There are two important points that are worth discussing. Firstly, the total cross section has terms
 512 that are proportional to the Higgs triple coupling, λ_{hhh} , which can be read directly from Eq. 2.25. On the
 513 one hand, this means that measuring this process gives us access to the value of λ_{hhh} and therefore
 514 provides valuable insight into the shape of the Higgs potential and ultimately into the EWSB mechanism
 515 in the SM. On the other hand, if λ_{hhh} has a value that is different from the one predicted by the SM, that
 516 will affect the measured value of the cross section and can lead to hints of new physics.

517 Secondly, although this is not evident from Eq. 2.25, the cross section for di-Higgs production in-
 518 creases with \hat{s} . This can be seen in figure 2.4 that shows the variation of the total (integrated) NLO cross
 519 section with the CM energy for the six largest production channels. Note that increasing the CM energy
 520 from 13 to 100 TeV increases the inclusive cross section by approximately two orders of magnitude which

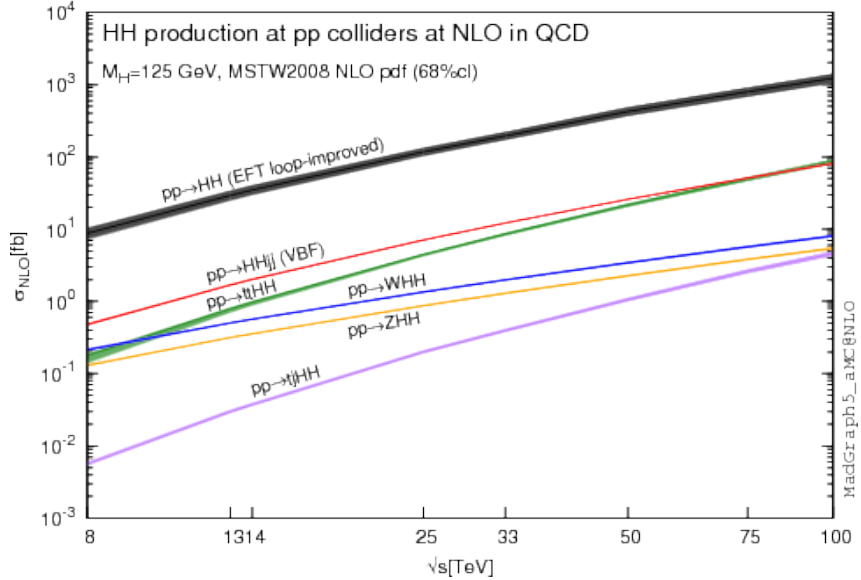


Figure 2.4: Total cross sections at the NLO in QCD for the six largest HH production channels at pp colliders. The thickness of the lines corresponds to the scale and PDF uncertainties added linearly.

521 is a consequence of the increased phase space that becomes available.

522 Therefore, the increase in the cross section of rare processes, such as Higgs pairs production, as
 523 the CM energy of collision experiments increases supports the claim that future colliders, with higher
 524 CM energies, might be our chance of discovering and precisely studying these processes.

525 2.2 Going beyond

526 Despite the success of the SM, there is evidence, both experimental and theoretical in nature, that
 527 indicate that it cannot be the final theory of particle physics. This led to the development of alternative
 528 models that extend the SM but that can still reproduce its successful predictions. These are referred to
 529 as Beyond the Standard Model (BSM) models.

530 On the one hand, there are several pieces of experimental evidence that the SM cannot explain.
 531 These include the nature of dark matter, postulated to explain the experimental observations of the
 532 velocity of far away galaxies [18], the asymmetry between matter and anti-matter in the present Universe
 533 ⁶ and the fact the neutrinos oscillate between flavors which implies that they have a non-zero mass. This
 534 phenomenon was measured independently by two collaborations, the Sudbury Neutrino Observatory
 535 (SNO) and the Super-Kamiokande, in 1998 and 2001-2002, respectively, [19–21].

536 On the other hand, its theoretical formulation also has some weaknesses: it accurately describes
 537 particles interactions at the electroweak scale (~ 246 GeV) but it does not include gravity which means it
 538 cannot be valid at the Planck scale ($\sim 10^{19}$ GeV) where gravity cannot be overlooked; it has a lot (over 20)
 539 of free parameters whose values have to be tuned to fit experimental observations, and there is a large
 540 discrepancy between the mass scales associated with the electroweak and gravitational interactions
 541 (this is one of the simplest formulations of what is known as the hierarchy problem).

⁶Or why do we live in an Universe made entirely out of matter?

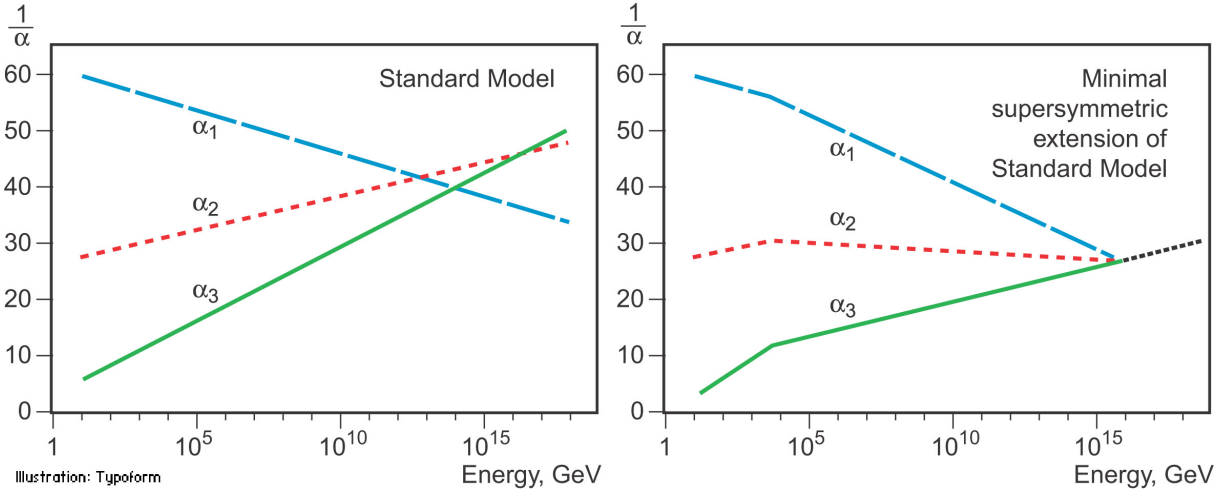


Figure 2.5: Here, α_1 , α_2 and α_3 represent the coupling constants of $U(1)$, $SU(2)$ and $SU(3)$, respectively. What is shown is the variation of the inverse of the coupling with the energy: on the left for the SM and on the right for the MSSM. Plots from [23].

When faced with these weaknesses, or rather hints of incompleteness, the theoretical community put a great effort into the development of models that add new ingredients to the SM but that simultaneous lead to predictions that are compatible with existent experimental measurements. In the following paragraphs we will introduce and briefly describe some of the most well studied (both theoretically and experimentally) BSM models. We follow the discussion presented in [22] as a starting point.

It is a well known consequence of renormalization in QFT that the coupling constants become dependent on the energy scale at which the theory is probed. As the energy scale increases the $U(1)$ coupling constant gets larger while the $SU(2)$ and $SU(3)$ coupling constants get smaller. If one extrapolates far enough these become nearly equal at an energy scale of approximately 10^{15} GeV. Although this matching is far from perfect, it sparked the idea that these three forces could be unified at an energy scale of 10^{15} GeV. Grand Unification Theories (GUT) try to combine $SU(3) \times SU(2) \times U(1)$ into a larger symmetry group.

Supersymmetric (SUSY) models introduce a new symmetry that links fermions and bosons. For each boson(fermion) of the SM it introduces a fermionic(bosonic) partner. Apart from spin, the supersymmetric partners would share the same mass and quantum numbers. Since we have not found any supersymmetric particles in the LHC this means that supersymmetry is necessarily a broken symmetry and, if they exist, new particles should have a larger mass (outside of the present reach of the LHC) than their SM partners. SUSY models were introduced because they offer a natural fix for the hierarchy problem. In addition, the Minimal Supersymmetric extension of the SM (MSSM) also leads to a better convergence of the coupling constants as can be seen in figure 2.5. From the standpoint of GUT this is extremely appealing.

An early proposal of a theory that could unify gravity with electromagnetism was given by Theodore Kaluza in 1921. In particular, he showed that these two forces could stem from a single tensor with the introduction of an extra space dimension. In 1926, Oscar Klein offered an explanation for this extra dimension; he proposed that it had a circular topology such that at each point of the four dimensional

space-time we would have a circle with a small radius. This theory has more degrees of freedom (because it is formulated in a higher dimensional space-time) and therefore it predicts new particles that are usually known as Kaluza-Klein gravitons (and their excited states). Nonetheless, the Kaluza-Klein does not provide a satisfactory explanation for the hierarchy problem. Therefore, in 1999, Lisa Randall and Raman Sundrum introduced a new model that does. This model introduces only two new particles: a spin 2 graviton (and its Kaluza-Klein excitations) and a radion, that is a spin 0 neutral particle.

Models with two Higgs doublets (2HDM) are one of the simplest possible extensions of the Higgs sector of the SM. They are appealing because while the fermionic sector is rather complex, having three families, the scalar sector is quite simple, having a single particle, which seems unnatural. This type of structure is realized in various new physics models including SUSY models. In addition, they provide an additional source for CP violation which could help explain the matter-anti-matter asymmetry in the Universe.

The most general renormalizable 2HDM scalar potential is written as [24]

$$\begin{aligned} V = & m_{11}^2 |\Phi_1|^2 + m_{22}^2 |\Phi_2|^2 - (m_{12}^2 \Phi_1^\dagger \Phi_2 + h.c.) \\ & + \frac{1}{2} \lambda_1 |\Phi_1|^4 + \frac{1}{2} \lambda_2 |\Phi_2|^4 + \lambda_3 |\Phi_1|^2 |\Phi_2|^2 + \lambda_4 |\Phi_1^\dagger \Phi_2|^2 \\ & + \left[\frac{1}{2} \lambda_5 (\Phi_1^\dagger \Phi_2)^2 + \lambda_6 |\Phi_1|^2 (\Phi_1^\dagger \Phi_2)^2 + \lambda_7 |\Phi_2|^2 (\Phi_1^\dagger \Phi_2)^2 + h.c. \right], \end{aligned} \quad (2.26)$$

where Φ_1 and Φ_2 are hypercharge doublets and the coefficients m_{12}^2 and $\lambda_{5,6,7}$ can be complex. However, when including the Yukawa interactions, the most general lagrangian leads to tree-level flavor changing neutral currents (FCNC) in the Yukawa sector. These FCNC are very tightly constrained by experimental data and should be avoided. They can be eliminated by imposing a \mathbb{Z}_2 symmetry. Although, usually, this symmetry is allowed to be softly broken in order to allow the theory to have a decoupling limit [25] where the mass of all the scalars other than the SM-like one can be made very large. In addition to the softly-broken \mathbb{Z}_2 symmetry, which leads to $\lambda_{6,7} = 0$, we also impose CP conservation which makes all possible complex phases vanish. In this case, we obtain five Higgs bosons that are CP eigenstates. Three of them are neutral, h , H and A , and the other two are charged, H^\pm . h and H are CP-even states while A is CP-odd. h is usually taken to be the SM Higgs boson and its mass is set to 125 GeV.

There are several types of 2HDM classified according to their fermion-scalar interactions. We highlight the type II (the one used in this work), where all right-handed up-type quarks couple to Φ_2 and right-handed down-type quarks and charged leptons couple to Φ_1 . This type of couplings is analogous to what happens in SUSY models.

Instead of the parameters in Eq. 2.26, we can describe the model in terms of the four physical masses, m_h , m_H , m_A and m_{H^\pm} , the angles α and β , the VEV $v = 246$ GeV and a further parameter, chosen to be m_{12}^2 [24]. The quartic couplings of the potential can then be written in terms of these parameters, as can be found in Eq. 11 of Ref. [24].

Simplified dark matter (DM) models are based on the exchange of a single particle between DM and SM particles and try to explain the nature of DM and how it interacts with the SM. The particle exchanged is called a mediator and, depending on the specific model, it can be neutral or electrically charged and

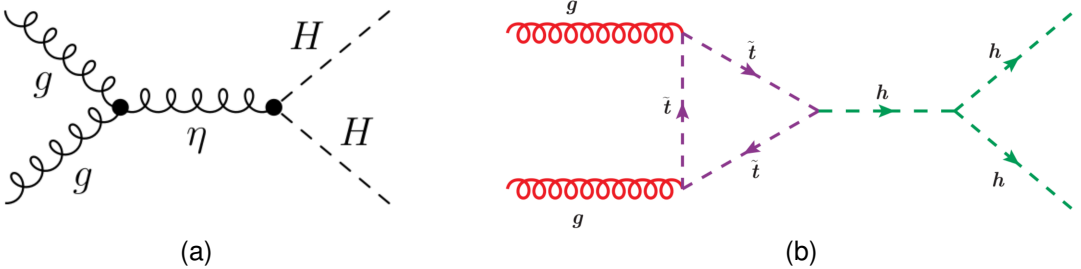


Figure 2.6: BSM contributions to Higgs pair production from the spin-2 Kaluza-Klein graviton (a) and from the SUSY partner of the top quark (b). Figures from Refs. [26, 27].

600 have spin 0, 1 or 2. The simplest possible scenario is a neutral scalar mediator.

601 The CP-conserving 2HDM and dark matter model with a spin 0 mediator are explored in this work
 602 as sources of alternative di-Higgs production processes. For these models, the main modification with
 603 respect to the SM occurs because new heavy particles, namely, H and the DM mediator can couple
 604 to the Higgs bosons through the s-channel diagram. This corresponds to replacing the off-shell Higgs
 605 boson by one of these particles in the Feynman diagram on the left in figure 2.3.

606 The spin-2 graviton predicted by Kaluza-Klein and Randal-Sundrum models can couple directly to
 607 gluons and then decay producing a Higgs pair, as it illustrated in figure 2.6(a). SUSY particles can
 608 contribute to the quantum loops in the Higgs production Feynmann diagrams. An example is shown in
 609 figure 2.6(b), where the top quark is replaced by its supersymmetric partner is the s-channel diagram.
 610 These are two examples of how BSM models can change the Higgs pair production process but there
 611 are many other. The crucial point is that some BSM contributions can lead to an enhancement of the
 612 cross section for Higgs pair production with respect to what is predicted by the SM. Experimentally, this
 613 means that we would not need as much sensitivity and therefore the process could be measured with
 614 less data and therefore sooner. This is the reason why a lot of the searches performed at the LHC focus
 615 on this type of scenario. In addition, if a new heavy particle couples to the Higgs boson via an s-channel
 616 diagram, it could lead to the existence of a peak in the Higgs pair invariant mass spectrum (assuming
 617 that we have enough experimental resolution and that there are not other processes coming into play).

618 Moreover, BSM models introduce new free parameters (in addition to the SM ones) that can be
 619 constrained using the experimental results obtained at the LHC (and other experiments). This reduces
 620 the available parameter space of the models and may even reject some of them.

621 Chapter 3

622 Collider experiments

623 In this chapter we start by providing an overview of the goals and main challenges of modern collider
624 experiments. The definitions of some key quantities that describe an accelerator are introduced and a
625 brief discussion on how they influence the discovery potential of an accelerator is presented.

626 In section 3.2 we introduce the LHC and in section 3.2.1 we describe the ATLAS experiment, includ-
627 ing brief discussions on b-tagging, trigger and data acquisition algorithms and systems. In section 3.3
628 we introduce the concept of a hadronic jet and describe how these objects are reconstructed in a general
629 collider experiment. Jet properties and substructure observables, as well as jet grooming algorithms,
630 are introduced in sections 3.3.1 and 3.3.2, respectively.

631 In section 3.4 we shift the focus to future collider experiments and accelerators and motivate their
632 need. In sections 3.4.1 and 3.4.2 we introduce the hadronic Future Circular Collider (FCC-hh) and
633 describe the baseline detector design, respectively.

634 Collider experiments are the best tool we have to explore matter's most fundamental structure. When
635 we accelerate a particle we increase its momentum. If we take into account the wave-particle duality
636 and the De Broglie expression, $\lambda = h/p$, where λ is the wavelength and p is the particle's momentum,
637 we can see that a particle with a large p will have a small λ . The wavelength gives us the dimension
638 scale of the objects we can probe with a given wave. If we want to probe very small particles (subatomic
639 and smaller) we need very small λ and therefore very large p . Conceptually, this is the basic idea behind
640 modern particle accelerators.

641 In practice, charged particles can be accelerated and their trajectories controlled by means of electro-
642 magnetic fields. However, this is not without numerous technical challenges. When a charged particle is
643 subject to an acceleration perpendicular to its velocity (which is exactly what happens in circular acceler-
644 ators) it emits electromagnetic radiation, called synchrotron radiation. The power emitted is proportional
645 to the fourth power of the particle's energy and inversely proportional to the radius squared and to the
646 fourth power of the particle's mass. This radiation limits the maximum energy that can be achieved in
647 electron-positron colliders. In proton-proton colliders, however, the energy is limited by the maximum
648 magnetic field that can be achieved. Therefore, there is also the need for extremely powerful magnets
649 which are usually implemented using technology based in superconductivity. Using superconducting

650 magnets raises another challenge: they can only operate at very low temperatures, close to the ab-
651 solute zero. In addition, in order to sustain a stable beam it is necessary that the beam pipe has an
652 environment very close to absolute vacuum.

653 3.1 Experimental aspects

One of the most important parameters of a particle accelerator is the time integrated luminosity, $\int \mathcal{L}(t)dt$. For a given process with cross section σ , it determines the number of event that will be produced, N :

$$N = \sigma \int \mathcal{L}(t)dt, \quad (3.1)$$

where $\mathcal{L}(t)$ is the instantaneous luminosity that is a measure of the number of collisions per bunch crossing. The instantaneous luminosity is given by:

$$\mathcal{L} = f_{coll} \frac{n_1 n_2}{4\pi \sigma_x \sigma_y}, \quad (3.2)$$

654 where f_{coll} is the collision frequency, n_1 and n_2 are the number of protons in each bunch and σ_x and σ_y
655 characterize the transverse beam size in the horizontal and vertical directions.

656 To increase the chances of measuring a rare process, or to increase the statistical significance of the
657 measurement of an already discovered process, we want to increase N as much as possible. To do so
658 we can either increase the cross section of the process or the integrated luminosity.

659 While the cross sections of most physics processes increase when the CM energy goes from 13 to
660 100 TeV, many BSM models predict new processes, or new contributions to existing processes, whose
661 cross sections increase more rapidly than the SM backgrounds. In addition, by conservation of energy,
662 a larger CM energy implies that particles with larger mass can be created. Based on Eq. 3.2, we can
663 tune its parameters to obtain the highest possible luminosity. Nonetheless, because we are dealing with
664 charged particles, there is a limit on how close the bunches can be and on how many protons we can
665 pack in a bunch. Moreover, the beam's transverse dimensions cannot be infinitely reduced. A smarter
666 way to increase the number of collisions that an accelerator can produce is to run for a longer time,
667 therefore increasing the integration time in Eq. 3.1.

668 In conclusion, the CM energy and the integrated luminosity are two of the main parameters that drive
669 the discovery potential of an accelerator.

670 3.2 The Large Hadron Collider

671 The LHC is the world's largest and most powerful particle accelerator. It is housed by the European
672 Organization for Nuclear Research (CERN) which focuses on fundamental particle physics with the goal
673 of probing matter's most elementary structure. Ever since its creation, in 1954, CERN has housed many
674 accelerators and experiments and played a key role in the development of fundamental and applied

675 science.

676 The LHC consists of a 27-kilometer ring located beneath the Franco-Swiss border, near Geneva.
677 Most of its running time is dedicated to accelerating protons in opposite directions up to a maximum center
678 of mass energy of $\sqrt{s} = 13$ TeV and colliding them at the center of the two general purpose experiments,
679 ATLAS (which is described in section 3.2.1) and CMS. The LHCb experiment also records data from
680 proton-proton collisions but it is dedicated to the study of beauty particles. The ALICE experiment is
681 optimized to study heavy-ion collisions at a CM energy of 2.76 TeV.

682 The acceleration of charged particles at the LHC is based on radio frequency (RF) cavities. These
683 cavities are shaped to sustain a resonant electromagnetic field that oscillates at a frequency of 400 MHz.
684 During the acceleration stage, charged particles passing through the cavities feel an overall force that
685 propels them forward. When the LHC is running at full energy, a perfectly timed proton with exactly the
686 right energy feels a zero net force when passing the cavities. Protons with a slightly different energies
687 arriving slightly earlier or later are decelerated or accelerated in order to keep the beam sorted in discrete
688 packages with the same energy. These are called bunches. There are 2808 bunches circulating at the
689 same time, each containing approximately 10^{11} protons. The bunches are spaced by 25 ns. Furthermore,
690 the successful operation of the LHC also relies on superconducting magnets made of Niobium-Titanium
691 filaments chilled to -271.3° C and on an ultra high vacuum (of the order of $10^{-10} - 10^{-11}$ mbar) inside
692 the beam pipes. The magnets are placed along the LHC ring and produce dipole and quadrupole
693 electromagnetic fields. The dipole magnets create a nominal field of 8.3 T and bend the beam along the
694 tunnel. The quadrupole magnets focus the beam at the interaction points. The ultra high vacuum greatly
695 reduces the probability that the beam interacts with any particle. It is crucial to keep a stable beam to
696 continuously maintain collisions during long runs.

697 One of the main research goals of the LHC was to discover the Higgs boson. This was achieved
698 in 2012 when ATLAS and CMS reported the discovery of a particle consistent with the boson predicted
699 by the Higgs mechanism, with a mass of 125 GeV [28],[29]. Ever since, efforts have been directed
700 to measuring its mass, couplings, spin-parity properties with increasing precision using different decay
701 channels and production modes.

702 ATLAS and CMS reported the observation (measurement with a significance greater than five sigma)
703 of the Higgs decaying to $b\bar{b}$ [30, 31]. The searches targeted the VH production mode. It offers the best
704 sensitivity to the $hb\bar{b}$ Yukawa coupling because requiring a vector boson helps reduce the SM back-
705 grounds, namely the ones from QCD interactions. The observation of $h \rightarrow b\bar{b}$ means we have now
706 observed all of the Higgs boson's decay modes predicted by the SM. CMS reported the first observation
707 of the Higgs boson decaying to a pair of tau leptons [32]. In addition, the observation of Higgs boson
708 production in association with a $t\bar{t}$ pair was very recently reported by both collaborations [33, 34]. More-
709 over, precision measurements of the masses of the Higgs [35, 36] and W [37] bosons and of the top
710 quark [38, 39] were also performed. So far, no conclusive signs of new physics were seen at the LHC.

711 Future prospects for the LHC include its upgrade to the High Luminosity-LHC (HL-LHC) after the
712 scheduled long shutdown of 2024-2026. This upgrade will increase the size of the dataset to 3000 fb^{-1}
713 over the course of ten years [40]. During the shutdown, the ATLAS detector will be upgraded.

714 In the Higgs sector, the high value of the integrated luminosity will improve the statistical precision of
715 already measured channels and the discovery potential of rare processes [41].

716 3.2.1 The ATLAS detector

717 The ATLAS detector has a cylindrical geometry and a multi layered structure. Its dimensions are 25
718 meters in height (diameter) and 44 meters in length and it weights approximately 7000 tonnes. In the fol-
719 lowing paragraphs we describe the detector's layers and their functionalities. A schematic representation
720 of the detector as well as the appropriate coordinate system can be found in figure 3.1.

721 A combination of cartesian and cylindrical coordinates is used to describe the detector. In both
722 cases, the origin is defined to coincide with the interaction point. The Cartesian system is right-handed
723 and the z axis is defined to be the direction of the beam. The x-axis points from the interaction point
724 to the center of the LHC ring and the y-axis points upwards. The azimuthal angle, ϕ , is measured
725 around the beam axis and the polar angle, θ , from the beam line. The pseudorapidity is defined as
726 $\eta = -\ln \tan(\theta/2)$. Another commonly used quantity is the rapidity, y , defined as a function of a particle's
727 energy, E , and longitudinal momentum, p_L : $y = \frac{1}{2} \ln \left(\frac{E+p_L}{E-p_L} \right)$. In the limit where a particle's mass is
728 negligible with respect to its momentum the pseudorapidity converges to the definition of rapidity. In
729 addition, the angular distance between two points, ΔR , is defined as $\Delta R = \sqrt{(\Delta\phi)^2 + (\Delta\eta)^2}$, where
730 rapidity can also be used instead of the pseudorapidity.

731 The detector consists of an inner detector (ID) or tracker, electromagnetic (EM) and hadronic calorime-
732 ters and a muon spectrometer (MS). The magnet configuration consists of a thin superconducting
733 solenoid that surrounds the ID cavity and three superconducting toroids (one barrel and two end-caps)
734 arranged with an eight-fold azimuthal symmetry around the calorimeters.

735 The ID covers the pseudorapidity range $|\eta| < 2.5$ and it makes up the innermost layer of the detector.
736 It consists of silicon pixel, silicon micro-strip, and straw tube transition radiation tracking detectors. It is
737 contained in a solenoid magnet with a central field of 2 T. The tracker provides precision measurements
738 of the positions and momenta of charged particles. As a charged particle transverses the several layers
739 of the ID it ionizes the medium creating electrical signals that can be read out. These individual electrical
740 signals are then combined to reconstruct the trajectory of the particle.

741 Lead/Liquid-Argon (LAr) sampling electromagnetic (EM) calorimeters cover the pseudorapidity range
742 $|\eta| < 3.2$. The EM calorimeter has an accordion like structure with layers of showering material (lead)
743 interleaved with layers of active material (liquid argon). These calorimeters provide measurements of
744 the energy of electrons and photons. The interaction of these particles with the lead layers induces the
745 production of an EM shower whose energy is measured in the liquid argon layers. The granularity of the
746 EM calorimeter strongly depends on the longitudinal layer and on the pseudorapidity region.

747 The hadronic calorimetry in the pseudorapidity range $|\eta| < 1.7$ is provided by a scintillator-tile
748 calorimeter (TileCal) which is divided in a central barrel and two smaller end-cap barrels, one on each
749 side of the central barrel. The active components are scintillator tiles made of polystyrene that are in-
750 terleaved with steel plates as the passive material. The scintillation light emitted by the tiles when an

Table 3.1: ATLAS tile and liquid argon hadronic calorimeters: summary of the pseudorapidity coverages and transversal segmentation (granularity).

TileCal	Barrel	Extended barrel
Coverage	$ \eta < 1.0$	$0.8 < \eta < 1.7$
Granularity	0.1×0.1	0.1×0.1
LAr calorimeter	End-cap	Forward
Coverage	$1.5 < \eta < 3.2$	$3.2 < \eta < 4.9$
Granularity	0.1×0.1 for $1.5 < \eta < 2.5$ 0.2×0.2 for $2.5 < \eta < 3.2$	0.2×0.2

751 ionising particle crosses the calorimeter is collected on both ends of the tiles by wavelength-shifting
 752 optical fibers. The light signal emitted is proportional to the particle's energy. The TileCal is composed of
 753 several cells with transverse segmentation $\Delta\eta \times \Delta\phi = 0.1 \times 0.1$ ¹ [42].

754 For $|\eta| > 1.5$ LAr calorimeters extend the pseudorapidity range to $|\eta| = 4.9$. The LAr calorimeter is
 755 divided in end-cap and forward. These cover the pseudorapidity ranges $1.5 < |\eta| < 3.2$ and $3.2 < |\eta| <$
 756 4.9, respectively. The active material is liquid-argon and the absorbers are copper and tungsten for the
 757 end-cap and forward calorimeters, respectively. In the end-cap LAr calorimeters the segmentation is
 758 $\Delta\eta \times \Delta\phi = 0.1 \times 0.1$ for $1.5 < |\eta| < 2.5$ and 0.2×0.2 for $2.5 < |\eta| < 3.2$. In the forward LAr calorimeter
 759 the segmentation is $\Delta\eta \times \Delta\phi = 0.2 \times 0.2$.

760 The granularity of the ATLAS hadronic calorimeters is summarized in table 3.1.

761 The hadronic calorimeters provide measurements of the energy of hadrons, jets, τ leptons and miss-
 762 ing transverse energy (E_T^{miss}). Approximately one third of the energy of jets is deposited in this layer.
 763 In the TileCal, the jet energy resolution is given by $\sigma/E \sim 50\%/\sqrt{E} + 3\%$ [42], where the first term is the
 764 stochastic term that derives from sampling fluctuations and follows a Poisson distribution and the second
 765 term is a constant that depends on the characteristics of the calorimeter. For the LAr calorimeter, the jet
 766 energy resolution is given by $\sigma/E \sim 60\%/\sqrt{E} + 2\%$ [43].

767 The MS is the outermost layer of the detector and it is dedicated to detecting muons that travel
 768 through the previous layers almost without interacting. This layer provides measurements of the muons
 769 transverse momenta. It is composed of Monitored Drift Tubes (MDT) and Cathode Strip Chambers
 770 (CSC) that provide high precision measurements of the muons' momentum in the pseudorapidity range
 771 $|\eta| < 2.7$ and of Resistive Plate Chambers (RPC) and Thin Gap Chambers (TGC) dedicated to triggering
 772 purposes for $|\eta| < 2.4$.

773 **b-Tagging**

774 Each collision produces a large number of hadronic jets (we refer to section 3.3 for a detailed description
 775 of jets and how they are reconstructed). For this work, jets initiated by a b quark (b jets) are particularly
 776 important: we are looking for a Higgs pair decaying to four b quarks which leads to an experimental

¹The TileCal is composed of three longitudinal layers. Only the first two have a segmentation equal to 0.1×0.1 . In the third layer the segmentation is 0.2×0.1 . However, most of the energy of hadronic showers is deposited in the first layers and therefore this detail is not very relevant for this work.

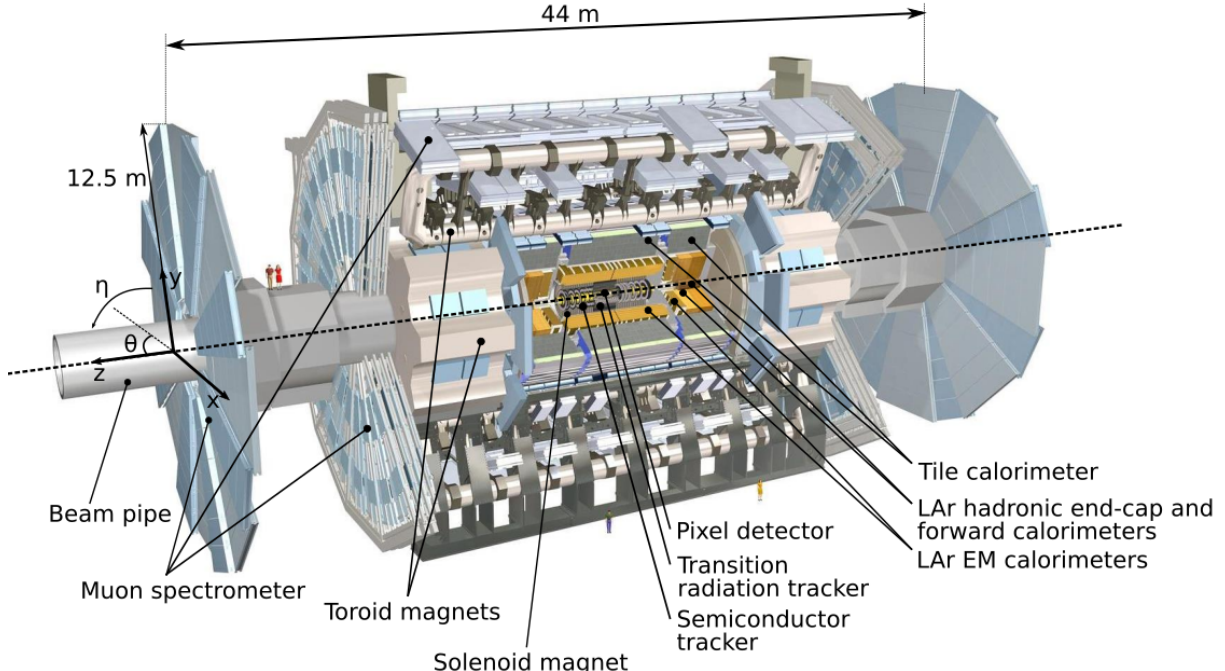


Figure 3.1: ATLAS detector.

777 signature that consists of four b jets. b-Tagging algorithms determine, with a given probability, if a jet
 778 was originated by a b quark.

779 When a b quark is produced it hadronizes almost instantly, producing a B hadron. B hadrons have a
 780 life time of ~ 1 ps and can be highly relativistic meaning that they can travel a few millimeters to a few
 781 centimeters inside the inner detector before decaying. When they decay there is often a reconstructible
 782 secondary vertex that is slightly displaced from the primary vertex where the b-quark was produced.
 783 The existence of a secondary vertex is used by b-tagging algorithms to identify, or tag, a jet as coming
 784 from a b-quark. It is important to note that a complete b-tagging algorithm relies on the reconstruction of
 785 a secondary vertex which can only be done using the information from the inner detector. This implies
 786 that, in ATLAS, we can only b-tag jets that are produced in the region $|\eta| < 2.5$.

787 In ATLAS, b-tagging algorithms are applied to the sub-set of tracks that are associated with a given
 788 jet. The matching between tracks and calorimeter-based jets is performed using the ghost association
 789 technique [44]². The identification of b-jets in ATLAS is based on distinct strategies encoded on three
 790 b-tagging algorithms: impact parameter-based algorithms, an inclusive secondary vertex reconstruction
 791 algorithm and a decay chain multi-vertex reconstruction algorithm. The output of these algorithms are
 792 combined in a multivariate discriminant based on a Boosted Decision Tree (BDT) which provides the
 793 best discrimination between the different jet flavors [45].

794 The impact parameter-based algorithms [46], IP2D and IP3D, use as discriminant variables the trans-
 795 verse impact parameter significance and the transverse and longitudinal impact parameter significance,
 796 respectively. The secondary vertex finding algorithm [46], SV, explicitly reconstructs a displaced sec-

²This procedure works by introducing ghost versions of the measured tracks that have the same direction but infinitesimally small p_T such that they do not modify the properties of the calorimeter jets. The jets are then reclustered and a track is considered to be associated with a given jet if its ghost version is contained in the jet after reclustering.

797 secondary vertex inside the jet by trying to find pairs of tracks with a common origin. The decay chain
798 multi-vertex reconstruction algorithm [47], JetFitter, tries to reconstruct the full b-hadron decay chain.
799 This approach allows to resolve b- and c-hadrons vertices even if there are not two tracks associated
800 with them.

801 **Trigger and data acquisition**

802 The LHC delivers approximately 1000 million proton-proton collisions per second, which corresponds to
803 an event rate of 1 GHz. On the one hand, only a small fraction of these events result in interesting physics
804 processes. On the other hand, the detector does not have enough storage or read out capabilities to
805 record all the collisions. The triggering and data acquisition systems are responsible for selecting a
806 manageable rate of events for permanent storage and further analysis.

807 The trigger is responsible for selecting events with interesting experimental signatures. The trigger
808 system in Run-2 consists of a hardware-based first level trigger (Level-1) and a software-based high
809 level trigger (HLT). The Level-1 trigger takes as input coarse granularity calorimeter and muon detector
810 information and reduces the event rate to 100 kHz. The HLT uses full granularity detector information
811 and reduces the rate to approximately 1 kHz [48].

812 **3.3 Jet reconstruction**

813 A jet is a collimated spray of hadrons that is interpreted as coming from a single initial parton such
814 that approximately retains information about its physical properties, namely 3-momentum, mass and
815 charge. The existence of such objects is a direct consequence of the confinement property of QCD.
816 Quarks and gluons, the fundamental degrees of freedom of QCD, are not asymptotically free. They are
817 confined inside hadrons. Therefore, when one of these particles is produced it undergoes showering
818 and hadronization processes that lead to the formation of hadrons.

819 At a particle detector we are interested in reconstructing jets. These are the objects that are used in
820 the physics analysis. Working with jets instead of hadrons is an advantage because it greatly reduces the
821 number of objects we need to analyze per event. In addition, they work as a *proxy* for the fundamental
822 partons produced in the event.

823 Jets are obtained through jet finding algorithms. These are clustering algorithms that group together
824 experimental quantities (energy deposits in the calorimeters, tracks or particle flow objects) using a
825 sequential recombination scheme. A crucial property of these algorithms is that they should be infrared
826 and collinear safe, meaning that the outcome of the algorithm (namely the number of jets and their
827 properties) should not be significantly modified by the emission of soft radiation or by a collinear splitting.

828 The most widely used jet finding algorithms are the k_T [49], the Cambridge/Aachen (C/A) [50] and
829 the anti- k_T [51]. They are based on distance measurements:

$$d_{ij} = \min(k_{Ti}^{2p}, k_{Tj}^{2p}) \frac{\Delta_{ij}^2}{R^2}, \quad d_{iB} = k_{Ti}^{2p}, \quad (3.3)$$

830 where d_{ij} is the distance between entities i and j and d_{iB} is the distance between entity i and the beam
 831 (B). $\Delta_{ij}^2 = (y_i - y_j)^2 + (\phi_i - \phi_j)^2$ where k_{Ti} , y_i and ϕ_i are the transverse momentum, rapidity and
 832 azimuth of entity i . Here, k_T stands for the transverse momentum. For $p = 1, 0, -1$ we get the k_T , C/A
 833 and anti- k_T algorithms, respectively.

834 The clustering algorithm starts by computing all d_{ij} and d_{iB} distances. If the smallest distance is a
 835 d_{ij} , the four momenta of particle i and j are summed and the distances are updated. If the smallest
 836 distance is a d_{iB} , particle i is removed and called a jet. This procedure is iterated until all particles are
 837 clustered in jets.

838 It is worth discussing further the anti- k_T algorithm since it is the default algorithm used in most
 839 analyses, including this one. In this algorithm, the Δ_{ij} distance between constituents i and j is weighted
 840 by the inverse of the transverse momentum of the constituent with a largest k_T . This feature implies that
 841 particles with larger momenta will have a smaller d_{ij} distance and therefore will be clustered first. This
 842 prevents soft particles from being clustered among themselves before clustering the hardest particles.

843 In ATLAS, the transverse and longitudinal segmentation of the calorimeters allow for a three dimensional
 844 reconstruction of particle showers which is based in a topological clustering algorithm. Topo-
 845 clusters of calorimeters cells are seeded by cells whose absolute energy exceeds the electronic and
 846 pile-up noise by four standard deviations. The topo-clusters are then expanded by adding all adjacent
 847 cells with absolute energy two standard deviations above noise. Finally, all cells neighbouring the pre-
 848 vious set are also added. After energy calibration, the topo-clusters are fed as input to a jet finding
 849 algorithm.

850 Boosted kinematic regime

851 With the increase of the CM energy of particle colliders the production of particles with a transverse
 852 momentum much larger than their mass became a reality. In this kinematic regime (referred to as boosted
 853 due to the high Lorentz boost of the particles) traditional jet reconstruction algorithms, that rely on a one-
 854 to-one correspondence between jets and partons, begin to fail [52].

Due to the high Lorentz boosts, decay products of heavy resonances get more collimated. The angular separation of the decay products is approximately [53]:

$$\Delta R \sim \frac{2m}{p_T} \quad (3.4)$$

855 where p_T and m are the transverse momentum and mass of the decaying particle. In addition to decaying
 856 particles with a larger p_T , another event topology that can produce highly collimated particles is the
 857 decay of a particle with a very large mass (directly seen from Eq. 3.4). This scenario is of particular
 858 interest for new physics searches because BSM models often predict the existence of heavy particles.

859 Take, as an example, the decay of a Higgs boson to two b quarks. Considering that the p_T of the
 860 Higgs is approximately 200 GeV (which is a reasonable and commonly used value in boosted Higgs
 861 bosons searches) we get $\Delta R \sim 1$. For resolved jets, the default jet radius parameter used in ATLAS
 862 is 0.4. We see that for a $p_T \sim 200$ GeV the angular separation between the decay products of a

863 Higgs boson is already similar to the default jet diameter, which can jeopardize the ability to resolve the
864 individual decay products.

865 A possible workaround is to use a single jet with a larger R parameter to reconstruct both decay
866 products. The problem with doing so is that we no longer have information about each individual de-
867 cay product which means we are loosing some information about the event. We cannot, for example,
868 compute angular variables between the decay products. This led to the development of techniques and
869 observables that allow for the exploration of the intrinsic structure (or substructure) of these large- R jets.
870 Some of these techniques are introduced and discussed in the following section.

871 **3.3.1 Jet properties and substructure observables**

872 In general, jet substructure variables aim to quantify the existence of energy clusters insider a jet. Each
873 cluster is interpreted as corresponding to an individual jet. These are called subjets because they are
874 contained inside the large- R jet that was reconstructed. Once they are identified, the subjets can be
875 handled and used for the analysis like normal jets. However, a lot of the substructure techniques do not
876 focus on reconstructing the subjets but rather on determining whether or not they exist, how many they
877 are and how are they distributed inside the large- R jet.

878 Heavy resonances decaying to two(three) particles will produce large- R jets that are consistent with
879 the existence of two(three) energy clusters. Examples of such topologies are the Higgs boson and top
880 quark decays: the Higgs boson always decays to pairs of particles (leptons, quarks or bosons) and the
881 top quark decays, with a probability close to 100%, to a b quark and a W boson that then decays to a
882 pair of leptons or quarks. These topologies are usually referred to as two or three prong. In contrast, jets
883 initiated by a gluon or quark splitting are not expected to have a meaningful substructure. The energy
884 is expected to be concentrated around the jet axis following an isotropic distribution and to become less
885 dense as we approach the jet's border. This is the signature of a one-prong topology. The previous
886 discussion is valid at LO and captures the generic features of jets that are targeted by jet substructure
887 techniques. Nonetheless, other effects may come into play. Take, for example, a highly virtual gluon with
888 a high p_T . If it splits into two quarks the resulting jet may have two subjets and thus mimic the topology
889 of a heavy resonance decay.

The N-subjetiness variable [54], τ_N , may be used to identify jets compatible with N subjets. It is given
by

$$\tau_N = \frac{1}{d_0} \sum_k p_T^k \min(\Delta R_1^k, \dots, \Delta R_N^k), \quad d_0 = \sum_k p_T^k R_0 \quad (3.5)$$

890 where the index k runs over all particles in a jet, the indexes 1 to N identify the number of axis inside the
891 jet and R_0 is the radius of the jet. This variable will have a small value if the particles with the highest p_T
892 (the ones we are most interested in) are clustered around the axis (because ΔR will be small) and will
893 have a larger value otherwise. A jet with small τ_N is considered to be consistent with having N or fewer
894 subjets because all its constituents are aligned with the axis.

895 We usually use ratios of τ_N variables ($\tau_{MN} = \tau_M / \tau_N$). Of particular interest for this work are the τ_{21} ,
896 τ_{31} and τ_{32} ratios. These observables can take values between zero and one. For τ_{21} , for example, a

897 small value (close to zero) indicates that the jet is more compatible with two subjets than with one and
 898 therefore it can help discriminate between two-prong and one-prong jets. The same applies to every
 899 other ratio.

The Fox-Wolfram moments, H_l , can be used to identify jets that have a structure of two back-to-back subjets in their rest frames [55]. They are given by:

$$H_l = \sum_{i,j} \frac{|\vec{p}_i||\vec{p}_j|}{E^2} P_l(\cos(\theta_{i,j})) \quad (3.6)$$

900 where θ_{ij} is the angle between energy clusters i and j , E is the total energy of the clusters in the jet rest
 901 frame and $P_l(x)$ are the Legendre polynomials. For a jet that has a structure of two back-to-back subjets
 902 in its rest frame, $H_1 = 0$, $H_l \sim 1$ for even l , and $H_l \sim 0$ for odd l . This is what we expect for jets coming
 903 from the decay of a boosted resonance. In this work we make use of H_2 .

In addition to jet substructure observables, more standard variables, from which we highlight the jet mass, can also be used to discriminate between jets coming from QCD background and jets resulting from heavy resonance decays. In the latter, the jet's invariant mass should roughly correspond to the mass of the resonance. The invariant mass of a jet, M , is calculated from the energies and momenta of its constituents as follows:

$$M = \left(\sum_i E_i \right)^2 - \left(\sum_i \vec{p}_i \right)^2 \quad (3.7)$$

904 where E_i and \vec{p}_i are the energy and three-momentum of the i^{th} constituent. However, the mass resolution
 905 is not expected to be very good for large-R jets because of all the extra QCD radiation that may be
 906 caught inside the jet. A possible workaround is the use of jet grooming algorithms which we describe in
 907 the following section.

908 3.3.2 Jet grooming algorithms

909 The main goal of jet grooming algorithms is to remove contamination of softer jet constituents from pileup
 910 or underlying event and to leave behind the hard substructure. The main advantage of such algorithms is
 911 that they improve the mass resolution of jets. These features are of particular interest in high luminosity
 912 environments such as the HL-LHC and future high energy colliders.

913 There are three main jet grooming algorithms: trimming, pruning and mass drop filtering. In this
 914 work we do not use pruning or trimming, although these techniques might be worth exploring in future,
 915 more comprehensive, studies. In particular, they can be useful to help reject pileup contributions. The
 916 mass drop filtering procedure isolates relatively symmetric subjets within a jet, each with a significantly
 917 smaller mass than the original jet [53]. This technique was developed and optimized using C/A jets for
 918 the search of Higgs decaying to $b\bar{b}$ pairs [56]. It works as follows:

- The last step of the C/A clustering is undone such that the jet is split in to subjets, j_1 and j_2 with $m_{j_1} > m_{j_2}$. We require that there is a significant difference between the mass of the original jet, m_{jet} , and m_{j_1} : $m_{j_1}/m_{jet} < \mu_{frac}$, where μ_{frac} is a parameter of the algorithm. In addition the splitting

is required to be relatively symmetric:

$$\frac{\min[(p_T^{j_1})^2, (p_T^{j_2})^2]}{(m_{\text{jet}})^2} \times \Delta R_{j_1, j_2}^2 > y_{\text{cut}} \quad (3.8)$$

where y_{cut} is a parameter that defines the energy sharing between the subjets. It is usually taken to be ~ 0.09 . If these two criteria are not met the jet is discarded.

- The subjets are clustered with the C/A algorithm with radius parameter $R_{\text{filt}} = \min[0.3, \Delta R_{j_1, j_2}/2]$. All jet's constituents that are outside of the three hardest subjets are discarded and we obtained the filtered jet and its subjets.

The subjets that are identified within a jet are interpreted as corresponding to the decay products of the particle that produced the original jet. There are usually only two decay products. A third subjet is allowed in order to account for extra QCD radiation.

3.4 Future Colliders

As we already argued in the beginning of this chapter, a larger CM energy is one of the factors driving the discovery potential of an accelerator. As far as we know today, proton-proton colliders are the main, and possibly only, man-made experimental tool available to explore particle physics in the energy range on tens of TeV. With this in mind, new hadronic colliders with CM energies of the order of tens of TeV have been proposed. The main projects are the hadronic Future Circular Collider (FCC-hh) led by CERN and the Super Proton-Proton Collider (SPPC) proposed by China.

In this work we focus on FCC-hh and use the established detector's baseline design as our starting point for this study. In the following section we describe in detail the FCC-hh accelerator and detector.

3.4.1 The hadronic Future Circular Collider

CERN's FCC study group was launched as a result of a recommendation made in the 2013 update of the European Strategy for Particle Physics that '*Europe needs to be in a position to propose an ambitious post-LHC accelerator project at CERN by the time of the next Strategy update*'. It investigates the technological challenges and physics opportunities of a future circular collider. The design and infrastructure are driven by a proton-proton collider (FCC-hh) requirements. Electron-positron (FCC-ee) and electron-proton (FCC-eh) colliders are also being analyzed. The main goal of this effort is to deliver a Conceptual Design Report (CDR) by the end of 2018. This document will include a first cost estimate to be submitted for the next update of the European Strategy for Particle Physics, foreseen by 2018.

The FCC-hh baseline design consists of a proton-proton circular collider with a maximum CM energy of 100 TeV housed by a 100 km tunnel in the area of Geneva. This machine will extend the research program of the LHC (and of the HL-LHC) after these have reached their full discovery potential, by around 2040. In addition, it will allow for the exploration of an entirely new kinematic regime, probing energy scales where new physics may come into play. A possible way of defining the target luminosity of

Table 3.2: Comparison between the working parameters of the LHC and of the FCC-hh. The values of the number bunches and of the number of events per bunch crossing are given assuming a bunch spacing of 25 ns.

Parameter	LHC	FCC-hh
Circumference [km]	27	100
CM energy [TeV]	13	100
Luminosity (peak) [$10^{34}\text{cm}^{-2}\text{s}^{-1}$]	1	30
Dipole field [T]	8.33	16
Nb. of bunches	2808	10600
Nb. of events per bunch crossing	27	1026

950 this machine is to require that within the first year of operation it surpasses the exploration potential of the
 951 LHC [57]. Comprehensive studies [57, 58] indicate that this can be achieved with an integrated luminosity
 952 of the order of 10 ab^{-1} per experiment. Considering a reasonable operation period of 10 years this leads
 953 to integrated luminosity per experiment of the order of 1 ab^{-1} per year. [LUMINOSITY TARGET?]

954 The FCC-hh is expected to work with a dipole field of 16 T and to provide a peak instantaneous lumi-
 955 nosity thirty times larger than the LHC. The number of bunches is expected to be almost a factor of four
 956 larger than for the LHC and the number of events per bunch crossing is expected to be approximately
 957 1000. The latter brings a lot of technical challenges because it means that the mean pileup expected
 958 for the FCC-hh is almost 40 times larger than for the LHC. This requires the development (or improve-
 959 ment of already existing techniques) of techniques and algorithms that allow us to further reject pileup
 960 contributions.

961 Some relevant parameters of the LHC and FCC-hh are summarized in table 3.2.

962 3.4.2 FCC-hh baseline detector

963 The design of the FCC-hh baseline detector, which we describe in detail in this section, has been greatly
 964 based on that of the ATLAS and CMS experiments, in particular the central barrel. The layers and sub
 965 detectors are arranged in the same order and perform very similar roles. The geometry is cylindrical
 966 and therefore we can use exactly the same coordinate system that was introduced in section 3.2.1. The
 967 dimensions are very close to the ones of ATLAS: 25 meters in height (diameter) and 48 m in length [59].
 968 A schematic representation of the FCC detector is shown in figure 3.2.

969 The detector consists of trackers, EM and hadronic calorimeters and MS. The magnet configuration
 970 consists of three solenoid magnets (one central-barrel and two forward) that surround the central bar-
 971 rel calorimeters and the forward trackers. The center solenoid delivers a magnetic field of 4 T at the
 972 interaction point [60].

973 The tracker covers the pseudorapidity range $|\eta| < 6$ and is divided in three sub systems: inner,
 974 outer and forward. The inner and outer trackers and the forward tracker are expected to cover the
 975 pseudorapidity ranges $|\eta| < 2.5$ and $2.5 < |\eta| < 6.0$, respectively. The inner tracker will be instrumented
 976 with pixel detectors while the outer and forward tracker will have layers of both pixel and strip detectors.

977 The EM calorimeter [61, 62] covers the pseudorapidity range $|\eta| < 6$. It is divided in barrel, end-cap

Table 3.3: Hadronic calorimeter layout, granularity and energy resolution.

Parameter	Barrel	End-cap	Forward
η coverage	$ \eta < 1.3$	$1.0 < \eta < 1.8$	$2.3 < \eta < 6.0$
Layout	Sci-Pb-Steel (1 : 1.3 : 3.3)	LAr-Cu (1 : 5)	LAr-Cu (1 : 200)
Granularity ($\Delta\eta \times \Delta\phi$)	0.025×0.025	0.025×0.025	0.05×0.05
Energy resolution (σ_E/E)	$40\%/\sqrt{E} \oplus 2.5\%$	$50\%/\sqrt{E} \oplus 3\%$	$100\%/\sqrt{E} \oplus 5\%$

and forward. These cover the pseudorapidity ranges $|\eta| < 1.5$, $1.4 < |\eta| < 2.5$ and $2.3 < |\eta| < 6$, respectively. The proposed layout for the EM calorimeter is a LAr sampling configuration with lead, glue and steal plates as absorbers. The granularity is expected to be two to four times better than for the ATLAS ECAL. For the barrel calorimeter, the goal energy resolution is $10\%/\sqrt{E} \oplus 1\%$.

The hadronic calorimeter [63] covers the pseudorapidity range $|\eta| < 6$. It is also divided in barrel, end-cap and forward that cover the pseudorapidity ranges $|\eta| < 1.3$, $1.0 < |\eta| < 1.8$ and $2.3 < |\eta| < 6.0$, respectively. The proposed layout for the barrel calorimeter consists of scintillator tiles interleaved with lead and stainless steel plates as absorbers. The end-cap and forward calorimeters are expected to be based on liquid argon with copper plates as absorbers. For the barrel and end-cap calorimeters, the expected segmentation $\Delta\eta \times \Delta\phi = 0.025 \times 0.025$ while for the forward calorimeter it is $\Delta\eta \times \Delta\phi = 0.05 \times 0.05$. Overall, this corresponds to approximately four times the ATLAS HCAL granularity. The energy resolution is expected to be $40\%/\sqrt{E} \oplus 2.5\%$, $50\%/\sqrt{E} \oplus 3\%$ and $100\%/\sqrt{E} \oplus 5\%$, for the barrel, end-cap and forward calorimeters, respectively. The pseudorapidity coverage, layout, granularity and energy resolution of the hadronic calorimeters are summarized in table 3.3.

The muon spectrometer is divided in barrel, end-cap and forward regions that cover the pseudorapidity ranges $|\eta| < 1.0$, $1.0 < |\eta| < 2.5$ and $2.5 < |\eta| < 6.0$, respectively. The muon's system layout is a layered structure of gas chambers.

3.4.3 FCC-hh physics program

The FCC-hh physics program is vast and diverse. Within the SM, it includes the study of gauge bosons pair production and heavy flavor production, the measurement of the top quark's properties and the study of the EWSB mechanism via multi-Higgs production. In addition, heavy ions collisions will allow for a deeper understanding of the Quark-Gluon Plasma. From a BSM standpoint, searches for supersymmetric and dark matter particles in new kinematic regimes can be pursued. A comprehensive review of the physics potential of the FCC-hh can be found here [14]. This document collects the results of the many studies that have been carried out since the beginning of the FCC initiative, in 2014.

Regarding Higgs pair production, a maximum precision on the SM cross section of 3% is expected to be achieved using the $b\bar{b}\gamma\gamma$ final state. This would allow to constraint the Higgs triple coupling to be $\lambda_{hhh} \in [0.97, 1.03]$. The $hh \rightarrow b\bar{b}b\bar{b}$ would allow for a 5% precision on the SM cross section and to constraint the triple coupling to be $\lambda_{hhh} \in [0.9, 1.5]$. In spite of the larger background yield, the $b\bar{b}b\bar{b}$ channel provides a reasonable number of events in the tail of the m_{hh} distribution. As discussed in

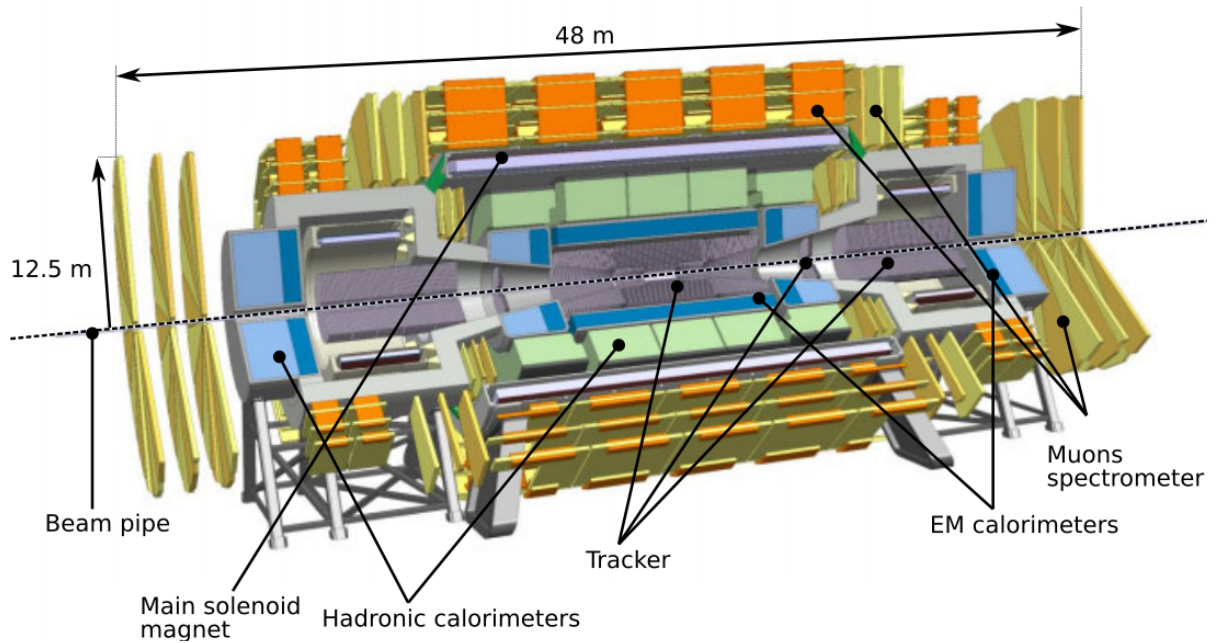


Figure 3.2: FCC detector baseline concept.

1008 section 2.1.1, the tail of this distribution does not have a large contribution from the triangle diagram.
 1009 Therefore, the sensitivity to the Higgs triple coupling is expected to be smaller. However, the high
 1010 energy regime can be more sensitive to new physics contributions which makes the $b\bar{b}b\bar{b}$ channel a very
 1011 interesting one.

1012 The Higgs quartic coupling could be probed through triple Higgs production. In this case the most
 1013 promising final state seems to be $b\bar{b}b\bar{b}\gamma\gamma$. This channel could constrain the Higgs quartic coupling to be
 1014 $\lambda_{hhh} \in [-4, 16]$.

1015 **Chapter 4**

1016 **State of the art**

1017 In this chapter we present the state of the art of searches for Higgs pairs production at the LHC and
1018 feasibility studies targeting searches for this process at future colliders. In addition, previous studies
1019 focusing on the granularity of the hadronic calorimeter as a key detector parameter are also reviewed.

1020 In section 4.1, we review the searches that have been conducted at the LHC by the ATLAS and CMS
1021 experiments. We include discussions on the different final states that were targeted and report on the
1022 constraints that were derived for the di-Higgs cross section and trilinear coupling. A brief overview of
1023 the current constraints on some BSM models is also presented. In section 4.2, we present the results
1024 obtained from feasibility studies that access the discovery potential for this process at the HL-LHC and
1025 at the FCC-hh. In section 4.3, we present previous studies on the impact of the granularity of the
1026 hadronic calorimeter on the spatial resolution of hadrons and on the resolution of the jet mass and of jet
1027 substructure observables.

1028 **4.1 Searches for Higgs pair production at the LHC**

1029 The discovery of the Higgs boson is a strong evidence that the Higgs mechanism operates in Nature.
1030 However, by itself, it does not guarantee that the shape of the Higgs potential is the one depicted in
1031 figure 2.2, on the right. In order to reconstruct the Higgs potential and gain a deeper understanding of
1032 the mechanism that leads to the breaking of the electroweak symmetry one must measure the Higgs
1033 boson self-couplings, namely its three and four point interactions, whose strengths depend on the values
1034 of the parameters of the Higgs potential, as shown in section 2.13.

1035 However, in the SM, the cross section for the production of Higgs pairs through ggF is extremely
1036 small: $\sim 30 \text{ fb}$ at the current CM energy achieved at the LHC (value computed at Next to Leading
1037 Order (NLO) accuracy) [64]. This value is approximately three orders of magnitude smaller than the
1038 production cross section of a single Higgs boson. In addition, this value has to be multiplied by the
1039 branching fraction of the chosen decay channel which further reduces the effective cross section of the
1040 full process. Nonetheless, ATLAS and CMS have conducted searches for this process whose results
1041 are summarized in this section.

1042 The searches performed so far covered different decay channels and targeted not only the SM pro-
1043 cess but also some BSM scenarios where di-Higgs production is enhanced. Neither could achieve
1044 enough statistical significance to declare the measurement of this process in the SM nor have found any
1045 significant deviation from the expected values. These searches resulted in upper limits for the cross sec-
1046 tion of di-higgs production in the SM and for the values of the parameters of BSM benchmark theories.
1047 From the limits on the cross section it is also possible to constraint the values of the Higgs self coupling,
1048 $k_\lambda = \lambda_{hhh}/\lambda_{hhh}^{SM}$.

1049 The $hh \rightarrow b\bar{b}b\bar{b}$ channel [65, 66] benefits from the large branching fraction of $h \rightarrow b\bar{b}$ ($\sim 58\%$). In
1050 addition, ATLAS showed that this is the most sensitive channel to resonance masses over 500 GeV [67].
1051 However, this channel suffers with an overwhelming multijet background which drives the need for very
1052 tight trigger level cuts in order to bring the event rates down to manageable values.

1053 The $hh \rightarrow b\bar{b}\tau\tau$ analysis [68, 69] benefits from a sizable branching fraction of $h \rightarrow \tau^+\tau^-$ ($\sim 7.3\%$)
1054 and from a relatively small background contribution from other SM processes. These searches target
1055 the semi-leptonic decay of the $\tau\tau$ pair to reduce contamination from QCD processes.

1056 The $hh \rightarrow b\bar{b}\gamma\gamma$ [70, 71], $WW^*\gamma\gamma$ [67, 72], $ZZ\gamma\gamma$ [72] analysis can make use of very efficient diphoton
1057 triggers and isolation criteria that greatly reduce multijet background. In addition the excellent mass
1058 resolution of $h \rightarrow \gamma\gamma$ can be exploited. The $hh \rightarrow b\bar{b}WW^*$ channel also benefits from the large branching
1059 fraction of $h \rightarrow W^+W^-$ ($\sim 21\%$).

1060 The most stringent upper limit on the cross section of Higgs pair production comes from a combina-
1061 tion of three searches using up to 36.1 fb^{-1} of proton-proton collision data at a CM energy of $\sqrt{s} = 13$
1062 TeV collected with the ATLAS detector [73]. The combination is based on the three most sensitive decay
1063 channels of Higgs boson pairs, i.e., $hh \rightarrow b\bar{b}\gamma\gamma$, $hh \rightarrow b\bar{b}\tau^+\tau^-$ and $hh \rightarrow b\bar{b}b\bar{b}$. The combined observed
1064 limit on the non-resonant Higgs boson pair cross-section is 0.223 pb at 95% CL, which corresponds to
1065 6.7 times the cross-section predicted by the SM. The ratio of the Higgs boson self-coupling to its SM
1066 expectation, k_λ , is constrained, at 95% CL, to be $-5.0 < k_\lambda < 12.1$.

1067 The upper limits on the cross section (at 95% CL) of Higgs pair production at 8 TeV as a function of
1068 the mass of a spin 0 resonance are summarized in figure 4.1(a) [70]. The limits were obtained using
1069 data collected with the CMS detector and come from searches using different final states, namely, $b\bar{b}\gamma\gamma$ (blue),
1070 $b\bar{b}b\bar{b}$ (red and pink) and $b\bar{b}\tau\tau$ (green). Depending on the analysis, the corresponding integrated
1071 luminosity varies between 17.9 fb^{-1} and 19.7 fb^{-1} . The results are usually interpreted in the framework
1072 of the Randall-Sundrum models such that the spin 0 resonance corresponds to the radion that decays
1073 to a pair of Higgs bosons. For a mass of 1 TeV the upper limit on the cross section is approximately 12
1074 pb.

1075 The upper limits on the cross section (at 95% CL) of Higgs pair production as a function of the mass
1076 of a heavy scalar Higgs, m_H , are summarized in figure 4.1(b) [74]. The limits were obtained through a
1077 combination of searches performed in the $hh \rightarrow b\bar{b}\gamma\gamma$, $hh \rightarrow b\bar{b}b\bar{b}$, $hh \rightarrow b\bar{b}\tau^+\tau^-$ and $hh \rightarrow \gamma\gamma W^+W^-$
1078 channels using proton-proton collision data corresponding to an integrated luminosity of 20.3 fb^{-1} col-
1079 lected with the ATLAS detector at a CM energy of $\sqrt{s} = 8 \text{ TeV}$. The improvement above $m_H = 500 \text{ GeV}$
1080 is due to the sensitivity of the $hh \rightarrow b\bar{b}b\bar{b}$ analysis. For $m_H = 900 \text{ GeV}$ the observed limit is 0.015 pb .

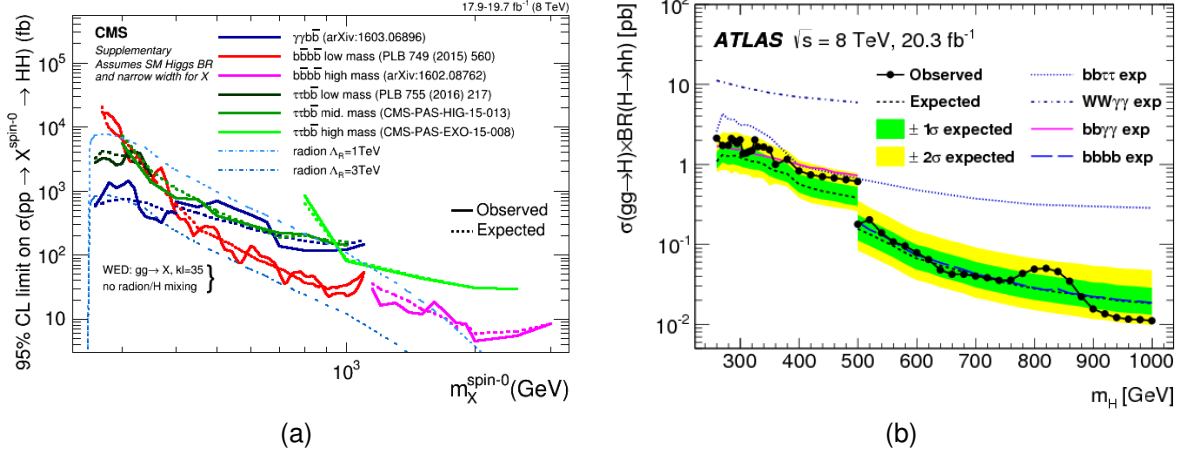


Figure 4.1: Exclusion limits (at 95% CL) on the cross section of resonant Higgs pair production from the decay of heavy scalar particles. These results were obtained using proton-proton collision data collected with the CMS (a) and ATLAS (b) detector at a CM energy of $\sqrt{s} = 8$ TeV and result from the combination of different channels. Plots from [70] and [74].

4.2 Feasibility studies for high-luminosity and future colliders

Without any BSM contribution, the discovery of Higgs pairs production in the four b quarks final state at the LHC is highly unlikely even considering the total expected integrated luminosity of 300 fb^{-1} . There might be evidence for this process but retrieving useful information about the value of the Higgs trilinear coupling will remain out of reach. Nonetheless, the HL-LHC as well as future colliders pose a good opportunity for the discovery and precision studies of this process. Therefore, Monte Carlo studies assessing the feasibility of searches for $hh \rightarrow b\bar{b}b\bar{b}$ at the HL-LHC and at the FCC-hh have been performed.

For the HL-LHC, a study including the $pp \rightarrow b\bar{b}b\bar{b}$, $pp \rightarrow b\bar{b}jj$, $pp \rightarrow jjjj$ and $pp \rightarrow t\bar{t} \rightarrow b\bar{b}jjjj$ backgrounds reports a significance (S/\sqrt{B}) of 4 (1.3) for an integrated luminosity of 3000 (300) fb^{-1} [75]. The analysis is performed in three orthogonal regions (boosted, intermediate and resolved) and the reported significance is obtained from the combination of these three regions. The highest significance ($S/\sqrt{B} = 2.9$) is achieved in the boosted category. In addition, the impact of pile up is evaluated. Considering a mean pile up of 80 and making use of jet grooming techniques, a significance of 3.1 (1.0) for an integrated luminosity of 3000 (300) fb^{-1} is reported (also considering the three analysis regions). This work makes use of artificial neural networks (ANN's) as well as of jet substructure observables to further increase the signal-background separation. Furthermore, single Higgs backgrounds, namely $Z(\rightarrow b\bar{b})h(\rightarrow b\bar{b})$, $t\bar{t}h(\rightarrow b\bar{b})$ and $b\bar{b}h(\rightarrow b\bar{b})$, are shown to be negligible for the analysis, when compared to the dominant QCD multijet background.

ATLAS and CMS also carried out preliminary studies for the sensitivity on the trilinear coupling at the HL-LHC. Several channels have been investigated: $hh \rightarrow b\bar{b}\gamma\gamma$, $hh \rightarrow b\bar{b}\tau^+\tau^-$, $hh \rightarrow b\bar{b}W^+W^-$ and $hh \rightarrow b\bar{b}b\bar{b}$. The $b\bar{b}\gamma\gamma$ final state is the most sensitive one. In this channel, ATLAS and CMS reported significances of 1.05σ and 1.6σ , respectively, for an integrated luminosity of 3000 fb^{-1} . Taking, as an example, the ATLAS result, the achieved significance translates to an upper limit on the total

1105 di-Higgs cross section of approximately twice the SM value. This corresponds to an exclusion limit of
1106 $-0.8 < k_\lambda < 7.7$. The analysis conducted by ATLAS in this channel is done at generator level. The
1107 energy and momenta of the particles are smeared to simulate the detector's response. A mean pile up
1108 of 200 is considered. No MVA techniques are employed in the analysis.

1109 For the $hh \rightarrow b\bar{b}b\bar{b}$ channel, ATLAS states that a cross section 5.2 times larger than the SM value can
1110 be excluded at 95% CL, with systematic uncertainties being taken into consideration. The Higgs trilinear
1111 coupling is expected to be constrained to $-3.5 < k_\lambda < 11$. These results are based on the extrapolation
1112 of the current results obtained with the 2016 dataset, comprising an integrated luminosity of 10.1 fb^{-1} .
1113 This study is based only on the resolved analysis documented in [65].

1114 For the FCC-hh, a recent study that uses as signal sample $pp \rightarrow hhj \rightarrow b\bar{b}b\bar{b}j$ and that includes
1115 only the irreducible $pp \rightarrow b\bar{b}b\bar{b}j$ reports a significance of 6.61 for an integrated luminosity of 30 ab^{-1} ,
1116 considering an analysis that targets the boosted region [76]. The extra jet in the signal sample has
1117 $p_T > 200 \text{ GeV}$ which provides the Higgs pair with a large Lorentz boost. This enhances the sensitivity
1118 to the Higgs boson self coupling because it favors highly boosted virtual Higgs bosons decaying to a
1119 pair of Higgs bosons. The analysis relies on the jet substructure observable τ_{21} and on a tight mass cut
1120 around the Higgs mass. No multivariate techniques are employed.

1121 A study comparing the feasibility of the search for di-Higgs production in the $b\bar{b}b\bar{b}$ in the HL-LHC and at
1122 the FCC-hh was presented in [77]. Only the irreducible background is considered. For a boosted region,
1123 cut based analysis, a significance of 1.1 is reported for an integrated luminosity of 3 ab^{-1} at $\sqrt{s} = 14 \text{ TeV}$
1124 (HL-LHC). For an integrated luminosity of 10 ab^{-1} at $\sqrt{s} = 100 \text{ TeV}$, which corresponds to the FCC-hh,
1125 this number is 5.7. While the significance is large for the FCC-hh, the reported signal to background ratio
1126 (S/B) is approximately one order of magnitude smaller, which means the measurement might be more
1127 sensitive to systematic uncertainties on the backgrounds.

1128 4.3 Hadronic calorimeter granularity studies

1129 Even before the baseline design for the FCC-hh was established, there were studies regarding the
1130 impact of the granularity of the calorimeters in the spatial resolving power of hadronic showers and on
1131 the resolution of jet mass and substructure variables. These studies targeted the development of future
1132 colliders and greatly influenced the baseline design of the FCC-hh.

1133 The granularity of hadronic calorimeters is a key parameter for future collider detectors because it
1134 determines how well we can resolve energy deposits from pileup vertices and highly-boosted jet topolo-
1135 gies. In Ref. [78], the use of smaller calorimeter cells (smaller than the ones that are used in currently
1136 operating hadronic calorimeters) to resolve individual hadrons is investigated. For two Kaons (K_L^0) with
1137 an energy of 100 GeV each and with a truth level separation (ΔR) equal to 0.035 the energy deposited in
1138 the ECAL (blue) and HCAL (red) is shown as a function of ΔR for HCAL cells with sizes $20 \text{ cm} \times 20 \text{ cm}$
1139 ($\Delta\eta \times \Delta\phi = 0.1 \times 0.1$) and $5 \text{ cm} \times 5 \text{ cm}$ ($\Delta\eta \times \Delta\phi = 0.022 \times 0.022$) is shown in figures 4.2(a) and
1140 4.2(b), respectively. The ECAL segmentation is equal to $2 \text{ cm} \times 2 \text{ cm}$. It is shown that for a granularity
1141 of $\Delta\eta \times \Delta\phi = 0.022 \times 0.022$ both hadrons can be resolved in the HCAL.

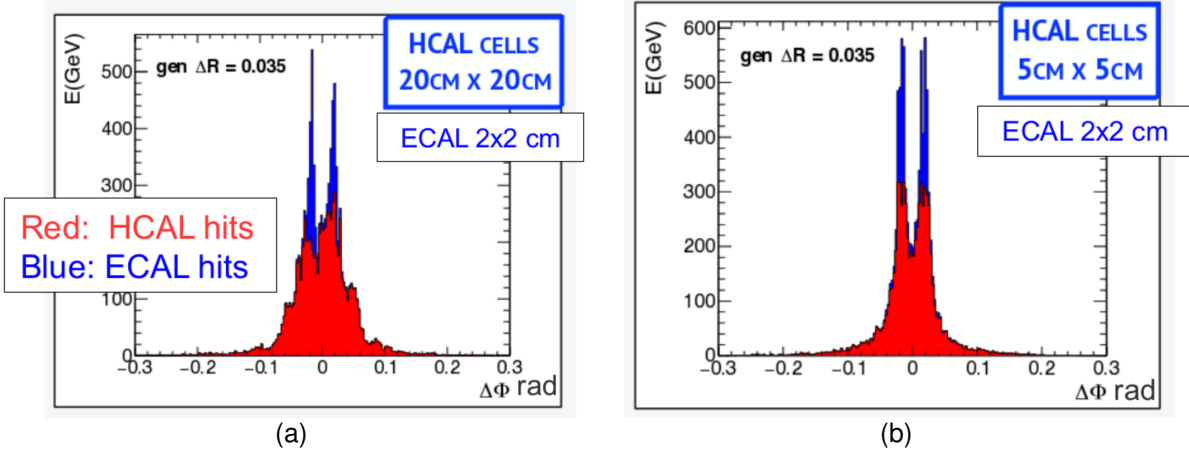


Figure 4.2: Azimuthal distribution of the energy deposits in the ECAL and HCAL for a pair of K_L^0 with $E = 100$ GeV for an hadronic calorimeter with $20\text{ cm} \times 20\text{ cm}$ (a) and $5\text{ cm} \times 5\text{ cm}$ (b). Figures from [79] (based on [78]).

Additional studies focusing on the jet mass resolution and on the resolution of jet substructure observables were performed for three calorimeter configurations (HCAL and ECAL). Some of these studies were presented in major conferences focused on future colliders, namely FCC week 2015 and 2016 and BOOST 2017. Here, we show results presented in Refs. [79–81]. The calorimeter configurations tested are: HCAL(ECAL) $0.1(0.025)$ $\eta \times 5.6(1.4)$ ϕ , HCAL(ECAL) $0.05(0.012)$ $\eta \times 2.8(0.7)$ ϕ and HCAL(ECAL) $0.025(0.006)$ $\eta \times 1.4(0.35)$ ϕ . For the segmentation in ϕ the numbers are give in degrees. For the HCAL, these correspond to approximately $\Delta\eta \times \Delta\phi = 0.1 \times 0.1, 0.05 \times 0.05, 0.025 \times 0.025$.

For $t\bar{t}$ events generated at NLO with MadGraph5 and passed through Delphes 3.2 to simulate detector response, the energy-flow jet mass distribution for $p_T(\text{jet}) > 3$ TeV is shown in figure 4.3(a) [80]. The jet mass resolution¹ is shown in figure 4.3(b). For $\Delta\eta \times \Delta\phi = 0.1 \times 0.1$ cells the root mean square (RMS) of the distribution is 0.130. This value decreases to 0.090 and 0.088 for $\Delta\eta \times \Delta\phi = 0.05 \times 0.05$ and $\Delta\eta \times \Delta\phi = 0.025 \times 0.025$ cells, respectively. This indicates that the mass resolution increases as the granularity of the HCAL increases.

Regarding jet substructure, the resolution of the τ_{32} variable in QCD dijet events generated with Pythia8 is shown in figure 4.4(a) for particle flow (or energy flow) jets [80]. The same distribution is shown in figure 4.4(b) for calorimeter (tower) jets. Regardless of the type of jets used (eflow or tower jets), the τ_{32} resolution increases as the HCAL resolution increases. In addition, it is important to note that the resolution is a lot worse when using tower jets which is an indication that exploiting tracking information is vital to achieve a good resolution in substructure variables.

Another interesting result, presented in Ref. [79], has to do with the overlap between the τ_{21} distribution for QCD and W jets. Jets with of 2.5 TeV show a reduction in overlap ($80\% \rightarrow 60\%$) going from $\Delta\eta \times \Delta\phi = 0.1 \times 0.1$ to $\Delta\eta \times \Delta\phi = 0.005 \times 0.005$ HCAL cells. For 5(10) TeV jets the overlap goes from 88(91)% to 78(85)%. However, for 20 TeV jets, the change in the HCAL granularity does not modify the overlap, as is shown in figure 4.5.

¹The resolution of a given observable, X , is given by $(X^{\text{reco}} - X^{\text{true}})/X^{\text{true}}$.

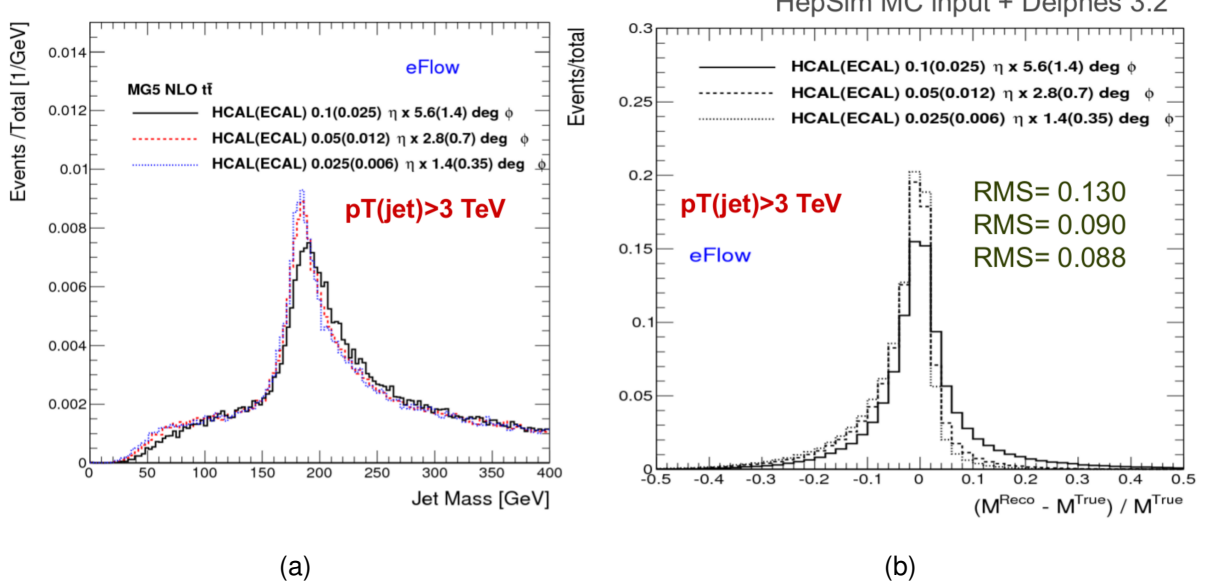


Figure 4.3: Jet mass (a) and jet mass resolution (b) plots in $t\bar{t}$ events for eflow jets with $p_T > 3$ TeV for three different HCAL and ECAL configurations: HCAL(ECAL) 0.1(0.025) $\eta \times 5.6(1.4)$ deg ϕ , HCAL(ECAL) 0.05(0.012) $\eta \times 2.8(0.7)$ deg ϕ and HCAL(ECAL) 0.025(0.006) $\eta \times 1.4(0.35)$ deg ϕ . Plots from Ref. [79].

In summary, previous studies focus on the impact of granularity in the resolution of jet mass and jet substructure observables. We did not find any studies that explored the change in the significance of a given analysis as a function of the granularity or of the detector configuration.

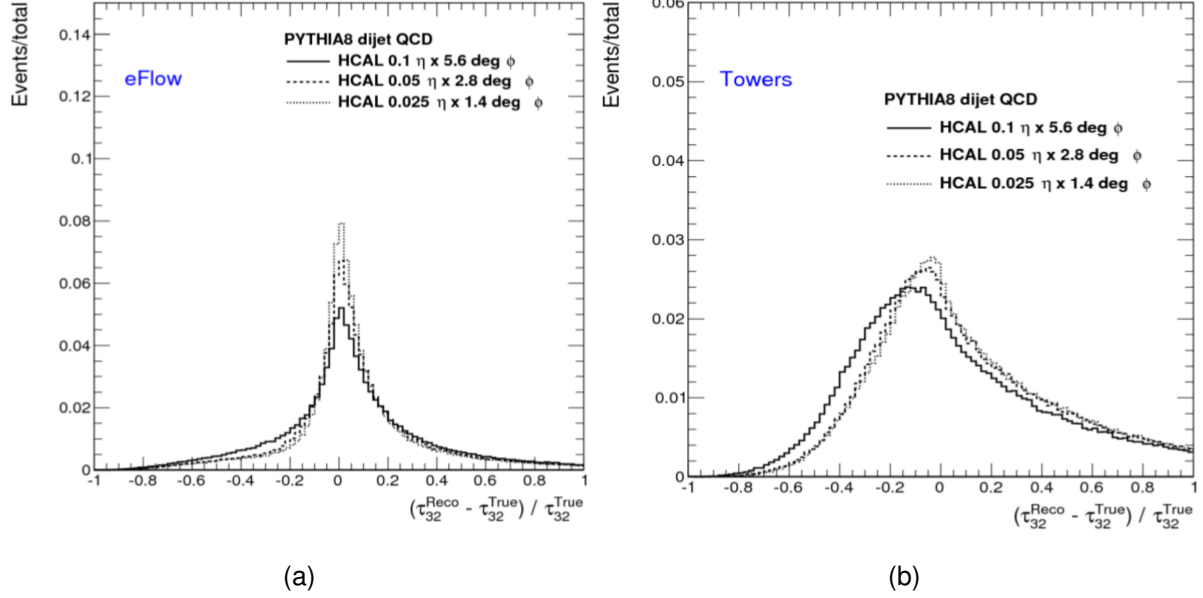


Figure 4.4: τ_{32} resolution plots for QCD dijet events reconstructed using eflow jets (a) and tower jets (b). Plots from Ref. [80].

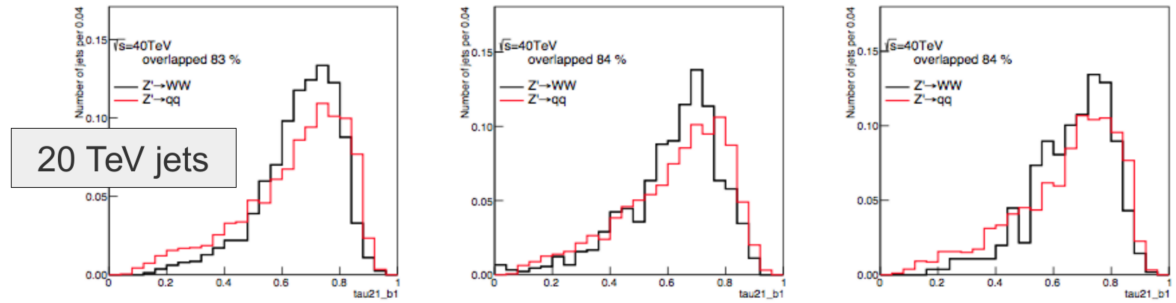


Figure 4.5: τ_{21} variable for 20 TeV W (black) and QCD jets (red) for three HCAL granularities: $\Delta\eta \times \Delta\phi = 0.1 \times 0.1$ (left), $\Delta\eta \times \Delta\phi = 0.022 \times 0.022$ (middle) and $\Delta\eta \times \Delta\phi = 0.005 \times 0.005$ (right). Plots from Ref. [79].

1169 **Chapter 5**

1170 **Sample generation and analysis tools**

1171 A crucial component of this work is the generation of the Monte Carlo samples that are used in the anal-
1172 ysis. They are produced using fast simulation. We use the software and machinery that was developed
1173 by the FCC study group at CERN. The simulation work flow and Monte Carlo samples are described in
1174 this chapter.

1175 In section 5.1 we introduce the generators used to produce the Monte Carlo samples and briefly
1176 describe their working principles and functionalities. We then focus on the FCC-hh software, in subsec-
1177 tion 5.1.2, and explain how the previously described simulation work flow is implemented. A detailed
1178 description of the technical settings used to produce the samples is provided in sections 5.2 and 5.2.3.

1179 **5.1 Fast simulation workflow**

1180 The Monte Carlo samples used in this study were generated using MadGraph5_aMC@NLO [82]. The
1181 showering and hadronization are simulated using Pythia 8 [83] and the detector response is parametrized
1182 using Delphes 3 [84]. These samples are available at the CERN EOS storage.

1183 MadGraph5 is a matrix element generator for high energy physics processes, such as decays and
1184 scatterings. The user specifies the desired process in terms of the initial and final states and can impose
1185 additional constraints such as allowing for a number of refined criteria, including forced or forbidden s-
1186 channel resonances, excluded internal particles, and forced decay chains of final state particles [82].
1187 As a result, MadGraph automatically generates the corresponding Feynman diagrams and creates the
1188 necessary code to compute the matrix element at a given point of the phase space. The output file is
1189 written in the Les Houches Accord [85].

1190 Pythia8 is frequently used for event generation in high energy physics. In this work, however, we use
1191 it only to simulate the showering and hadronization process and not the parton level hard process which
1192 is simulated in MadGraph5. The Les Houches file that is produced by MadGraph5 is used as input to a
1193 Pythia8 program that can decay unstable particles, simulate initial and final state showers as well as the
1194 hadronization of coloured particles, such as quarks and gluons. The desired settings can be specified
1195 in an additional file, a card, that is used as input for a Pythia8 run.

1196 Delphes3 allows for a quick and simple simulation of the detector's response [84]. Its goal is to allow
1197 the fast simulation of a multipurpose detector for phenomenological studies. The simulation includes a
1198 track propagation system, electromagnetic and hadronic calorimeters and a muon identification system.
1199 Low level physics objects, such as tracks and energy deposits, and high level physics objects, such as
1200 leptons and jets, are reconstructed from the detector's response and can be used to perform physics
1201 analysis. In the following paragraphs we briefly describe how the detector response is simulated and
1202 how jet reconstruction is performed.

1203 The magnetic field is uniform, axial and parallel to the beam direction. Charged particles follow a
1204 helicoidal trajectory from the interaction point to the calorimeter while neutral particles have a straight
1205 line trajectory. The probability of a charged particle being reconstructed as a track is defined by the
1206 user. Only a smearing in the modulus of the transverse momentum is applied (not to the direction). The
1207 tracking efficiency as well as energy and momentum resolutions are specified by the user and may in-
1208 clude a dependency on the particle type, momentum and pseudorapidity. The calorimeters have a finite
1209 segmentation in the (η, ϕ) plane and the cell size can be defined in the configuration file. The amount
1210 of energy deposited in the calorimeters by each particle type can be defined by the user. By default,
1211 stable hadrons deposit all their energy in the HCAL although in a real detector a significant fraction of
1212 their energy is deposited in the ECAL. The energy resolution of the ECAL and HCAL are parameter-
1213 ized as a function of η and include stochastic, noise and constant terms: $\sigma(E)/E = a/\sqrt{E} \oplus b$. The
1214 electromagnetic and hadronic energy deposits are independently smeared by log-normal distributions.

1215 Jets can be produced using generator level long-lived particles after showering and hadronization,
1216 tracks, calorimeter towers or particle-flow tracks and towers. These are referred to as generator, track,
1217 calorimeter or particle-flow jets, respectively. For generator level jets no detector simulation nor recon-
1218 struction are taken into account. In spite of the type of jet the user can choose the jet clustering algorithm
1219 and the values of its parameters as well as the minimum transverse momentum of the jets that are stored
1220 in the final collection. Delphes integrates the FastJet package [86] and therefore allows jet reconstruc-
1221 tion with the most popular jet reconstruction algorithms, namely, anti- k_T , k_T and Cambridge-Aachen
1222 (C/A). Jets resulting from the hadronization of a b quark (known as b jets), are identified if a b quark is
1223 found within a ΔR distance from the jet's axis. The tagging efficiency and mis-tagging probabilities can
1224 be defined by the user.

1225 5.1.1 Particle flow and calorimeter reconstruction in Delphes

1226 In Delphes, hadronic jets can be reconstructed using only the information from the HCAL towers or using
1227 a particle flow algorithm that combines information from the tracking system and from the HCAL towers.
1228 These two approaches create jets that are referred to as calorimeter and particle flow jets, respectively.
1229 The latter can also be referred to as energy flow jets (eflow jets in short). In this work we performed the
1230 analysis using both sets of jets and compare the results. Therefore we briefly describe them here.

1231 Calorimeter jets are very simple. They are reconstructed using as input for the jet clustering algorithm
1232 the 4-vectors associated with the calorimeter towers, after a cell energy smearing has been applied.

1233 Therefore the energy resolution is limited by the transverse segmentation of the calorimeters.

1234 The goal of the particle flow approach is to make use of all the available information provided by the
1235 various sub-detectors for reconstructing an event [84]. This approach is used by some experimental
1236 collaborations [87, 88] but the exact implementation depends on the specificities of the experiment. If
1237 the momentum resolution of the tracking system is better than the energy resolution of the calorimeters
1238 it might be convenient to use the tracking information to estimate the momentum of charged particles.
1239 In real experiments, the tracking resolution is only better than the calorimeter's energy resolution up to
1240 some energy threshold. However, in Delphes, it is assumed that it is always convenient to estimate the
1241 momentum of charged particles via the tracker.

1242 The particle flow algorithm works as follows [84]. For each calorimeter tower it counts:

- 1243
- the total energy deposited in ECAL and HCAL, E_{ECAL} and E_{HCAL} , respectively;
 - the total energy deposited in ECAL and HCAL originating from charged particles for which a track
1244 has been reconstructed, $E_{\text{ECAL,trk}}$ and $E_{\text{HCAL,trk}}$, respectively.
- 1245

Then it defines $\Delta_{\text{ECAL}} = E_{\text{ECAL}} - E_{\text{ECAL,trk}}$, $\Delta_{\text{HCAL}} = E_{\text{HCAL}} - E_{\text{HCAL,trk}}$ and computes $E_{\text{Tower}}^{\text{eflow}}$ given by

$$E_{\text{Tower}}^{\text{eflow}} = \max(0, \Delta_{\text{ECAL}}) + \max(0, \Delta_{\text{HCAL}}). \quad (5.1)$$

1246 All reconstructed tracks result in a particle flow track. If $E_{\text{Tower}}^{\text{eflow}} > 0$ a particle flow tower is created with
1247 energy $E_{\text{Tower}}^{\text{eflow}}$. The particle flow tracks and jets are then used as input for the jet clustering algorithms.

1248 5.1.2 FCC-hh software

1249 FCC software (FCCSW) [89], common to all FCC studies (electron-electron, electron-hadron and hadron-
1250 hadron) has been developed and is maintained by the FCC study group. The software is based on Gaudi
1251 [90]. An FCC Event Data Model based on Podio [91] was also developed. It consists in specific classes
1252 that encode the information about the events.

1253 The FCC-hh study group is responsible for the generation of Monte Carlo quick simulation samples
1254 for the main benchmark processes for the FCC-hh. The samples are generated using the workflow
1255 described in the previous section. CERN users can request rights to run the EventProducer package
1256 [92] and produce samples for any desired process using the machinery that is already implemented. In
1257 addition, the FCC Event Data Model classes are directly accessible and can be used to read the ROOT
1258 files that are produced after the events are passed through Delphes.

1259 The machinery to submit jobs to CERN's batch system is also implemented for both the generation
1260 (MadGraph5) and reconstruction (Pythia8 plus Delphes3) levels.

1261 In this work we make use of this software in order to produce the necessary samples.

1262 5.2 Signal and background samples

1263 In this work we focus on the $hh \rightarrow b\bar{b}b\bar{b}$ channel and perform an analysis targeting the boosted kinematic
1264 region. The main backgrounds are multijet and $t\bar{t}$ production and the irreducible $pp \rightarrow b\bar{b}b\bar{b}$ process. This
1265 was introduced and motivated in chapter 1 and it is discussed in detail in chapter 6. Here we provide a
1266 technical description of how the signal and background samples were generated.

1267 5.2.1 MadGraph

1268 The irreducible background is generated with an extra jet with a high p_T at generator level, $4b+j$, where j
1269 stands for a light jet (initiated by a gluon or u, d, c, s quarks). This is referred to as the four flavor scheme.
1270 A high- p_T extra jet forces the four b quarks to have a high Lorentz boost and therefore increases the
1271 probability of the events being reconstructed with two large- R jets with a two-prong substructure. For this
1272 process, QCD and electroweak contributions are considered separately, i.e, we include three different
1273 types of samples: one in which only QCD processes are considered, one in which only electroweak
1274 processes are considered and one in which both process are considered simultaneously. The samples
1275 do not overlap. The $4b+j$ QCD sample is constituted by two independent samples that have a different
1276 generator level cut in the minimum p_T of the light jets, namely, $200 < p_{T,j}^{\min} < 500$ GeV and $p_{T,j}^{\min} > 500$
1277 GeV. This allows for a more efficient generation.

1278 The multijet background is simulated through $jj+0/1/2 j$ where j stands for a light or b jet (five flavor
1279 scheme). This background is divided into several individual samples that are produced in different H_T
1280 regions, where H_T is the scalar sum of the p_T of all partons at generator level. The minimum(maximum)
1281 allowed H_T is 500(100,000) GeV. Since these backgrounds are QCD processes, the p_T distribution of
1282 the final state jets falls very steeply as the p_T increases. Therefore, if one were to generate events for
1283 these processes without restricting the phase space, most events would consist of jets with a very low
1284 p_T which are exactly the type of events that are rejected the most by a boosted analysis (see chapter
1285 6 for more details on the event topology that is targeted and on the analysis strategy). As we move to
1286 regions of the phase with a higher H_T the cross section decreases meaning we need fewer MC events
1287 to properly simulate the background in that region.

1288 Note that for the $4b+j$ (QCD) and $jj+0/1/2 j$ samples we do not take into account the regions of the
1289 phase space with $p_{T,j} < 200$ GeV and with $0 < H_T < 500$ GeV. We assume that we can reject most of
1290 the events (if not all) with these kinematic characteristics by going to a sufficiently boosted region of the
1291 phase space. In addition, note that after the showering procedure there could be some overlap between
1292 the $4b+j$ and $jj+0/1/2 j$. This is taken care of in our analysis code: if an event from the $jj+0/1/2 j$
1293 has four b quarks at truth level [GIVE PERCENTAGE] then we do not consider it because it will certainly
1294 overlap with an event from the $4b+j$ sample.

1295 The $t\bar{t}$ background sample is generated with extra jets at generator level, $t\bar{t}+0/1/2 j$, using the five
1296 flavor scheme. We consider an inclusive sample for this background, meaning that we do not force any
1297 particular decay of the top quark or of the subsequent particles.

1298 For the hh SM signal sample, one of the Higgs is decayed to $b\bar{b}$ in MadGraph. The reasoning behind

1299 this choice is that most searches for Higgs pair production make use of a final state that includes at
 1300 least two b quarks in order to keep the cross section times BR of the process large enough. In addition,
 1301 this method allows the same generator level samples to be used to perform different analysis, simply by
 1302 choosing the decay channel of the remaining Higgs boson. The decay of the remaining Higgs boson
 1303 can be implemented in Pythia, in the case of this work, to $b\bar{b}$.

1304 The generator level cuts for the signal and background samples are summarized in table D.1 in
 1305 appendix D.

1306 Signal samples - BSM

1307 In addition to the SM di-Higgs signal, we also explore the signature and analysis sensitivity for di-Higgs
 1308 signals produced by two benchmark BSM models: CP-conserving type II 2HDM and a simplified dark
 1309 matter model (DM) with a spin 0 mediator. These models were described in section 2.2.

1310 Both models are readily available in FeynRules [93] (which is a Mathematica package for the imple-
 1311 mentation of new physics models) model database and can be straightforwardly implemented in Mad-
 1312 graph5. The parameters of the models, namely the masses of the new particles, can be changed by
 1313 the user. In the case of this work, we want new particles to have a large mass so that they produce SM
 1314 Higgs pairs with a high Lorentz boost.

1315 For the DM model [18], the spin 0 mediator's mass is set at 1 TeV. The cross section for the signal
 1316 generated with this model is smaller than the cross section of the SM signal (approximately 0.2 pb *versus*
 1317 0.7 pb) and therefore this model is not excluded by experimental data.

1318 For the 2HDM [94, 95], a finer tuning of the parameters is required because the model is very general
 1319 and has a lot external free parameters. In addition, it is written in the Higgs basis such that we need to
 1320 convert the parameters from the physical basis (introduced in 2.2) to this basis. The free parameters of
 1321 the model that we are interested in are the masses of the neutral, $m_{h_1}, m_{h_2}, m_{h_3}$, and charged scalars,
 1322 m_{hc} , the neutral scalars mixing angles, $mix_h, mix_{h_2}, mix_{h_3}$, the real and imaginary parts of the up, down
 1323 and charged lepton 3×3 Yukawa matrices, $GUR, GUI, GDR, GDI, GLR, GLI$ and the values (real and
 1324 imaginary parts) of the second, third and seventh quartic couplings, $l_{2,3,7,..}$. In the CP-conserving model
 1325 $h_{1,2,3}$ can be identified with the physical states h, H and A , respectively.

We start from the following parameters (in the physical basis):

$$\begin{aligned}
 m_h &= 125 \text{ GeV}, & m_H &= 900 \text{ GeV}, & m_A &= 850 \text{ GeV}, & m_{H^\pm} &= 800 \text{ GeV} \\
 \beta &= \frac{\pi}{4}, & \alpha &= -0.75 \\
 m_{12}^2 &= [(m_H^2 + m_A^2 + m_{H^\pm}^2)/3] \cos(\beta) \sin(\beta) \simeq 181041.6667. & (5.2)
 \end{aligned}$$

In the Higgs basis, the input parameters for the model are

$$\begin{aligned}
m_{h_1} &= 125 \text{ GeV}, & m_{h_2} &= 900 \text{ GeV}, & m_{h_3} &= 850 \text{ GeV}, & m_{hc} &= 800 \text{ GeV} \\
mix_{h_2} &= mix_{h_3} = 0 \\
mix_{h_1} &= \frac{\pi}{2} - (\beta - \alpha) \simeq 0.035 \\
l_2 &\simeq 0.27, & l_3 &\simeq 9.46, & l_7 &\simeq 0.46.
\end{aligned} \tag{5.3}$$

The masses of the scalars cannot change when going from one basis to the other. Therefore we set them to the exact same values. $mix_{h_2}, mix_{h_3} = 0$ because we are considering the CP-conserving model. To obtain the values of $l_{2,3,7}$ we use Eq. 11 from [24] we write the λ parameters of the scalar potential in terms of the parameters defined in Eq. 5.2. Then we use Eq. 47,48 and 50 from [96] to obtain the values of the quartic coupling in Higgs basis.

Regarding the Yukawa interactions, we work in the type II model. Following the type II restriction file found in [94] we set

$$\begin{aligned}
GLR &= GLI = GDI = GUI = 0 \\
GDR &= \text{diag} \left(0, 0, \frac{m_b \sqrt{2} \tan(\beta)}{v} \right) \\
GDR &= \text{diag} \left(0, 0, -\frac{m_t \sqrt{2}}{v \tan(\beta)} \right)
\end{aligned} \tag{5.4}$$

where $m_b = 4.7$ GeV and $m_t = 172$ GeV are the masses of the bottom and top quarks.

5.2.2 Pythia

For the signal samples (SM and BSM) we simply turn off all other decays except $h \rightarrow b\bar{b}$ therefore forcing the Higgs to decay to a pair of b quarks leading to the desired final state with four b quarks. All other settings are not altered with respect to their default configuration. For the BSM samples, this implies that the coupling of the SM Higgs boson to the b quarks is set to its SM value.

For the $jj + 0/1/2$ and $t\bar{t} + 0/1/2 j$ samples we have to perform jet matching because we require additional jets at the level of the matrix element. In addition to the partons generated in MadGraph and that can produce a jet, Pythia may introduce extra jets that are usually soft and collinear (with the particle from which they were radiated) and result from the showering process. This could lead to the same process (meaning processes with the same final states) being counted twice (double counting). Take, for example, the processes jj and $j jj$ at MadGraph level. It can happen that Pythia generates an extra jet for the first process but not for the second, leading to both processes having the same final state (three jets). Each process would then give its independent contribution to the total number of events but because they simply represent two distinct ways of achieving the same final state they should only be counted once. The goal of jet matching procedures is to avoid this problem.

The cross section times branching ratio (when applicable), the k-factors and the total number of

1348 events used in the analysis are summarized in table 5.1, for all samples. The k-factor multiplies the
 1349 cross section times branching ratio in order to reproduce known higher order results. It corresponds
 1350 only to the ratio between the total cross sections and it does not correct for possible differences that
 1351 might exist between the differential cross sections.

For the SM signal, $\sigma \times BR$ is given by $\sigma(hh, h \rightarrow b\bar{b}) \times BR(h \rightarrow b\bar{b})$, with $BR(h \rightarrow b\bar{b}) = 0.5824$ for $m_h = 125$ GeV [97]. $\sigma(hh, h \rightarrow b\bar{b})$ is given by:

$$\sigma(hh, h \rightarrow b\bar{b}) = \sigma(hh) \times 2 \times BR(h \rightarrow b\bar{b}) = 1.22 \text{ pb} \times 2 \times 0.5824 = 1.42 \text{ pb} \quad (5.5)$$

1352 where $\sigma(hh) = 1.22$ pb follows from Ref. [98] and the factor of 2 is a combinatorial factor that indicates
 1353 that both Higgs bosons can decay to a pair of b quarks. The k-factor is given by $\sigma_{\text{NNLL}}/\sigma_{\text{NNLO}}$, where
 1354 σ_{NNLL} is calculated according to the prescription given in equation I.7.8 of Ref. [97], with $\delta_t = -0.315$,
 1355 which yields $\sigma_{\text{NNLL}} = 1.33$ pb.

For the BSM signal samples, $\sigma \times BR$ is given by:

$$\sigma \times BR = \sigma(hh)_{\text{MG}} \times (BR(h \rightarrow b\bar{b}))^2 \quad (5.6)$$

1356 where $\sigma(hh)_{\text{MG5}}$ is the cross section for Higgs pair production as given by MadGraph. For these sample
 1357 we consider a k-factor of 1.0.

1358 For the remaining samples, $\sigma \times BR$ are the values given by MadGraph. In these samples no decay
 1359 mode is imposed, therefore the branching ratio is one. For the $4b + j(\text{QCD})$ sample, a k-factor of two
 1360 is applied [92] in order to parameterize our ignorance on the QCD irreducible background. For the
 1361 $t\bar{t} + 0/1/2 j$, a k-factor of 1.74 is applied, following Ref. [92].

1362 The parameters used in Pythia 8 can be found in table D.2 in appendix D.

1363 5.2.3 Delphes

1364 It is one of the main goals of this work to evaluate how the analysis sensitivity is influenced by the
 1365 granularity of the hadronic calorimeter. We start from the same MadGraph level samples and pass them
 1366 through Pythia and Delphes changing the settings of the Delphes card that correspond to the HCAL. All
 1367 other detector's parameters were kept unchanged with respect to the FCC default Delphes card. We
 1368 tested five benchmark granularity configurations:

- 1369 1. ATLAS HCAL granularity (as implemented in the standard ATLAS Delphes card);
- 1370 2. Starting from the ATLAS HCAL configuration we increase the granularity in $|\eta|$ by a factor of four,
 1371 in the pseudo rapidity range $|\eta| < 1.7$ which corresponds to the TileCal region;
- 1372 3. Starting from the FCC HCAL configuration we decrease the granularity in ϕ by a factor of two, in
 1373 the entire pseudo rapidity range covered by the HCAL.
- 1374 4. FCC HCAL default granularity (as implemented in the standard FCC Delphes card);

Table 5.1: Summary of the effective cross sections ($\sigma \times BR$) and k factors of the signal and background samples used in the analysis.

Sample	$\sigma \times BR$ [pb]	k-factor
$hh \rightarrow b\bar{b}b\bar{b}$ - SM	0.827	1.09
$hh \rightarrow b\bar{b}b\bar{b}$ - DM mediator	0.218	1.0
$hh \rightarrow b\bar{b}b\bar{b}$ - 2HDM type II	1.85	1.0
$4b + j$ (QCD, $200 < p_T^j < 500$)	756.4	2.0
$4b + j$ (QCD, $p_T^j > 500$)	57.71	2.0
$4b + j$ (QCD+EWK)	6.204	1.0
$4b + j$ (EWK)	0.07206	1.0
$jj + 0/1/2 j$ ($500 < H_T < 1000$)	1.64×10^7	1.0
$jj + 0/1/2 j$ ($1000 < H_T < 2000$)	1.67×10^6	1.0
$jj + 0/1/2 j$ ($2000 < H_T < 4000$)	1.32×10^5	1.0
$jj + 0/1/2 j$ ($4000 < H_T < 7200$)	7.32×10^3	1.0
$jj + 0/1/2 j$ ($7200 < H_T < 15000$)	4.75×10^2	1.0
$jj + 0/1/2 j$ ($15000 < H_T < 25000$)	7.35	1.0
$jj + 0/1/2 j$ ($25000 < H_T < 35000$)	0.176	1.0
$jj + 0/1/2 j$ ($35000 < H_T < 100000$)	0.00765	1.0
$t\bar{t} + 0/1/2 j$	4.31×10^4	1.74

- 1375 5. Starting from the FCC HCAL configuration we increase the granularity in $|\eta|$ and in ϕ by a factor of
 1376 two, in the entire pseudo rapidity range covered by the HCAL.

1377 The granularities of these five configurations are summarized in table 5.2. The values that are shown,
 1378 as well as the corresponding pseudorapidity regions, are exactly what is implemented in Delphes.

1379 In addition, we also passed the same generator level samples through the default ATLAS detector
 1380 simulation in Delphes. The HCAL granularity is the one that is indicated in table 5.2 but the other detector
 1381 parameters, such as the radius, magnetic field, tracking resolutions are the ones that are implemented
 1382 in the default ATLAS Delphes card. This additional detector configuration gives us an extra point in the
 1383 space of parameters that we are trying to explore. Furthermore, in a first, very crude, approximation,
 1384 it allow us to compare the results obtained at $\sqrt{s} = 100$ TeV to the ones obtained at $\sqrt{s} = 13$ TeV
 1385 by ATLAS. For completion we summarize, in table 5.3, the values of some key detector parameters as
 1386 implemented in Delphes for the ATLAS and FCC-hh detectors. The magnetic field is twice as strong for
 1387 the FCC-hh. The charged hadrons tracking efficiency and the HCAL resolution are fairly similar between
 1388 the two detector configurations.

Table 5.2: Summary of the benchmark granularity configurations of the HCAL.

Configuration	$\Delta\eta \times \Delta\phi$	η range
1 (ATLAS HCAL)	0.1×0.1	$ \eta < 2.5$
	0.2×0.2	$2.5 < \eta < 5.0$
2 (ATLAS HCAL $\eta \times 4$)	0.025×0.1	$ \eta < 1.7$
	0.1×0.1	$1.7 < \eta < 2.5$
3 (FCC HCAL $\phi/2$)	0.2×0.2	$2.5 < \eta < 5.0$
	0.025×0.05	$ \eta < 2.5$
4 (FCC HCAL)	0.05×0.1	$2.5 < \eta < 6.0$
	0.025×0.025	$ \eta < 2.5$
5 (FCC HCAL $\eta, \phi \times 2$)	0.05×0.05	$2.5 < \eta < 6.0$
	0.0125×0.0125	$ \eta < 2.5$
	0.025×0.025	$2.5 < \eta < 6.0$

Table 5.3: Summary of some key detector parameters for the FCC-hh and ATLAS detectors.

Parameter	FCC-hh	ATLAS
Radius of magnetic field coverage [m]	1.5	1.15
Half length [m]	5	3.51
Magnetic field [T]	4	2
Charged hadrons tracking efficiency	90% for $2.5 < \eta < 4.0$, $p_T > 1.0$	85% for $1.5 < \eta < 2.5$, $p_T > 1.0$
HCAL resolution	$\sqrt{E^2(0.03)^2 + E(0.60)^2}$ for $1.7 < \eta < 4.0$	$\sqrt{E^2(0.05)^2 + E(0.706)^2}$ for $1.7 < \eta < 3.2$

1389 **Chapter 6**

1390 **Analysis**

1391 **6.1 Overview of the $hh \rightarrow b\bar{b}b\bar{b}$ channel**

1392 For the SM Higgs, with a mass around 125 GeV, the branching ratio of the $hh \rightarrow b\bar{b}b\bar{b}$ decay is ap-
1393 proximately 33.6%, making it the most probable decay for Higgs pairs, as is illustrated in figure 6.1(a).
1394 However, in this channel, the main background is QCD multijet production that has a cross section sev-
1395 eral orders of magnitude larger than di-Higgs production in the SM, as table 5.1 shows. Nonetheless,
1396 the jet p_T distributions in this background have a very large yield close to zero and then fall very steeply
1397 while the signal has a much larger tail to high values of p_T . This indicates that searches targeting the
1398 boosted kinematic regime may be the key to measure $hh \rightarrow b\bar{b}b\bar{b}$ using inclusive production.

1399 In this work we target the boosted regime. In this kinematic region, the final state of the signal is
1400 characterized by two jets with a large radius parameter. Each jet is expected to contain the two b quarks
1401 originated from the decay of a Higgs boson, as figure 6.1(b) illustrates. Extra jets are also expected to
1402 be reconstructed as a consequence of QCD radiation.

1403 The analysis presented here is performed using the Monte-Carlo samples described in chapter 5. All
1404 samples assume $m_h = 125$ GeV. The event selection criteria are designed to optimize the significance,
1405 given by S/\sqrt{B} , where S and B represent the number of signal and background events, respectively.

1406 **6.1.1 Event pre-selection**

1407 We start by applying very simple and loose cuts that target events consistent with the boosted topol-
1408 ogy. Jets are reconstructed with the anti- k_T algorithm with an radius parameter $R = 0.8$. They are
1409 reconstructed from particle flow objects or calorimeter towers. Both approaches were explored in this
1410 analysis.

1411 We require at least two b-tagged $R = 0.8$ jets which corresponds to at least four b-tagged subjets,
1412 at least two in each $R = 0.8$ jet. The subjets are found through the soft drop mass technique that was
1413 described in section 3.3.2. The leading and sub leading jets must have $p_T \geq 200$ GeV in order for the
1414 event to be accepted. From Eq. 3.4, a Higgs boson with, e.g., $p_T = 200$ GeV leads to a pair of b quarks
1415 with $\Delta R \sim \frac{2m}{p_T} = 1.25$. Therefore, considering jet with $R = 0.8$ (diameter equal to 1.6) and $p_T \geq 200$ GeV

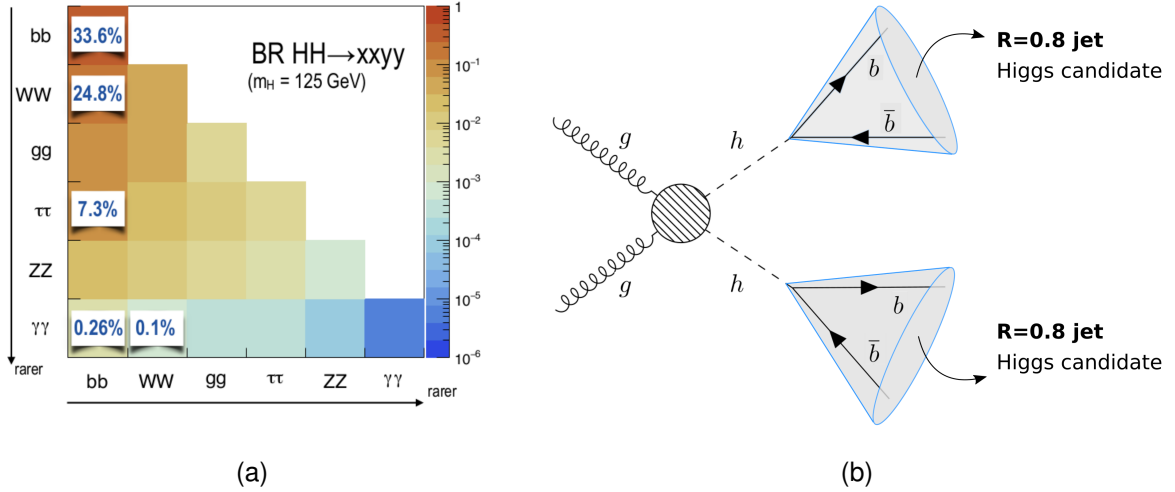


Figure 6.1: Higgs pairs branching ratios (left) and event topology targeted by this analysis (right).

is a reasonable choice. For a more complete description about the jet radius see appendix A. Due to the b-tagging parameterization (described in detail in section 6.2.1), there is a natural cutoff at $|\eta| = 4$ so we do not place any additional cut in η . From now on, these cuts are referred to as pre-selection cuts.

After the pre-selection cuts we can plot all the relevant distributions that allow us to characterize the signal and background events. These are shown in the next two sections. In addition, these distributions provide a first insight into the discriminating power of the kinematic and substructure variables that are explored.

6.1.2 Signal characterization

The cross section for di-Higgs inclusive production from pp collisions at 100 TeV is 1.22 pb [98]. This value is computed at NNLO accuracy. The dominant process is gluon-gluon fusion that has been extensively discussed in section 2.1.1. The signal process comprehends the di-Higgs inclusive production and the $hh \rightarrow b\bar{b}b\bar{b}$ subsequent decays. The total process cross section amounts to approximately 0.9 pb. This number includes the branching ratio and a k-factor to account for known NNLL results. This is described in detail in section 5.2.2. For an integrated luminosity of 30 ab^{-1} of proton-proton collisions at $\sqrt{s} = 100$ TeV we expect 2.7×10^7 events.

The Higgs candidates are reconstructed using large R jets that can be directly measured using information from the calorimeters and tracking systems. Figure 6.2(a) shows the $\Delta\phi$ between the two leading jets (Higgs candidates), $\Delta\phi(hh)$. For a large fraction of the signal events (red curve) $\Delta\phi(hh) \sim \pi$ which indicates that the jets are produced back-to-back in the transverse plane. There is also a small fraction of events for which the jets have $\Delta\phi(hh) \sim 1$. For these events there must be at least a third jet that balances the momentum of the jets pair.

Each wide jet is expected to be consistent with having two subjets associated with the two b quarks from the $h \rightarrow b\bar{b}$ decay. In the Higgs rest frame, the two subjets are produced back-to-back conserving momentum. In the laboratory frame, the ΔR between the subjets depends on the momentum of the

1440 Higgs boson, with larger ΔR corresponding to Higgs bosons with a lower momentum. This correlation
1441 between the ΔR between the subjets of the leading Higgs candidate ($\Delta R(b\bar{b})$) and its momentum
1442 ($p_T(h_1)$) is shown in figure 6.2(b).

1443 The p_T distributions of the leading and sub leading jets (Higgs candidates) are shown in figures
1444 6.5(a) and 6.5(b), respectively. The histograms are normalized to unit area in order to allow for shape
1445 comparison between them. For the leading jet, the signal p_T spectrum peaks at approximately 350 GeV
1446 and has a long tail for large values of p_T , in particular, longer than any of the backgrounds, at least up to
1447 $p_T > 1000$ GeV. For the sub leading jet the spectrum is softer, as expected, but the tail of the distribution
1448 is still longer than for any of the backgrounds. These distributions show that the signal process produces
1449 jets with larger transverse momenta than the jets produced by the background processes which indicates
1450 that a boosted analysis might perform well.

1451 The η distribution of the leading jet is shown in figure 6.6(a). This distribution is limited to $|\eta| < 4$
1452 because the b-tagging efficiency goes to zero for $|\eta| > 4$ (see section 6.2.1 for more details). The
1453 number of events decreases as we go to larger values of η which is due to the detector's acceptance.
1454 The η distribution of the sub leading jet is very similar to this one so we abstain from showing it here.

1455 The softdrop mass distribution of the leading jet is shown in figure 6.6(b). For the signal (red curve)
1456 there is a clear peak at approximately 120 GeV which corresponds to the SM Higgs boson mass peak.
1457 The peak is quite broad which means the mass resolution in this channel is not very good. On the one
1458 hand, this is because we are using large- R jets to reconstruct the Higgs candidates. These objects
1459 have a worse mass resolution than other cleaner objects such as photons or electrons. On the other
1460 hand, the cuts applied before plotting these distributions are very loose. As we place additional cuts the
1461 mass peak can be made slightly narrower. Another interesting feature of the signal mass spectrum is
1462 the existence of a peak close to zero. The explanation is the following: some jets do not contain both b
1463 quarks from the Higgs decay such that when applying the mass drop procedure only one b quark with a
1464 mass of approximately 5 GeV remains inside the jet, creating the peak at lower masses. A more detailed
1465 discussion, as well as a plot that supports this interpretation, can be found in appendix C.

1466 In addition to the basic kinematic distributions that we have just described, there are a multitude of
1467 other variables one can look at. Here we show the $\Delta\eta$ between the Higgs pairs, figure 6.7(a), and the
1468 τ_{21} variable for the leading Higgs candidate, figure 6.7(b). The first distribution shows that the Higgs pair
1469 tends to have a $\Delta\eta$ close to zero, which indicates that the pair is highly boosted in the longitudinal plane.
1470 The τ_{21} distribution shows that for the signal this variable takes values close to zero which means the jet
1471 is consistent with having two subjets.

1472 6.1.3 Backgrounds

1473 The relevant backgrounds for this analysis are QCD multijet production, $t\bar{t}$ and $b\bar{b}b\bar{b}$. Although the $b\bar{b}b\bar{b}$
1474 background is a particular case of a QCD multijet production process we consider it separately because
1475 it constitutes the irreducible background and therefore will have a higher efficiency in the analysis. The
1476 cross sections for these processes are several orders of magnitude larger than the cross section for the

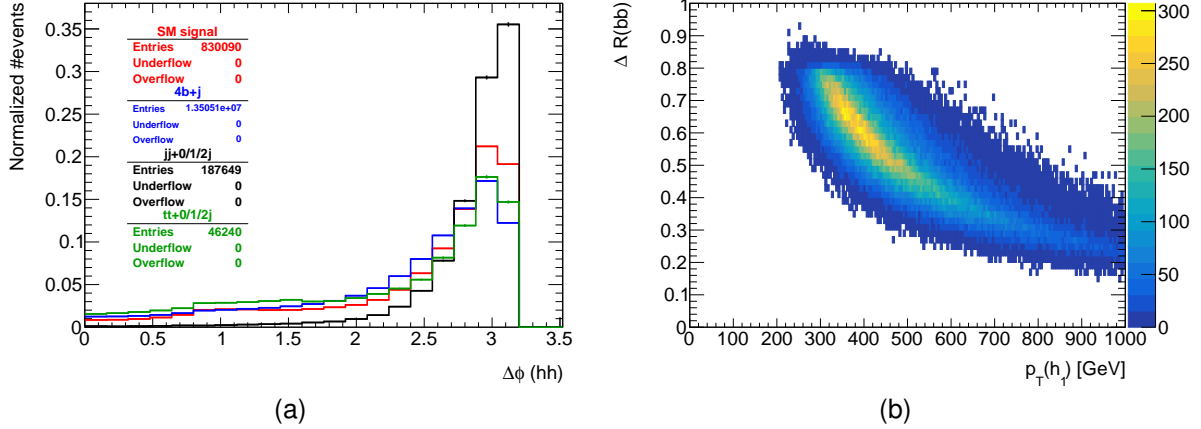


Figure 6.2: $\Delta\phi$ between the Higgs candidates, $\Delta\phi(hh)$, (left) and ΔR between the b quarks coming from the decay of the leading Higgs candidate, h_1 (right). To obtain this plot the cut $|M - 125| < 40$ GeV was applied in addition to the pre-selection cuts..

1477 signal, as table 5.1 shows. In addition, in the case of the $t\bar{t}$ background, the event topology is expected
 1478 to be similar to the signal because it also consists in the production of a pair of particles with the same
 1479 mass.

1480 The assumption that QCD multijet production and $t\bar{t}$ are the two main backgrounds is corroborated
 1481 by the ATLAS di-Higgs search performed in the same channel, where these backgrounds are found to be
 1482 the dominant ones. All other sources of backgrounds, including processes involving Higgs bosons, are
 1483 found to be negligible [65]. In appendix B we discuss and evaluate the importance of some backgrounds
 1484 that include Higgs bosons in our analysis.

1485 Figure 6.3 shows examples of LO Feynman diagrams that contribute to $4b + j$ (left), three (middle)
 1486 and four (right) light jets production. The $b\bar{b}b\bar{b}$ background is generated with an extra light jet at generator
 1487 level, as discussed in chapter 5. This jet boosts the four b quarks and has a minimum p_T of 200 GeV. This
 1488 increases the probability of two b quarks being reconstructed as single large- R jet therefore emulating
 1489 the signal's final state signature, i.e, high p_T jets compatible with a two-prong substructure. The QCD
 1490 $4b + j$ sample with $(200 < p_T < 500)$ GeV has a cross section of approximately 756 pb. In addition, as
 1491 explained in section 5.2.2, we multiply this cross section by a k-factor of 2, which yields a total cross
 1492 section of approximately 1.5×10^3 pb. The cross section is a lot smaller for the other $4b + j$ QCD sample
 1493 as well as for the samples that include both QCD and electroweak contributions, as expected.

1494 The QCD multijet background consists of two, three and four jet events (represented as $jj + 0/1/2 j$),
 1495 at generator level. The jets can originate from light and b quarks and from gluons. A jet matching pro-
 1496 cedure is implemented in Pythia in order to avoid double counting. Due to mis-tagging probabilities, light
 1497 and c jets can be identified as b jets. Although these probabilities are relatively small when compared
 1498 to the b-tagging efficiency (see section 6.2.1) the cross section of multijet processes is very large such
 1499 that this background becomes dominant. The $jj + 0/1/2 j$ sample with $(500 < H_T < 1000)$ GeV has
 1500 a cross section of the order of 10^7 GeV. As anticipated, the p_T spectrum of the multijet background is a
 1501 lot softer than for the signal and remaining backgrounds, as it is shown in figures 6.5(a) and 6.5(b). In

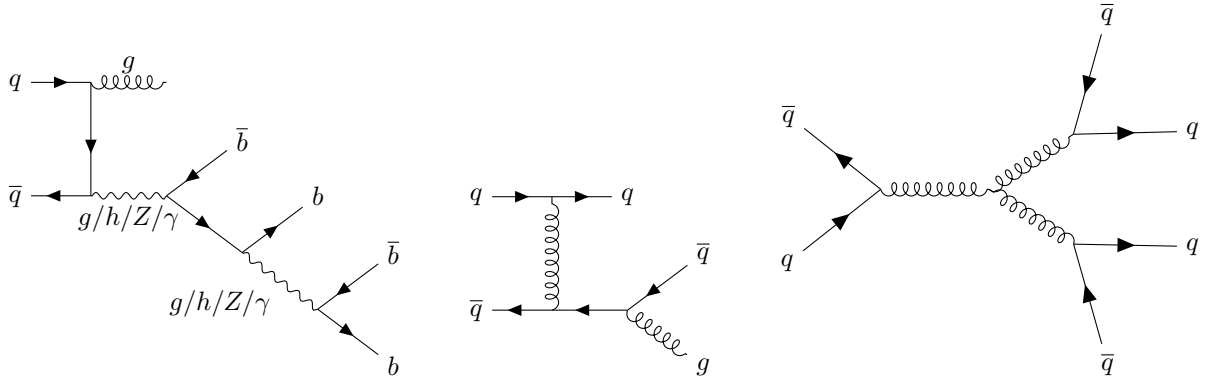


Figure 6.3: Example of diagrams that contribute to the QCD multijet background: five final state jets, four of which are b-jets (left), three final state jets (middle) and four final state jets (right). Here, q stands for a light quark/jet.

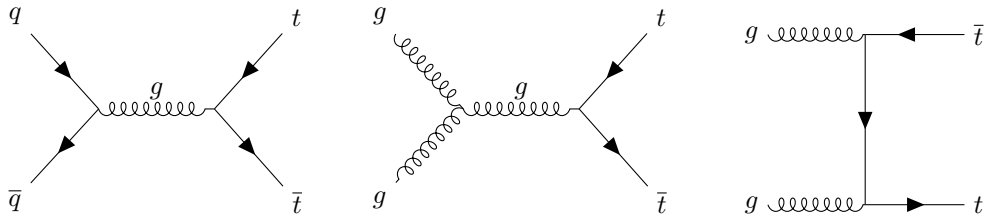


Figure 6.4: Dominant diagrams of $pp \rightarrow t\bar{t}$ at LO.

addition, for this background the τ_{21} variable takes values close to one, as it is shown in figure 6.7(b).
This indicates that the jets are not consistent with two subjets.

Figure 6.4 shows examples of LO Feynman diagrams that contribute to $t\bar{t}$ production through $q\bar{q}$ (left) and gg (middle and right) fusion. The $t\bar{t}$ background is simulated with additional zero, one or two jets (represented as $t\bar{t} + 0/1/2 j$), at generator level. The extra jets can originate from light and b quarks and from gluons. A jet matching procedure is implemented in Pythia in order to avoid double counting. The top quark has a very short life time, predicted to be 5×10^{-25} s, such that it decays before it can hadronize. This sample is inclusive in the top quark decay modes. However, the most favoured decay of the top quark is $t \rightarrow Wb$ with a branching ratio close to 96% [99]. Therefore, $t\bar{t}$ events will, most of the times, result in the $W^+W^-b\bar{b}$ final state. We do not specify any decay mode for the W such that the sample is also inclusive in the W decay modes. The W decays to hadrons ($W^+ \rightarrow q\bar{q}$) and leptons ($W^+ \rightarrow l^+\nu$) with $BR(W^+ \rightarrow q\bar{q}) \sim 68\%$ and $BR(W^+ \rightarrow l^+\nu) \sim 10\%$. If one (or both) W bosons decays to hadrons then there will be additional jets in the final state. These can be b jets or can be misidentified as such. If both W bosons decay to leptons there will still be at least two b jets in the final state, coming from the $t\bar{t}$ decay. The cross section of the $t\bar{t} + 0/1/2 j$ is approximately 4.3×10^4 pb. As explained in 5.2.2, k-factor of 1.74 is applied which yields a total cross section of approximately 7.5×10^4 pb.

It is interesting to note that in the softdrop mass plot for the leading Higgs candidate (figure 6.6(b)) the $t\bar{t}$ background (green line) shows a small peak around 170 GeV. In this region, all the decay products of the top quark are contained inside the $R = 0.8$ jet such that the jet mass corresponds to the mass of the original top quark.

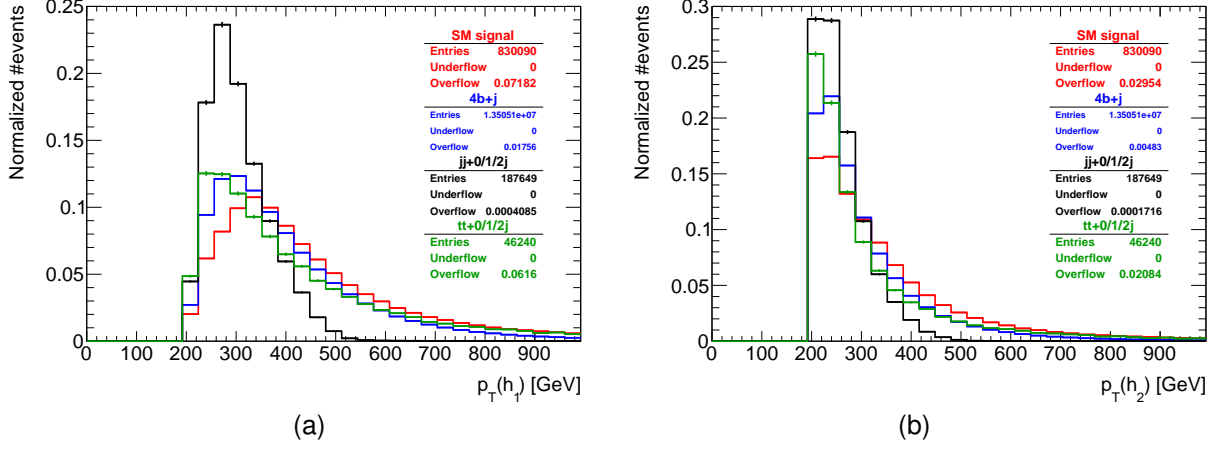


Figure 6.5: p_T distributions for the leading (left) and sub-leading (right) Higgs candidates. The signal is the SM $hh \rightarrow b\bar{b}$ process. The histograms are normalized to unit area.

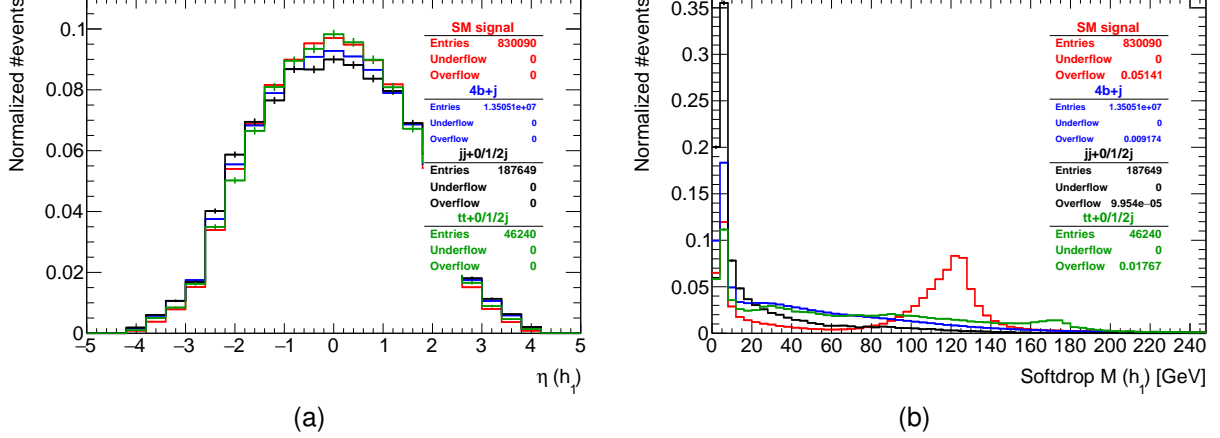


Figure 6.6: η distribution for the leading Higgs candidate (left) and softdrop mass distribution for the leading Higgs candidate (right). The signal is the SM $hh \rightarrow b\bar{b}$ process. The histograms are normalized to unit area.

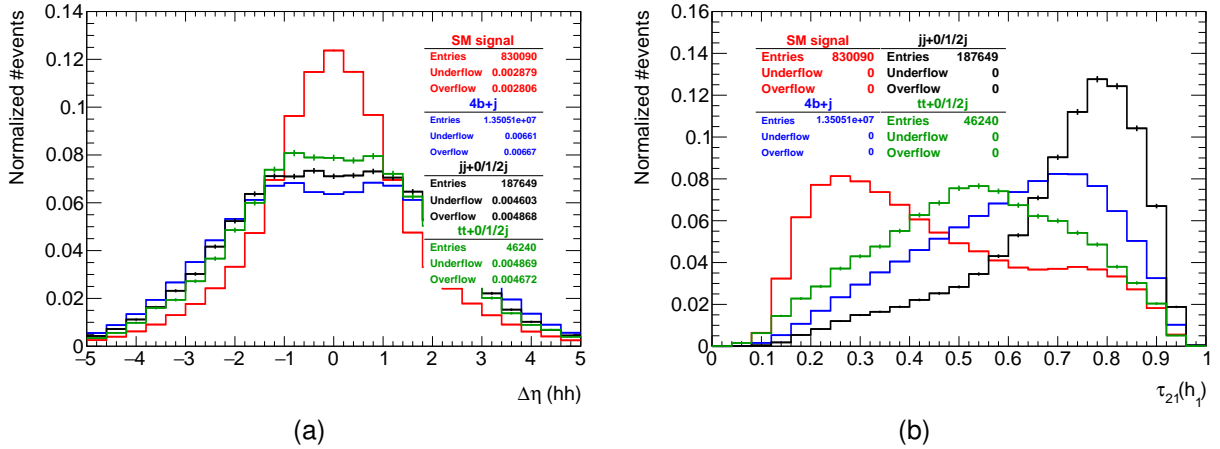


Figure 6.7: Distributions of the $\Delta\eta$ between the Higgs candidates (left) and of the τ_{21} variable for the leading Higgs candidate (right). The histograms are normalized to unit area.

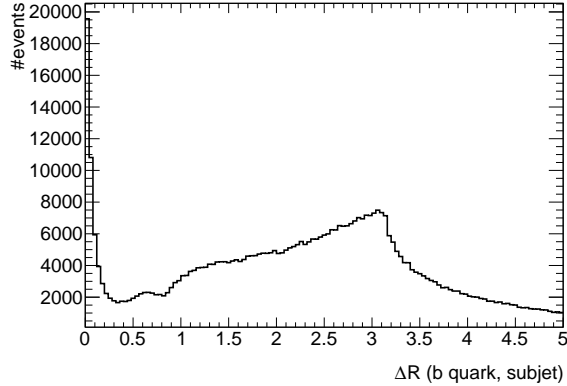


Figure 6.8: Minimum ΔR between b quarks and subjets of the $R = 0.8$ jets.

6.2 Analysis strategy

As already discussed, this analysis targets events in which at least two large- R jets are reconstructed. The jet with the highest momentum is assumed to correspond to the leading Higgs candidate and the jet with the second highest momentum to the sub leading one. Both the leading and sub leading jets must be b-tagged in order for the event to be accepted.

The events are reconstructed using particle flow (or eflow) or pure calorimeter jets (we explored both approaches) with $R = 0.8$, clustered with the anti- k_T algorithm. We perform the b-tagging of jets using truth level information as it is described in the following section. Jets with a large- R parameter cannot be b-tagged using Delphes default algorithm because the tagging of large R jets is an ambiguous task that can be performed in several different ways. Therefore, we implemented our own b-tagging algorithm that is described in section 6.2.1.

In this section, we present the baseline analysis based on cuts on the kinematic and substructure variables. An optimized version of the analysis is also presented and compared to the baseline. The optimization is based on plots of the significance (S/\sqrt{B}) as a function of the cut on a given variable. We also briefly describe how statistical uncertainties are taken into account.

6.2.1 Implementation of b-tagging

For each jet, the two hardest subjets are found using the mass drop procedure. It might happen that there are not two subjets because the algorithm's criteria are not met. In that case, the jet is rejected. We compute the ΔR distance between all b and c quarks in the event with Pythia 8 status equal to 23 and with $p_T > 10$ GeV and each subjet ($\Delta R(\text{subjet,parton})$). According to the Pythia manual, particles with status 23 result directly from the hardest subprocess. We consider that a subjet is matched to a given quark if $\Delta R(\text{subjet,parton}) < 0.3$, as indicated by the plot in figure 6.8. If the subjet is matched to at least a b quark, we b-tag the subjet with a given probability. If the subjet is not matched to any b quark but it is matched to at least one c quark we apply a c mistag rate. If the subjet is not matched to any b or c quark we apply a light mis tag rate. The b-tag probability and mistag rates were obtained from the Delphes FCC-hh card. They depend on the momentum of the jet and on its η coordinate. They are

Table 6.1: b-Tagging (black), c (blue) and light (red) mistag probabilities as a function of η and p_T of the (sub)jet. The momentum dependent factor, $(1 - p_T/15000)$, is common to the three probabilities.

$\eta \backslash p_T$	$10 < p_T < 500$	$500 < p_T < 15000$
$ \eta < 2.5$	0.85; 0.05 ; 0.01	$(0.85; \textcolor{blue}{0.05}; \textcolor{red}{0.01}) \times (1 - p_T/15000)$
$2.5 < \eta < 4.0$	0.64; 0.03 ; 0.0075	$(0.64; \textcolor{blue}{0.03}; \textcolor{red}{0.0075}) \times (1 - p_T/15000)$

1548 summarized in table 6.1. The b-tagging probabilities are given in black and the c and light mis tagging
 1549 probabilities are given in blue and red, respectively. Note that a jet cannot be b-tagged if $|\eta| > 4$ or if its
 1550 momentum is smaller than 10 GeV or larger than 15000 GeV.

1551 In terms of the technical implementation, the b-tagging algorithm works as follows: for each subjet we
 1552 look for a truth-level b quark within $\Delta R = 0.3$ of the subjet and calculate the b-tagging and mis-tagging
 1553 efficiencies using the expressions in table 6.1, where p_T and η refer to the subjet. If a b quark is found we
 1554 generate a random number between 0 and 1. If it smaller than the b-tagging efficiency we consider the
 1555 subjet to be b-tagged. If the subjet is not b-tagged we look for truth-level c quarks within $\Delta R = 0.3$ of the
 1556 subjet. If one is found we generate a new random number between 0 and 1 and if the number is smaller
 1557 than the c mis-tag probability we consider the subjet to be b-tagged. If the subjet is not b-tagged we
 1558 generate a random number between 0 and 1 and consider the subjet b-tagged if the number is smaller
 1559 than the light mis-tag probability.

1560 6.2.2 Baseline analysis

1561 The analysis described in this section and later was developed using the sample simulated with the
 1562 default FCC-hh detector implementation. The same analysis selection was then applied to the samples
 1563 generated using the different detector configurations. This allows for a straightforward comparison of the
 1564 results in terms of the significances.

1565 As a first step, we implemented a baseline analysis based on rectangular cuts on kinematic and
 1566 substructure variables. Firstly, we apply cuts on the transverse momenta of the leading and sub leading
 1567 Higgs candidates, $p_T(h_1)$ and $p_T(h_2)$, and of the Higgs pair, $p_T(hh)$:

$$1568 \quad p_T(h_1) > 400 \text{ GeV}, \quad p_T(h_2) > 350 \text{ GeV}, \quad p_T(hh) > 100 \text{ GeV}. \quad (6.1)$$

1569 These cuts follow from both distributions shown in figures 6.9(a), 6.9(b) and 6.10(a) and guarantee that
 1570 we are choosing events for which the Higgs candidates are sufficiently boosted. In addition, a high
 1571 threshold for the p_T of the jets suppresses $t\bar{t}$ events because the decay products of the top quark are
 1572 reconstructed in a single jet. In a more realistic analysis, these cuts would also be dictated by the trigger
 1573 threshold.

1574 From figure 6.10(b) we then apply a cut on the τ_{21} of the leading Higgs candidate to select jets that

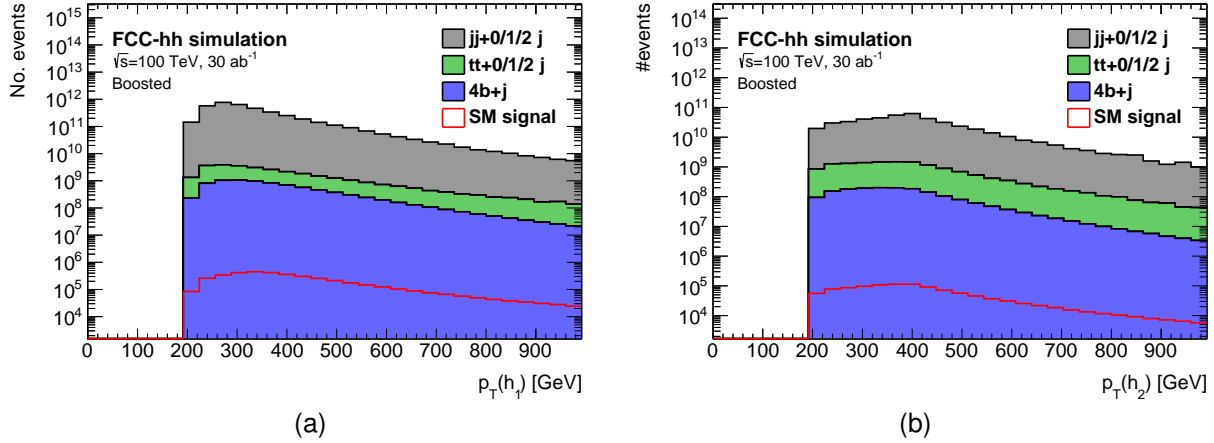


Figure 6.9: p_T distributions for the leading (a) and sub leading Higgs candidates (b). The histograms are normalized to $\mathcal{L} = 30 \text{ ab}^{-1}$.

are more compatible with a two-prong structure:

$$\tau_{21}(h_1) < 0.55. \quad (6.2)$$

The cut on this variable works as a Higgs tagging method. Therefore we apply the same cut on the τ_{21} of the sub leading Higgs candidate although that does not necessarily follow from the distribution of τ_{21} for the sub leading Higgs candidate (which can be found in figure F.1 in appendix F). Then, from the distribution in figure 6.11(a), we place a cut on the second Fox-Wolfram momentum (defined in section 3.3.1) of the leading Higgs candidate, $H_2(h_1)$:

$$H_2(h_1) > 0.2 \quad (6.3)$$

This substructure variable is particularly interesting because it helps suppress the $t\bar{t}$ background.

Finally, based on the distribution shown in figure 6.11(b), we apply a cut on the softdrop mass of both Higgs candidates, $M_{SD}(h_1, h_2)$. This cut is placed in a window around the nominal SM Higgs mass:

$$(100 \leq M_{SD}(h_1, h_2) \leq 135) \text{ GeV.} \quad (6.4)$$

Using this analysis, we achieve a significance, S/\sqrt{B} , of 5.1 ± 0.5 (stat.) ± 1.6 (sys.) (1.62 ± 0.16) (stat.) ± 0.8 (sys.)

for an integrated luminosity of 30 (3) ab^{-1} .

6.2.3 Optimization

The first approach to the optimization consists in placing successive cuts in the most relevant kinematic variables. The value of each cut is chosen in order to optimize the significance after that cut. As for the baseline analysis we start by looking at the transverse momenta of the leading and sub leading Higgs candidates. After the pre-selection cuts are applied, we scan the histograms of the p_T of the leading

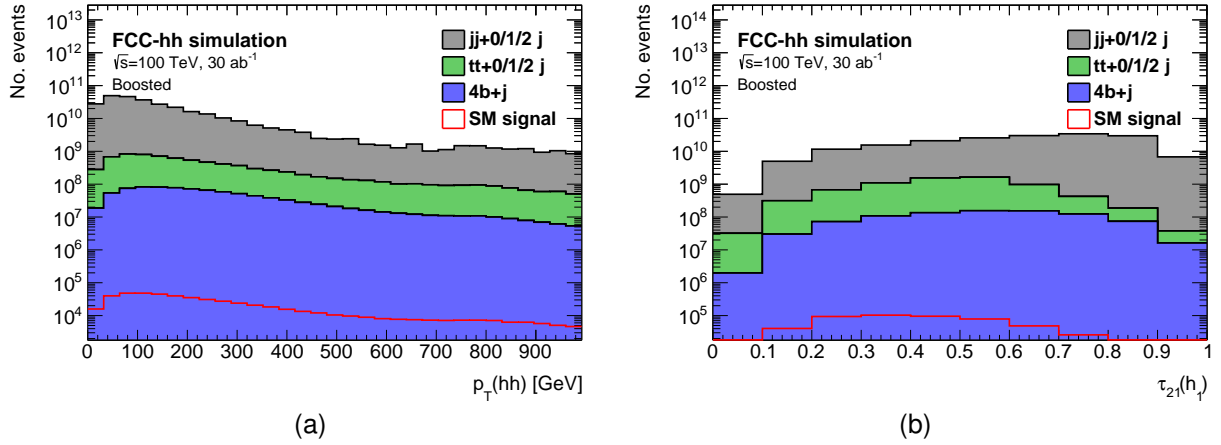


Figure 6.10: (a) p_T distribution for the Higgs pair, (b) τ_{21} variable for the leading Higgs candidate. The histograms are normalized to $\mathcal{L} = 30 \text{ ab}^{-1}$.

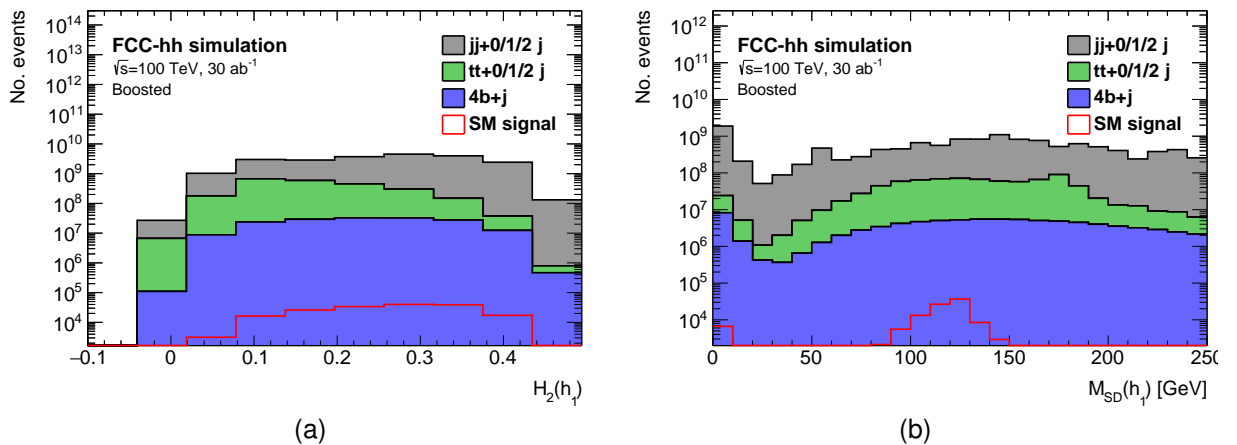


Figure 6.11: (a) H_2 variable for the leading Higgs candidate, (b) softdrop mass distribution for the leading Higgs candidate. The histograms are normalized to $\mathcal{L} = 30 \text{ ab}^{-1}$.

Higgs candidate for signal and backgrounds by placing a lower cut on this variable. For each value of the cut we integrate upwards in order to obtain the expected number of signal and background events after the cut. Using these numbers we calculate the significance, S/\sqrt{B} . The significance as a function of the lower cut on $p_T(h_1)$ is shown in figure 6.12(a). Based on this plot we choose the cut:

$$p_T(h_1) > 300 \text{ GeV}. \quad (6.5)$$

After placing the cut on $p_T(h_1)$ we do the same plot for the p_T of the sub leading Higgs candidate and of the Higgs pair. These are shown in figures 6.12(b) and 6.13(a), respectively. From figure 6.12(b) we see that a cut on $p_T(h_2)$ above 200 GeV is not favorable. Therefore, we do not apply any other cut on this variable. Based on the plot in figure 6.13(a) we choose the cut:

$$p_T(hh) > 100 \text{ GeV}. \quad (6.6)$$

Following the cuts on the momenta we place a cut on the τ_{21} variable for both Higgs candidates. From all the variables considered during the optimization process this was the one that lead to the highest increase in the significance. From the definition of the τ_{21} variable we expect the signal to take lower values than the background. Therefore we optimize the cut on this variable by placing an upper cut and integrating the distribution backwards. The plot is shown in figure 6.13(b). From this plot we place the following cut on the τ_{21} of the leading Higgs candidate:

$$\tau_{21}(h_1) < 0.4. \quad (6.7)$$

1574 We apply exactly the same cut on the τ_{21} of the sub leading Higgs candidate. This guarantees that both
1575 jets are consistent with having two subjets and therefore are more likely to originate from the decay of a
1576 Higgs boson.

Next we apply cuts on the $\Delta\eta$ between the Higgs candidates and on the second Fox-Wolfram momentum of the leading Higgs candidates, in this order:

$$|\Delta\eta(hh)| < 1.5 \quad H_2(h_1) > 0.2. \quad (6.8)$$

1577 These cuts follow from the plots on figures 6.14(a) and 6.14(b). The optimization plot for $\Delta\eta(hh)$ is
1578 obtained placing a cut in a window around zero which follows directly from the shape of the distributions
1579 in figure 6.7(a). For the $H_2(h_1)$ variable the cut is placed on the lower value.

1580 Finally we apply the mass cuts on the leading and sub leading Higgs candidates. These are the
1581 same that were applied in the baseline analysis.

1582 Using the optimized analysis we obtain a significance, S/\sqrt{B} , of 8.8 ± 1.6 (stat.) $^{+4.4}_{-3.4}$ (sys.) $(2.36 \pm$
1583 0.32 (stat.) $^{+1.4}_{-1.1}$ (sys.)) for an integrated luminosity of 30 (3) ab^{-1} . This corresponds to an improvement of
1584 approximately 70% with respect to the baseline analysis. This percentage is calculated as $((S/\sqrt{B})_{\text{opt.}} -$
1585 $(S/\sqrt{B})_{\text{base.}})/(S/\sqrt{B})_{\text{base.}}) \times 100$.

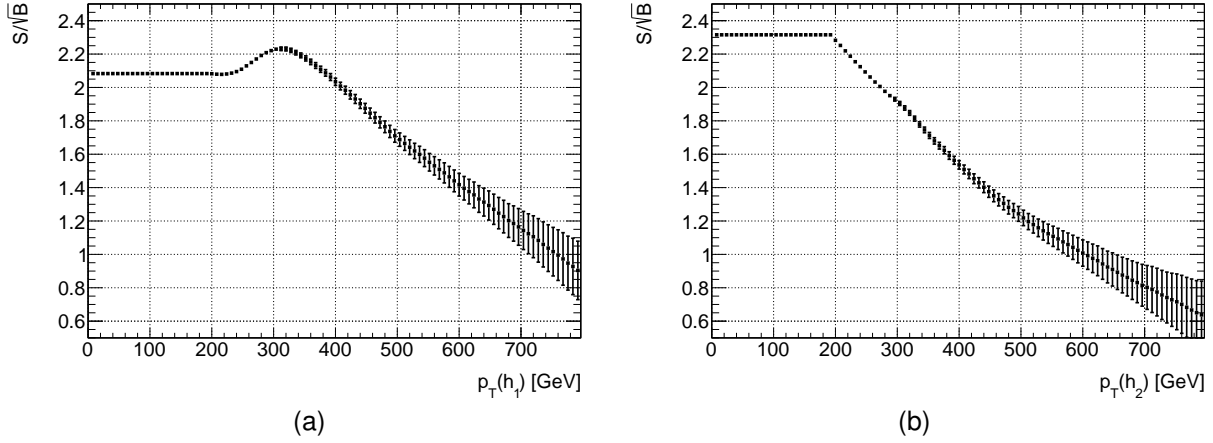


Figure 6.12: S/\sqrt{B} as a function of the cut on the p_T of the leading Higgs candidate, $p_T(h_1)$ (left) after the pre-selection cuts and of the sub leading Higgs candidate, $p_T(h_2)$ (right) after the cut on $p_T(h_1)$.

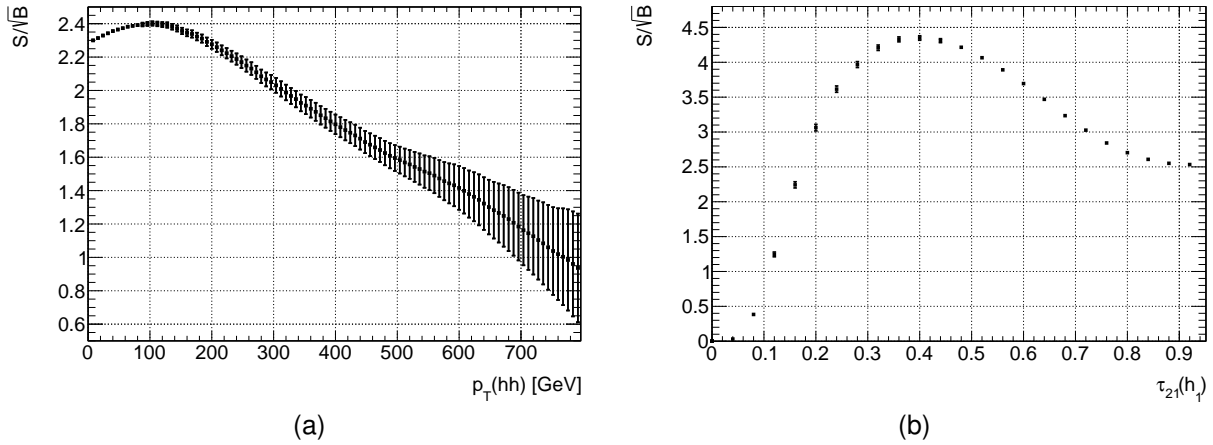


Figure 6.13: S/\sqrt{B} as a function of the cut on the p_T of the Higgs pair, $p_T(hh)$ (left) after the cut on $p_T(h_1)$ and as a function of the τ_{21} variable for leading Higgs candidate, $\tau_{21}(h_1)$ (right) after the cut on $p_T(hh)$.

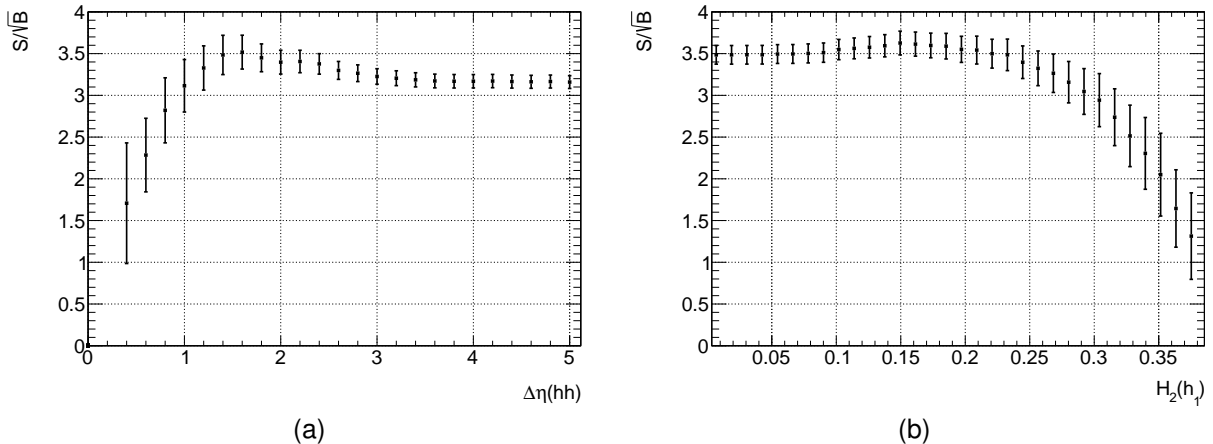


Figure 6.14: S/\sqrt{B} as a function of the cut on the $\Delta\eta$ between the Higgs candidates, $\Delta\eta(hh)$ (left) after the cuts on the transverse momentums and on the τ_{21} variables and as a function of the second Fox-Wolfram momentum for the leading Higgs candidate, $H_2(h_1)$ (right) after the cuts on the transverse momentums, τ_{21} and $\Delta\eta$.

1586 **6.2.4 Handling of uncertainties**

1587 **Statistical uncertainties**

For challenging analyses such as this one, the backgrounds usually have a much larger cross section than the signal meaning that we need a lot of Monte Carlo events to properly simulate them. Most of the times it is not feasible to generate as much events as we would need for a given luminosity. This is the case with this work, namely because we are targeting very high luminosities (of the order of tens of ab^{-1}). Take for example the multijet sample with $500 < H_T < 1000$. The cross section is approximately 10^7 pb which means that we expect a total of 3×10^{14} events for an integrated luminosity of 30 ab^{-1} . It is not feasible, within the time frame of this work and with the available computational resources, to generate this number of events. Therefore, we apply a weight, w , to each event given by:

$$w = \frac{\mathcal{L} \times \sigma}{N} \quad (6.9)$$

1588 where \mathcal{L} is the target integrated luminosity, σ is the cross section of the sample and N is the number of
1589 MC events generated.

If we assume that the number of events follows a Poisson distribution then the standard deviation (or uncertainty) is given by \sqrt{N} where N is the mean number of events. In order to normalize the number of events to a given luminosity we need to multiply the mean value and the uncertainty by the respective weight such that the number of normalized events, including the uncertainty, $N_{\text{norm}} \pm \Delta N_{\text{norm}}$, is given by:

$$N_{\text{norm}} \pm \Delta N_{\text{norm}} = w \times (N \pm \sqrt{N}). \quad (6.10)$$

ΔN_{norm} can then be used in standard error propagation to compute the statistical uncertainty associated with any expression, in particular, with S/\sqrt{B} . The error associated with S/\sqrt{B} is given by:

$$\left(\Delta \frac{S}{\sqrt{B}} \right)_{\text{stat.}}^2 = \left| \frac{1}{\sqrt{B}} \right|^2 (\Delta S)^2 + \left| -\frac{S}{B^{3/2}} \right|^2 (\Delta B)^2 \quad (6.11)$$

where ΔS and ΔB are the uncertainties associated with the number of signal and background events. ΔB is given by:

$$(\Delta B)^2 = \sum_i (\Delta B_i)^2 \quad (6.12)$$

1590 where the index i runs over all independent backgrounds.

1591 **Systematic uncertainties**

1592 Systematic uncertainties are usually related to the detector specificities and object reconstruction tech-
1593 niques, which makes them difficult to list and quantify for a detector that is not yet built. Nonetheless,
1594 we can use the numbers for the systematic uncertainties that are reported for existing searches for
1595 $pp \rightarrow hh \rightarrow b\bar{b}b\bar{b}$ using the ATLAS detector.

1596 When requiring four b-tags, the largest uncertainty affecting the signal is the the b-tagging uncer-

1597 tainty (table 6 of Ref. [100]). It is of the order of 30%. We use this number to estimate the impact of the
 1598 b-tagging uncertainty on the analysis. For the background, the largest uncertainty comes from the esti-
 1599 mation of its yield and shape, according to the same reference. The reported value is 16%. However, a
 1600 study performed by the FCC study group [101] considers more conservative values for the uncertainties
 1601 on the $t\bar{t}$ and QCD di-jet backgrounds normalizations. The reported values are 20% for $t\bar{t}$ and 50% for di-
 1602 jet production. In this study, we use these numbers to estimate the impact of the systematic uncertainty
 1603 on the normalization of the backgrounds.

1604 To estimated the b-tagging systematic uncertainty, the number of signal events after all the analysis
 1605 cuts is varied by 30% up and down. This leads to an upper (lower) bound in the significance of 6.6 (3.6).

1606 The background normalization uncertainties are implemented by increasing and decreasing the k-
 1607 factor of each background by the corresponding percentage, with respect to what is given in table 5.1.
 1608 We vary the k-factors of the QCD multijet ($4b + j$ and $jj + 0/1/2 j$) and of the $t\bar{t}$ backgrounds individually.
 1609 For the $4b + j$ and $jj + 0/1/2 j$ backgrounds we consider the same uncertainty of 50% and the variations
 1610 are done simultaneously for both. This leads to an upper (lower) bound in the significance of 7.1 (4.2).
 1611 For the $t\bar{t}$ background we consider an uncertainty of 20% which leads to an upper (lower) bound in the
 1612 significance of 5.13 (5.09).

We assume that the three sources of systematic uncertainty are uncorrelated and therefore the
 respective variations can be added in quadrature. The statistical error is also added in quadrature.
 Therefore, the total uncertainty that is given by:

$$\left(\Delta \frac{S}{\sqrt{B}} \right)_{\text{sys.+stat.}}^2 = (\delta_{\text{b-tag}})^2 + (\delta_{\text{QCD bkg.}})^2 + (\delta_{t\bar{t} \text{ bkg.}})^2 + (\delta_{\text{stat.}})^2 \quad (6.13)$$

1613 where $\delta_{\text{b-tag}}$, $\delta_{\text{QCD bkg.}}$ and $\delta_{t\bar{t} \text{ bkg.}}$ are the variations with respect to the nominal value of the significance
 1614 caused by the b-tagging uncertainty and by the uncertainties on the normalization of the QCD multijet
 1615 and $t\bar{t}$ backgrounds, respectively. $\delta_{\text{stat.}}$ is the statistical uncertainty.

1616 6.2.5 Trigger discussion

1617

Chapter 7

1618

Results

1619 In this chapter we describe the main results of the search for $hh \rightarrow b\bar{b}b\bar{b}$ at the FCC-hh using two
1620 benchmark luminosities, 30 ab^{-1} and 3 ab^{-1} (section 7.1). The statistical analysis used to extract the
1621 signal strength and to set limits on the Higgs boson triple coupling is also discussed. In section 7.2 we
1622 show how the significance of the analysis varies as a function of the granularity of the HCAL and/or the
1623 detector configuration. We also compare the results obtained using particle flow and pure calorimeter
1624 jets.

1625

7.1 Di-Higgs discovery potential at the FCC-hh

1626 The event selection of the baseline analysis for the search for $hh \rightarrow b\bar{b}b\bar{b}$ at the FCC with the baseline
1627 detector design is summarized in tables 7.1 and 7.2 for the signal samples (SM, DM mediator and type
1628 II 2HDM) and for the background samples ($4b + j$, $jj + 0/1/2j$ and $t\bar{t}$), respectively.

1629 From table 7.1, we see that for the BSM models the signal efficiency is higher than for the SM. It
1630 varies from 0.422 in the SM, to 0.487 in the DM mediator model and to 1.342 in the type II 2HDM.

Considering the SM production of Higgs pairs, the achieved significance is

$$S/\sqrt{B} = 8.8 \pm 1.6 \text{ (stat.)} {}^{+4.4}_{-3.4} \text{ (sys.)} \quad (2.36 \pm 0.32 \text{ (stat.)} {}^{+1.4}_{-1.1} \text{ (sys.)}) \quad (7.1)$$

1631 for an integrated luminosity of 30 (3) ab^{-1} . For $\mathcal{L} = 30 \text{ ab}^{-1}$, the significance is above the 5σ threshold
1632 while for $\mathcal{L} = 3 \text{ ab}^{-1}$ it is above the 3σ threshold. These results indicated that with the entire dataset that
1633 is expected to be accumulated by the FCC-hh detector it should be possible to observe the production
1634 of Higgs pairs.

1635 For a signal model that includes a 1 TeV dark matter mediator that can decay to pairs of SM Higgs
1636 bosons the achieve significance is 2.3 ± 0.4 (stat.) ${}^{+1.2}_{-0.9}$ (sys.) (0.73 ± 0.13 (stat.) ${}^{+0.37}_{-0.28}$ (sys.)) for an
1637 integrated luminosity of 30 (3) ab^{-1} . The significance is well bellow the 3σ threshold for both luminosities.
1638 Therefore, we do not expect to be able to detect or exclude this signal at the FCC-hh. In this model, the
1639 coupling of the DM mediator to the Higgs pairs is small which means that the contribution from the box

Table 7.1: Cumulative efficiency, in percentage, of each event selection criterion for the signal samples (SM and 2HDM). The absolute value of expected events after some key selection cuts is shown in curved brackets. The number of expected events is normalized to $\mathcal{L} = 30 \text{ ab}^{-1}$. The double horizontal line marks the pre-selection cuts. These results were obtained using the FCC-hh baseline detector design, as implemented in Delphes by the FCC-hh study group.

Selection [FCC-hh]	SM	DM mediator	2HDM type II
Gen level	100 $(2704 \pm 12) \times 10^3$	100 $(65400 \pm 29) \times 10^2$	100 $(13977 \pm 7) \times 10^3$
$N(\text{b-tags}) \geq 4$	92.488	92.593	93.430
$p_T(j_1, j_2) \geq 200 \text{ GeV}$	16.602 $(4490 \pm 5) \times 10^3$	17.033 $(11140 \pm 12) \times 10^2$	33.975 $4734 \pm 4 \times 10^3$
<hr/>			
$p_T(j_1) \geq 300 \text{ GeV}$	13.521	14.007	20.869
$p_T(j_1 + j_2) \geq 100 \text{ GeV}$	10.933	11.301	22.863
$\tau_{21}(j_1, j_2) < 0.4$	1.309	1.410	3.952
$ \Delta\eta(hh) < 1.5$	1.071	1.154	3.479
$FW2(j_1) > 0.2$	0.989	1.064	3.276
$(100 < M_{SD}(j_1, j_2) < 135) \text{ GeV}$	0.446 $(1207 \pm 8) \times 10^2$	0.487 $(3188 \pm 20) \times 10$	1.666 $(2328 \pm 8) \times 10^2$

¹⁶⁴⁰ diagram dominates over the resonant production (s-channel diagram), just like in the SM.

For the type II 2HDM the achieved significance is

$$S/\sqrt{B} = 16.9 \pm 3.0 \text{ (stat.)} {}^{+8.5}_{-6.6} \text{ (sys.)} \quad (5.4 \pm 0.9 \text{ (stat.)} {}^{+2.7}_{-2.1} \text{ (sys.)}) \quad (7.2)$$

¹⁶⁴¹ for an integrated luminosity of $30 (3) \text{ ab}^{-1}$. These results indicate that it can be observed (or excluded) at ¹⁶⁴² the FCC-hh. The high efficiency of this signal sample through the cuts, reflected in the high significance ¹⁶⁴³ that is achieved, make it a very exciting and achievable benchmark.

¹⁶⁴⁴ 7.1.1 Statistical analysis

¹⁶⁴⁵ 7.1.2 Comparing with the ATLAS detector

¹⁶⁴⁶ The event selection of the search for $hh \rightarrow b\bar{b}b\bar{b}$ with the ATLAS detector at a CM energy of 100 TeV is ¹⁶⁴⁷ summarized in tables 7.3 and 7.4 for the signal and background samples, respectively.

¹⁶⁴⁸ It is interesting to compare the results obtained with the FCC-hh default detector simulation with the ¹⁶⁴⁹ ones obtained using the simulation of the ATLAS detector. These are summarized in table 7.5 in terms ¹⁶⁵⁰ of the achieved significance for an integrated luminosity of 30 ab^{-1} .

¹⁶⁵¹ For all the signal models, the significance increases approximately 30% going from the ATLAS de- ¹⁶⁵² tector to the FCC-hh. For the SM signal, nonetheless, using the ATLAS default detector configuration ¹⁶⁵³ the achieved significance is already above 5σ , for $\mathcal{L} = 30 \text{ ab}^{-1}$: $S/\sqrt{B} = 5.7 \pm 1.3 \text{ (stat.)} {}^{+3.1}_{-2.4} \text{ (sys.)}$.

Table 7.2: Cumulative efficiency, in percentage, of each event selection criterion for the background samples ($4b + j$, $jj + 0/1/2j$ and $t\bar{t}+0/1/2 j$). The absolute value of expected events after some key selection cuts is shown in curved brackets. The number of expected events is normalized to $\mathcal{L} = 30 \text{ ab}^{-1}$. The double horizontal line marks the pre-selection cuts. These results were obtained using the FCC-hh baseline detector design, as implemented in Delphes by the FCC-hh study group.

Selection [FCC-hh]	$4b + j$	$jj + 0/1/2j$	$t\bar{t}$
Gen level	100 $(49035 \pm 12) \times 10^6$	100 $(54698 \pm 13) \times 10^{10}$	100 $(22503 \pm 11) \times 10^8$
$N(\text{b-tags}) \geq 4$	75.819	3.963	53.495
$p_T(j_1, j_2) \geq 200 \text{ GeV}$	17.811 $(8734 \pm 5) \times 10^6$	0.742 $(4058 \pm 11) \times 10^9$	1.056 $(2377 \pm 11) \times 10^7$
<hr/>			
$p_T(j_1) \geq 300 \text{ GeV}$	12.744	0.422	0.718
$p_T(j_1 + j_2) \geq 100 \text{ GeV}$	10.901	0.245	0.617
$\tau_{21}(j_1, j_2) < 0.4$	0.256	0.002	0.037
$ \Delta\eta(hh) < 1.5$	0.130	0.001	0.024
$FW2(j_1) > 0.2$	0.105	0.001	0.014
$(100 < M_{SD}(j_1, j_2) < 135) \text{ GeV}$	0.007 $(341 \pm 10) \times 10^4$	0.00003 $(17 \pm 11) \times 10^7$	0.0007 $(149 \pm 28) \times 10^5$

Table 7.3: Cumulative efficiency, in percentage, of each event selection criterion for the signal samples (SM and 2HDM). The absolute value of expected events after some key selection cuts is shown in curved brackets. The number of expected events is normalized to $\mathcal{L} = 30 \text{ ab}^{-1}$. The double horizontal line marks the pre-selection cuts. These results were obtained using the ATLAS detector design, as implemented in Delphes.

Selection [ATLAS]	SM	DM mediator	2HDM type II
Gen level	100 $(27043 \pm 12) \times 10^3$	100 $(65400 \pm 29) \times 10^2$	100 $(13978 \pm 6) \times 10^3$
$N(\text{b-tags}) \geq 4$	88.690	88.787	89.643
$p_T(j_1, j_2) \geq 200 \text{ GeV}$	15.533 $(4201 \pm 5) \times 10^3$	15.941 $(10426 \pm 12) \times 10^2$	32.181 $(4498 \pm 4) \times 10^3$
<hr/>			
$p_T(j_1) \geq 300 \text{ GeV}$	12.599	13.061	29.141
$p_T(j_1 + j_2) \geq 100 \text{ GeV}$	10.185	10.526	21.523
$\tau_{21}(j_1, j_2) < 0.4$	1.139	1.220	3.411
$ \Delta\eta(hh) < 1.5$	0.891	0.960	2.930
$FW2(j_1) > 0.2$	0.796	858	2.684
$(100 < M_{SD}(j_1, j_2) < 135) \text{ GeV}$	0.333 $(901 \pm 7) \times 10^2$	0.360 $(2358 \pm 18) \times 10$	1.266 $(1770 \pm 7) \times 10^2$

Table 7.4: Cumulative efficiency, in percentage, of each event selection criterion for the background samples ($4b + j$, $jj + 0/1/2j$ and $t\bar{t}+0/1/2 j$). The absolute value of expected events after some key selection cuts is shown in curved brackets. The number of expected events is normalized to $\mathcal{L} = 30 \text{ ab}^{-1}$. The double horizontal line marks the pre-selection cuts. These results were obtained using the ATLAS detector design, as implemented in Delphes.

Selection [ATLAS]	$4b + j$	$jj + 0/1/2j$	$t\bar{t}$
Gen level	100 $(49035 \pm 15) \times 10^6$	100 $(54698 \pm 15) \times 10^{10}$	100 $(22503 \pm 9) \times 10^8$
$N(\text{b-tags}) \geq 4$	71.617	3.747	51.782
$p_T(j_1, j_2) \geq 200 \text{ GeV}$	16.299 $(7993 \pm 6) \times 10^6$	0.685 $(379 \pm 11) \times 10^9$	0.985 $(2215 \pm 9) \times 10^7$
<hr/>			
$p_T(j_1) \geq 300 \text{ GeV}$	11.627	0.390	0.669
$p_T(j_1 + j_2) \geq 100 \text{ GeV}$	9.932	0.227	0.574
$\tau_{21}(j_1, j_2) < 0.4$	0.234	0.003	0.031
$ \Delta\eta(hh) < 1.5$	0.113	0.001	0.019
$FW2(j_1) > 0.2$	0.082	0.001	0.010
$(100 < M_{SD}(j1, j2) < 135) \text{ GeV}$	0.005 $(253 \pm 11) \times 10^4$	0.00004 $(23 \pm 15) \times 10^7$	0.0007 $(160 \pm 24) \times 10^5$

Table 7.5: Significances achieved with the ATLAS and FCC-hh detector configurations for $\mathcal{L} = 30 \text{ ab}^{-1}$ for the three benchmark signal models: SM, 1 TeV DM mediator and 2HDM with $m_H = 900 \text{ GeV}$.

Signal sample	ATLAS	FCC-hh
SM	$5.7 \pm 1.3 \text{ (stat.)}$	$8.8 \pm 0.7 \text{ (stat.)}$
1 TeV DM mediator	$1.50 \pm 0.23 \text{ (stat.)}$	$2.3 \pm 0.4 \text{ (stat.)}$
2HDM type II	$11.3 \pm 1.7 \text{ (stat.)}$	$16.9 \pm 3.0 \text{ (stat.)}$

7.2 Hadronic calorimeter granularity studies for future colliders

In this section we present the results that allow us to compare the different detector configurations. In section 7.2.2, we show the results obtained with the baseline and optimized analyses. In the optimized analyses, the statistical fluctuations are higher because the $jj + 0/1/2 j$ background with $500 < H_T < 1000$, which has the largest statistical weight, is not rejected as efficiency. Therefore, the shapes of the plots are easier to discern for the baseline analyses.

7.2.1 Resolution of jet mass and N-subjetiness

The softdrop mass of the leading Higgs candidate for the SM signal sample is shown in figure 7.1(a) for the different detector configurations. The same plot is shown in figure 7.1(b) for calorimeter jets. It can be seen that the mass resolution increases as we increase the granularity. This effect is more pronounced when using pure calorimeter jets. In order to quantify this effect we use the full width at half maximum (FWHM). For particle flow (calorimeter) jets, the FWHM varies from 126 (130) for the ATLAS detector configuration to 124 (122) for the FCC granularity with $\eta, \phi \times 2$ which corresponds to a 1% (6%) effect.

The invariant mass of the Higgs pair is shown in figure 7.2 for the SM signal when using particle flow jets. The same distribution is shown for the DM mediator and 2HDM signals in figures 7.3(a) and 7.3(b), respectively. For the SM, the mass spectrum of the Higgs pair does not show any resonance. On the one hand, the production is dominated by the box diagram. On the other hand, even if we only had the contribution from the triangle diagram, the Higgs that decays to a pair of Higgs bosons has to be off shell, therefore we expect a broad spectrum. For the DM mediator model, there is an enhancement with respect to the SM for $M(hh) \sim 1$ TeV. This is due to the contribution of the 1 TeV DM mediator decaying to pairs of SM Higgs bosons. Nonetheless, the spectrum is still quite broad because the box diagram still gives a very large contribution. For the 2HDM, there is a clear peak at $M(hh) \sim 900$ GeV because resonant production dominates. The mass resolution of the resonances does not seem to increase as the granularity increases. This picture holds even when using HCAL jets.

The τ_{21} variable for the leading Higgs candidate for the SM signal (filled lines) and for the $4b + j$ background (dashed lines) is shown in figure 7.4(a) for the different detector configurations for particle flow jets. The same plot is shown in figure 7.4(b) for calorimeter jets. The separation between signal and background increases. This was expected because an increase in the granularity of the hadronic calorimeter should help resolve better the substructure of boosted jets. For particle flow jets, the distance between the maximum points of the two distributions varies from 0.4 for the ATLAS detector, ATLAS HCAL and ATLAS HCAL with $\eta \times 4$ to 0.44 for the FCC HCAL with $\phi/2$ and to 0.46 for the remaining configurations. For calorimeter jets the distance between the maximum is always smaller than when using particle flow jets, considering the same detector configuration. Therefore, the separation is always better when using particle flow jets. When using calorimeter jets, there is a larger difference in the shape of the distributions for the multiple detector configurations, particularly when going from the ATLAS granularity with $\eta \times 4$ to the FCC granularity with $\phi/2$.

1691 The separation is the largest between the signal and the $jj + 0/1/2 j$ background, as expected.
1692 For this background, the distance between the maximums of the distributions varies from 0.48 (24) to
1693 0.56 (0.48), for particle flow (calorimeter) jets.

1694 7.2.2 Signal efficiency and significance

1695 Figure 7.5(a) shows the signal efficiency for the three signal models: SM (filled squares), 1 TeV DM
1696 mediator (empty squares) and type II 2HDM with $m_H = 900$ GeV, for eflow jets. The same plot is
1697 shown in figure 7.5(b) for calorimeter jets. For eflow jets the efficiency increases as we increase the
1698 granularity, for all signal models. It varies approximately 30% between the lowest value (ATLAS default)
1699 and the highest value (FCC granularity with $\eta, \phi \times 2$). For HCAL jets, this tendency also exists with
1700 the exception of the first point which corresponds to the ATLAS default detector configuration. [WHY?
1701 OPTIMIZATION OF ATLAS?]. In addition, the efficiency changes more when using pure calorimeter jets.
1702 It varies by approximately 98% between the ATLAS detector configuration and the configuration with the
1703 FCC granularity and $\eta, \phi \times 2$. The efficiency is higher for both BSM models than for the SM. This is
1704 because these models were chosen to have very heavy particles decaying to a pair of highly boosted
1705 Higgs pairs.

1706 The significances achieved with the baseline analysis as a function of the detector configuration
1707 for the SM signal, the DM mediator model and the type II 2HDM are shown in figures 7.6(a), 7.7(a)
1708 and 7.8(a), respectively. The same plots are shown for the optimized analysis in figures 7.6(b), 7.7(b)
1709 and 7.8(b). The square markers refer to analysis performed using particle flow jets. The statistical
1710 uncertainty associated with each value of the significance is computed using standard error propagation
1711 and is shown as error bars. The grey blocks represent the total uncertainty. For the baseline analysis,
1712 regardless of the signal model considered, the significance changes by approximately 15% when going
1713 from the ATLAS detector configuration to the configuration with the FCC granularity increase by a factor
1714 of two in η and ϕ . For the optimized analysis the change is of approximately 54%.

1715 Motivated by the small change in significance over the range of configurations that were tested,
1716 we implemented exactly the same analysis but using HCAL jets instead of eflow jets. The results are
1717 shown in the same plots using triangular markers and with green error blocks. On the one hand, the
1718 achieved significance is always smaller when using HCAL jets because we are not making use of the
1719 tracking information. On the other hand, when using HCAL jets, the significance changes more over
1720 the configuration range. For the SM signal, it varies by approximately 80% when going from the ATLAS
1721 detector configuration to the configuration with the FCC granularity increase by a factor of two in η and
1722 ϕ . For the DM mediator model, this value is 77% and for the 2HDM it is 60%. These percentages refer
1723 to the baseline analysis. For the optimized analysis the change is between 60% and 70% depending on
1724 the signal model.

1725 All in all, given the large uncertainties it is hard to conclude on the tendency followed by the plots
1726 of the significance as a function of the detector configuration. Nonetheless, the significance does seem
1727 to increase as the granularity increases, which what was expected. As previously discussed, this effect

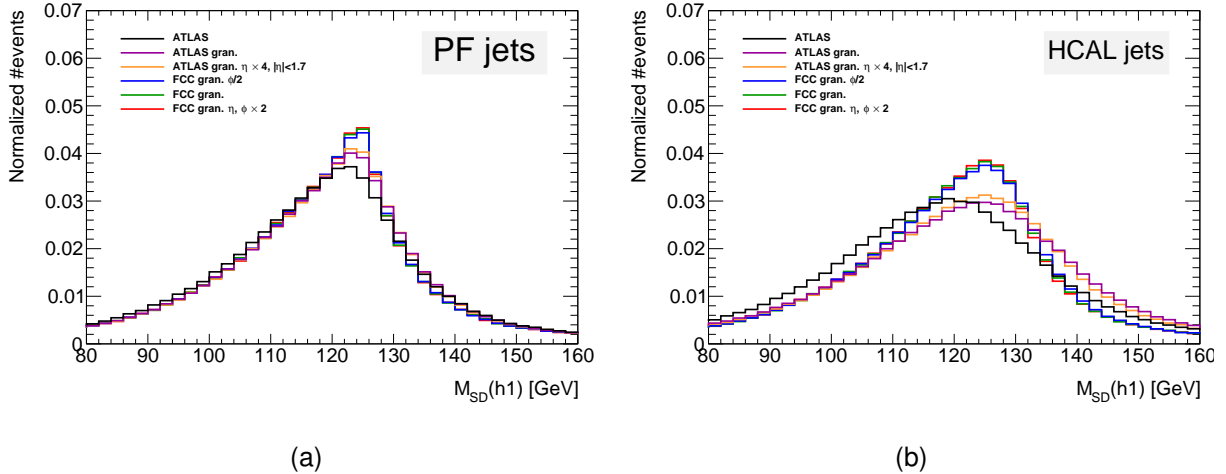


Figure 7.1: Leading Higgs candidate softdrop mass after the pre-selection cuts for particle flow (a) and calorimeter (b) jets. The colors indicate the different detector configurations. The x axis range is from 80 GeV to 160 GeV in order to make the differences between the histograms more clear.

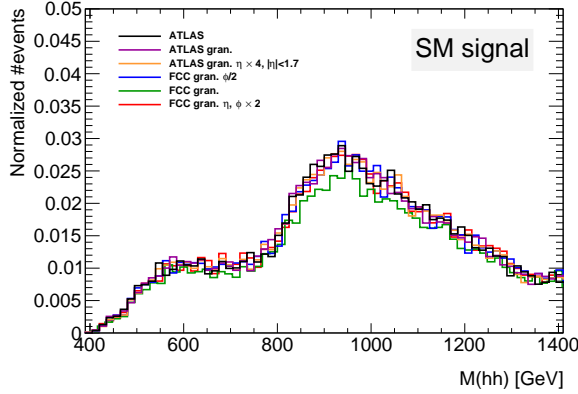


Figure 7.2: Invariant mass of the Higgs pair for the SM signal. The plots include the events that pass all the analysis cuts. The colors indicate the different detector configurations.

1728 is more accentuated when using pure calorimeter jets because we are only making use of the information
 1729 provided by the hadronic calorimeter and therefore the analysis is more sensitive to its transversal
 1730 segmentation (granularity).

1731 The small change in the significance when using eflow jets and the fact that the change increases
 1732 when using HCAL jets indicate that in the FCC-hh baseline detector design the resolution of the tracking
 1733 system is so good, in particular, so much better than the HCAL resolution that it is the limiting factor.

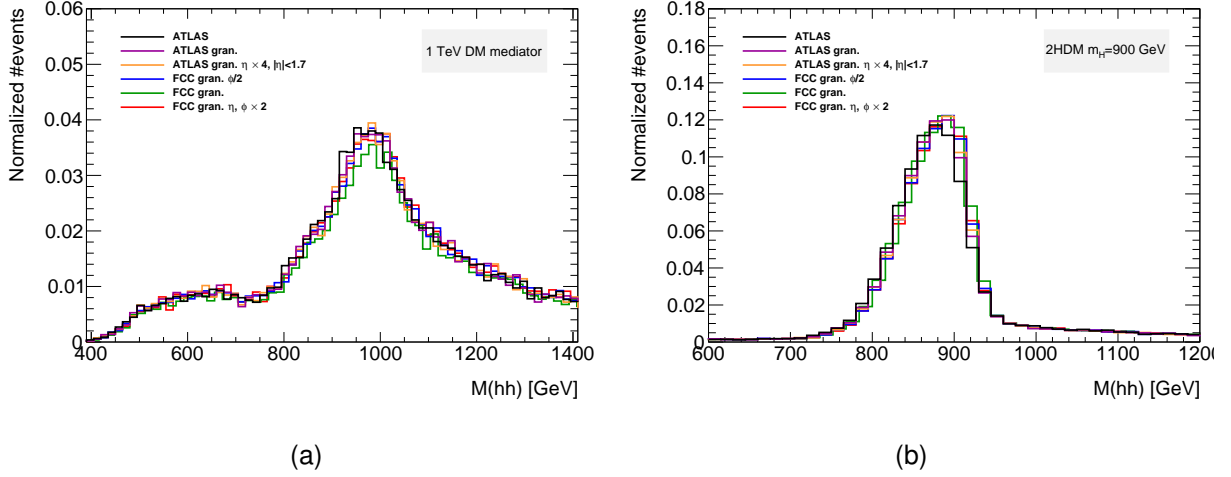


Figure 7.3: (a) Invariant mass of the Higgs pair for the 1 TeV DM mediator, (b) Invariant mass of the Higgs pair for the 2HDM with $m_H = 900$ GeV. The plots include the events that pass all the analysis cuts. The colors indicate the different detector configurations.

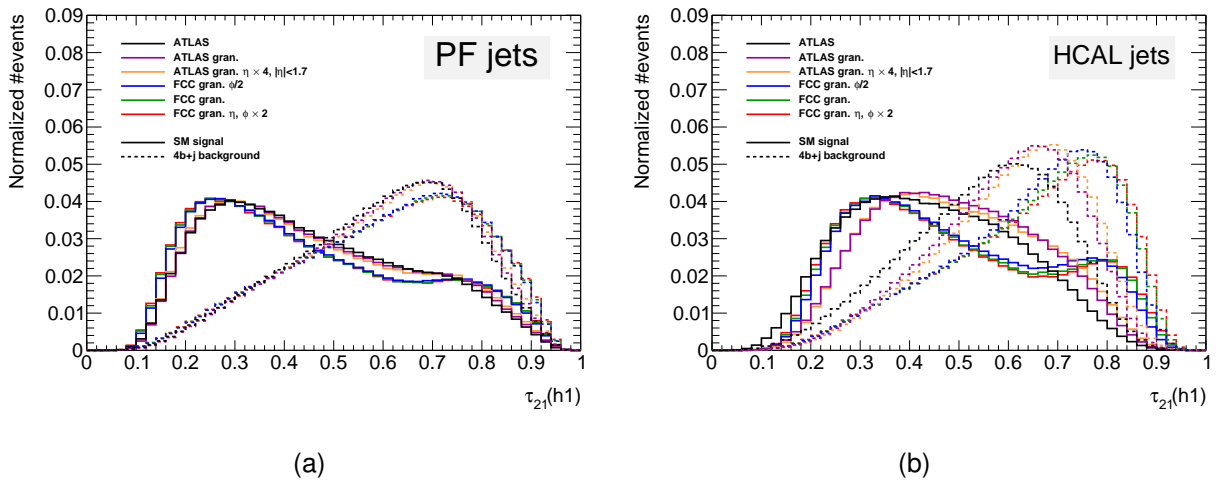


Figure 7.4: (a) Leading Higgs candidate τ_{21} distribution for eflow jets, (b) Leading Higgs candidate τ_{21} distribution for HCAL jets. The colors indicate the different detector configurations. The distributions are shown for the signal (filled lines) and for the $4b + j$ background (dashed lines).

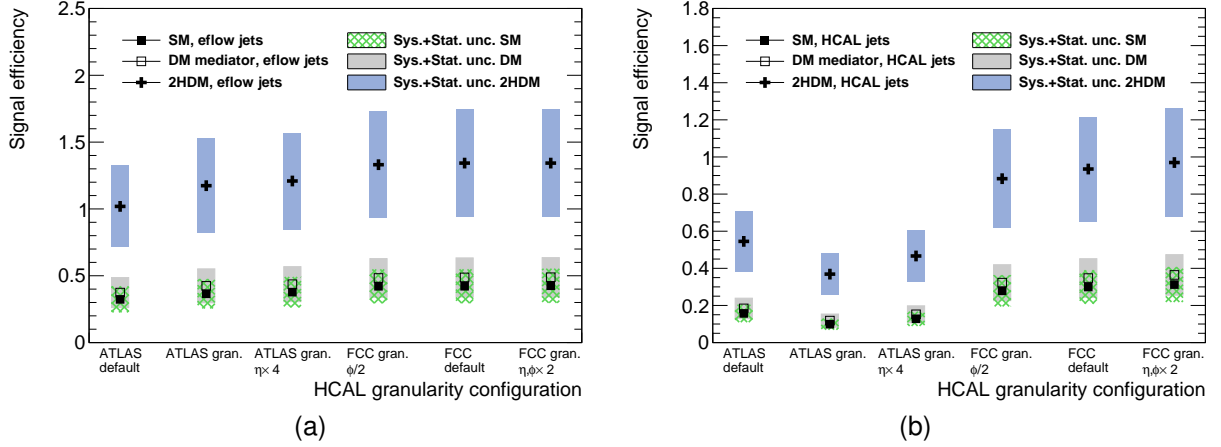


Figure 7.5: (a) Signal efficiency as a function of the detector configuration for particle flow jets, (b) Signal efficiency as a function of the detector configuration for calorimeter jets. Three signal models are shown: SM (filled squares), 1 TeV DM mediator (empty squares) and type II 2HDM with $m_H = 900$ GeV (crosses). The error bars are drawn but are smaller than the markers.

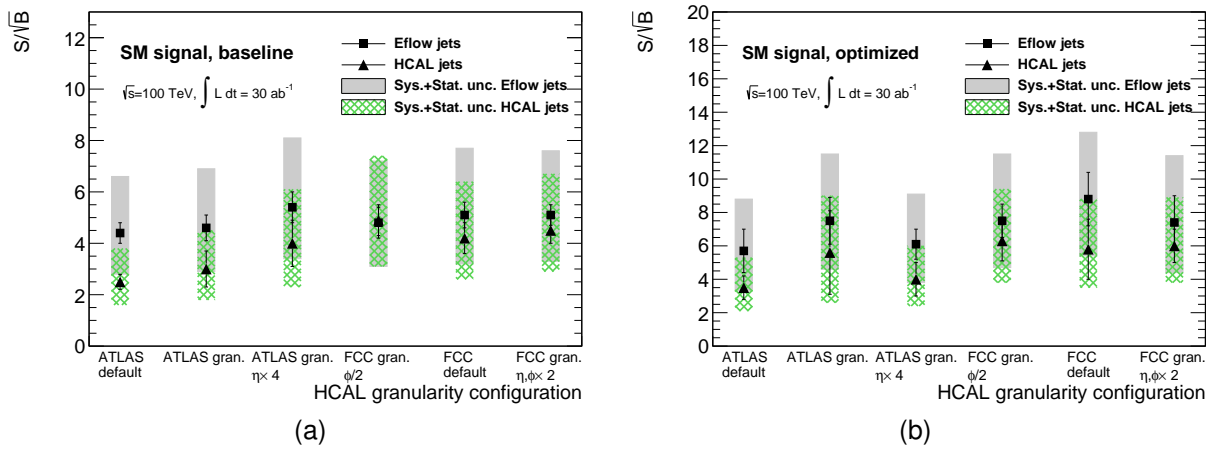


Figure 7.6: Significance as a function of the detector configuration for the SM signal, for the baseline (a) and optimized (b) analyses. The significances are shown for eflow jets (squares) and pure HCAL jets (triangles).

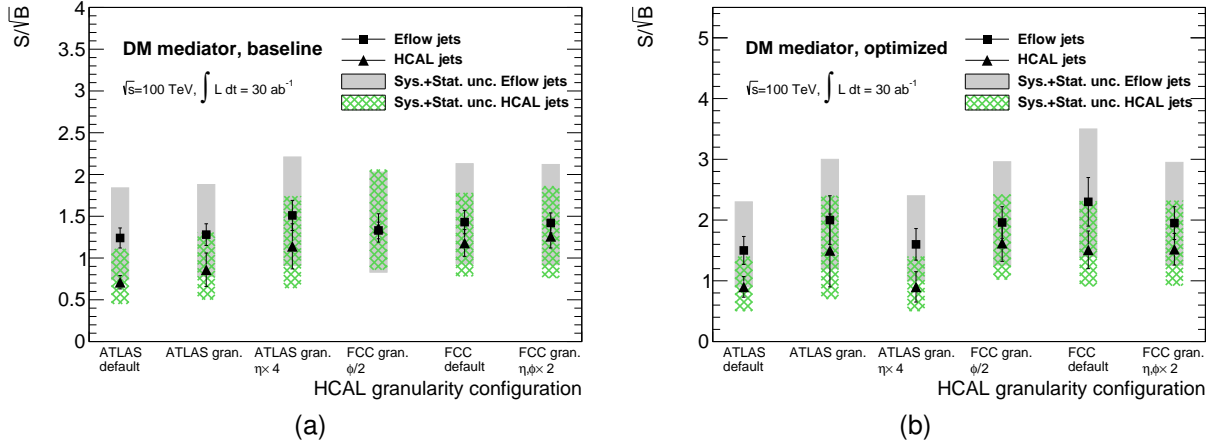


Figure 7.7: Significance as a function of the detector configuration for the DM mediator signal, for the baseline (a) and optimized (b) analyses. The significances are shown for eflow jets (squares) and pure HCAL jets (triangles).

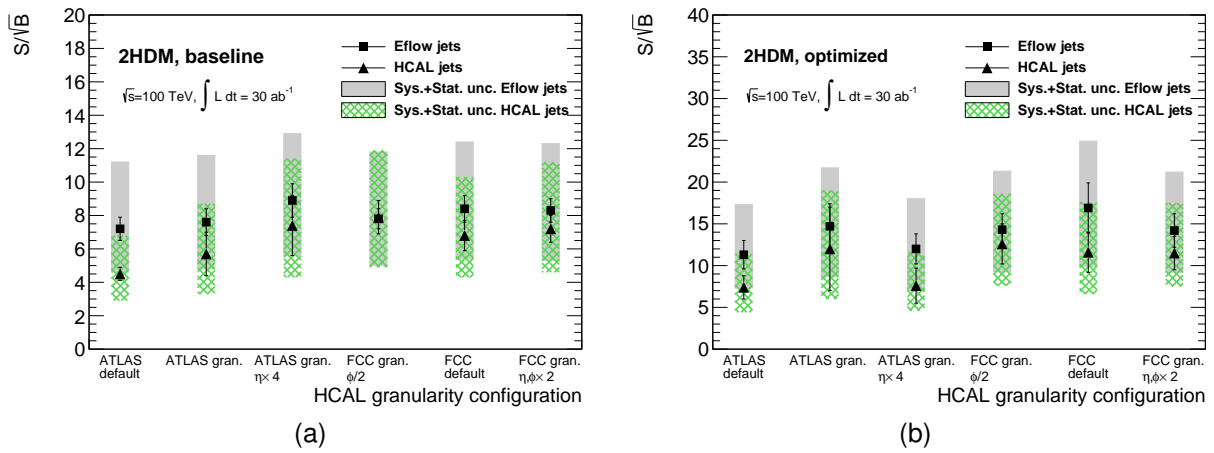


Figure 7.8: Significance as a function of the detector configuration for the 2HDM signal, for the baseline (a) and optimized (b) analyses. The significances are shown for eflow jets (squares) and pure HCAL jets (triangles).

¹⁷³⁴ Chapter 8

¹⁷³⁵ Conclusions

¹⁷³⁶ This thesis presented a feasibility study targeting the search for Higgs pair production in the $pp \rightarrow hh \rightarrow$
¹⁷³⁷ $b\bar{b}b\bar{b}$ channel at a center of mass energy of $\sqrt{s} = 100$ TeV. The analysis targeted a boosted kinematic
¹⁷³⁸ regime. The impact of the granularity of the hadronic calorimeter in the achieved significance was
¹⁷³⁹ analyzed.

¹⁷⁴⁰ The analysis consisted of a cut-based event selection designed to efficiently select signal events con-
¹⁷⁴¹ sistent with a boosted topology. In addition to standard kinematic variables, jet substructure variables,
¹⁷⁴² namely a ratio of N-subjetiness variables and a Fox-Wolfram momentum, are used to further suppress
¹⁷⁴³ the background. The analysis required the existence of at least two b-tagged large- R jets consistent
¹⁷⁴⁴ with having two subjets and with $p_T > 200$ GeV. Multijet production through QCD interactions and $t\bar{t}$
¹⁷⁴⁵ production constitute the main backgrounds.

¹⁷⁴⁶ In addition to SM Higgs pair production, two BSM benchmark processes were considered: a 1
¹⁷⁴⁷ TeV dark matter mediator and a heavy Higgs boson with $m_H = 900$ GeV in the framework of the
¹⁷⁴⁸ CP-conserving type II 2HDM, both decaying to pairs of SM Higgs bosons. The existence of heavy
¹⁷⁴⁹ resonances is expected to enhance Higgs pair production with respect to the SM.

¹⁷⁵⁰ For the hadronic Future Circular Collider (FCC-hh), the significance obtained was $S/\sqrt{B} = 8.8 \pm$
¹⁷⁵¹ 1.6 (stat.) (2.8 ± 0.5 (stat.)) for an integrated luminosity of $\mathcal{L} = 30$ (3) ab^{-1} . For $\mathcal{L} = 30 \text{ ab}^{-1}$, the
¹⁷⁵² value is above the observation threshold (5σ) which indicates that the full dataset that is expected to
¹⁷⁵³ be collected during the operation of the FCC-hh should be enough to claim the observation of Higgs
¹⁷⁵⁴ pair production, assuming SM production. For the CP-conserving type II 2HDM with $m_H = 900$ GeV,
¹⁷⁵⁵ the achieved significance was $S/\sqrt{B} = 16.9 \pm 3.0$ (stat.) (5.4 ± 0.9 (stat.)) for an integrated luminosity
¹⁷⁵⁶ of $\mathcal{L} = 30$ (3) ab^{-1} , which makes it an accessible benchmark for the HL-LHC and future colliders.
¹⁷⁵⁷ The achieved significance for the 1 TeV DM mediator is of order 1 even for an integrated luminosity of
¹⁷⁵⁸ $\mathcal{L} = 30 \text{ ab}^{-1}$, which makes it a very challenging benchmark and probably unaccessible even at future
¹⁷⁵⁹ high energy colliders.

¹⁷⁶⁰ With the ATLAS detector simulation, the achieved significance for the SM signal is $S/\sqrt{B} = 5.7 \pm$
¹⁷⁶¹ 1.3 (stat.) (1.8 ± 0.4 (stat.)) for an integrated luminosity of $\mathcal{L} = 30$ (3) ab^{-1} .

¹⁷⁶² The resolution of jet mass and the separation provided by the τ_{21} variable are shown to increase

1763 as the granularity of the HCAL increases. This effect is more evident when using pure calorimeter jets.

1764 [NUMBERS]

1765 When using particle flow jets, the change in the significance over the range of detector configurations
1766 tested is small, for all signal models. For the SM signal, it varies from X to Y, for an integrated luminosity
1767 of $\mathcal{L} = 30 \text{ ab}^{-1}$. This corresponds to a X% effect. Using pure calorimeter jets, the change in significance
1768 is more accentuated. It varies from X to Y for an integrated luminosity of $\mathcal{L} = 30 \text{ ab}^{-1}$, which corresponds
1769 to a X% effect. For the same detector configuration, the significance is always smaller when using
1770 calorimeter jets. The same qualitative conclusions hold for the BSM models. The effect of the granularity
1771 is of the same order of magnitude as for the SM.

1772 These results lead to the conclusion that the jet reconstruction performance is dominated by the
1773 tracking system.

Bibliography

- [1] J. Goldstone. Field Theories with Superconductor Solutions. *Nuovo Cim.*, 19:154–164, 1961. doi: 10.1007/BF02812722.
- [2] Y. Nambu and G. Jona-Lasinio. Dynamical Model of Elementary Particles Based on an Analogy with Superconductivity. 1. *Phys. Rev.*, 122:345–358, 1961. doi: 10.1103/PhysRev.122.345. [,127(1961)].
- [3] G. Arnison et al. Experimental Observation of Lepton Pairs of Invariant Mass Around 95-GeV/c**2 at the CERN SPS Collider. *Phys. Lett.*, B126:398–410, 1983. doi: 10.1016/0370-2693(83)90188-0. [,7.55(1983)].
- [4] G. Arnison et al. Experimental Observation of Isolated Large Transverse Energy Electrons with Associated Missing Energy at $s^{**}(1/2) = 540\text{-GeV}$. *Phys. Lett.*, B122:103–116, 1983. doi: 10.1016/0370-2693(83)91177-2. [,611(1983)].
- [5] F. Wilczek. Spontaneous symmetry breaking: General. <http://web.mit.edu/8.701/www/LectureNotes/8.701spontaneousSymmetryBreaking-GeneralFA13.pdf>, 2013. Accessed 2018-01-11.
- [6] P. W. Higgs. Broken Symmetries and the Masses of Gauge Bosons. *Phys. Rev. Lett.*, 13:508–509, 1964. doi: 10.1103/PhysRevLett.13.508. [,160(1964)].
- [7] F. Englert and R. Brout. Broken Symmetry and the Mass of Gauge Vector Mesons. *Phys. Rev. Lett.*, 13:321–323, 1964. doi: 10.1103/PhysRevLett.13.321. [,157(1964)].
- [8] G. S. Guralnik, C. R. Hagen, and T. W. B. Kibble. Global Conservation Laws and Massless Particles. *Phys. Rev. Lett.*, 13:585–587, 1964. doi: 10.1103/PhysRevLett.13.585. [,162(1964)].
- [9] R. Costa Batalha Pedro, J. Maneira, and P. Conde Muio. Search for the Higgs boson at ATLAS/LHC in WH associated production and decay to b quark pairs, Apr 2017. URL <https://cds.cern.ch/record/2304102>. Presented 09 Nov 2017.
- [10] C. S. Wu, E. Ambler, R. W. Hayward, D. D. Hoppes, and R. P. Hudson. Experimental test of parity conservation in beta decay. *Phys. Rev.*, 105:1413–1415, Feb 1957. doi: 10.1103/PhysRev.105.1413. URL <https://link.aps.org/doi/10.1103/PhysRev.105.1413>.

- 1801 [11] M. Goldhaber, L. Grodzins, and A. W. Sunyar. Helicity of neutrinos. *Phys. Rev.*, 109:
1802 1015–1017, Feb 1958. doi: 10.1103/PhysRev.109.1015. URL <https://link.aps.org/doi/10.1103/PhysRev.109.1015>.
- 1803
- 1804 [12] S. M. Bilenky and J. Hosek. GLASHOW-WEINBERG-SALAM THEORY OF ELECTROWEAK
1805 INTERACTIONS AND THE NEUTRAL CURRENTS. *Phys. Rept.*, 90:73–157, 1982. doi: 10.
1806 1016/0370-1573(82)90016-3.
- 1807 [13] R. Frederix, S. Frixione, V. Hirschi, F. Maltoni, O. Mattelaer, P. Torrielli, E. Vryonidou, and M. Zaro.
1808 Higgs pair production at the LHC with NLO and parton-shower effects. *Phys. Lett.*, B732:142–149,
1809 2014. doi: 10.1016/j.physletb.2014.03.026.
- 1810 [14] M. Mangano. *Physics at the FCC-hh, a 100 TeV pp collider*. CERN Yellow Reports: Monographs.
1811 CERN, Geneva, 2017. URL <https://cds.cern.ch/record/2270978>.
- 1812 [15] T. Plehn, M. Spira, and P. M. Zerwas. Pair production of neutral Higgs particles in gluon-
1813 gluon collisions. *Nucl. Phys.*, B479:46–64, 1996. doi: 10.1016/0550-3213(96)00418-X, 10.1016/
1814 S0550-3213(98)00406-4. [Erratum: Nucl. Phys.B531,655(1998)].
- 1815 [16] S. Borowka, N. Greiner, G. Heinrich, S. Jones, M. Kerner, J. Schlenk, U. Schubert, and T. Zirke.
1816 Higgs Boson Pair Production in Gluon Fusion at Next-to-Leading Order with Full Top-Quark Mass
1817 Dependence. *Phys. Rev. Lett.*, 117(1):012001, 2016. doi: 10.1103/PhysRevLett.117.079901, 10.
1818 1103/PhysRevLett.117.012001. [Erratum: Phys. Rev. Lett.117,no.7,079901(2016)].
- 1819 [17] S. Borowka, N. Greiner, G. Heinrich, S. P. Jones, M. Kerner, J. Schlenk, and T. Zirke. Full top
1820 quark mass dependence in Higgs boson pair production at NLO. *JHEP*, 10:107, 2016. doi:
1821 10.1007/JHEP10(2016)107.
- 1822 [18] H. C. van de Hulst, E. Raimond, and H. van Woerden. Rotation and density distribution of the
1823 Andromeda nebula derived from observations of the 21-cm line. 14:1, Nov. 1957.
- 1824 [19] Y. Fukuda et al. Evidence for oscillation of atmospheric neutrinos. *Phys. Rev. Lett.*, 81:1562–1567,
1825 1998. doi: 10.1103/PhysRevLett.81.1562.
- 1826 [20] Q. R. Ahmad et al. Measurement of the rate of $\nu_e + d \rightarrow p + p + e^-$ interactions produced by
1827 8B solar neutrinos at the Sudbury Neutrino Observatory. *Phys. Rev. Lett.*, 87:071301, 2001. doi:
1828 10.1103/PhysRevLett.87.071301.
- 1829 [21] Q. R. Ahmad et al. Direct evidence for neutrino flavor transformation from neutral current
1830 interactions in the Sudbury Neutrino Observatory. *Phys. Rev. Lett.*, 89:011301, 2002. doi:
1831 10.1103/PhysRevLett.89.011301.
- 1832 [22] B. Gripaios. Lectures on Physics Beyond the Standard Model. 2015.
- 1833 [23] N. M. A. 2018. Popular information, 2004. URL <https://www.nobelprize.org/prizes/physics/2004/popular-information/>.
- 1834

- 1835 [24] V. Branchina, F. Contino, and P. M. Ferreira. Electroweak vacuum lifetime in two Higgs doublet
1836 models. 2018.
- 1837 [25] J. F. Gunion and H. E. Haber. The CP conserving two Higgs doublet model: The Approach to the
1838 decoupling limit. *Phys. Rev.*, D67:075019, 2003. doi: 10.1103/PhysRevD.67.075019.
- 1839 [26] H. Sun, Y.-J. Zhou, and H. Chen. Constraints on large-extra-dimensions model through 125-
1840 GeV Higgs pair production at the LHC. *Eur. Phys. J.*, C72:2011, 2012. doi: 10.1140/epjc/
1841 s10052-012-2011-4.
- 1842 [27] P. Huang, A. Joglekar, M. Li, and C. E. M. Wagner. Corrections to di-Higgs boson production
1843 with light stops and modified Higgs couplings. *Phys. Rev.*, D97(7):075001, 2018. doi: 10.1103/
1844 PhysRevD.97.075001.
- 1845 [28] G. Aad et al. Observation of a new particle in the search for the Standard Model Higgs boson with
1846 the ATLAS detector at the LHC. *Phys. Lett.*, B716:1–29, 2012. doi: 10.1016/j.physletb.2012.08.
1847 020.
- 1848 [29] S. Chatrchyan et al. Observation of a new boson at a mass of 125 GeV with the CMS experiment
1849 at the LHC. *Phys. Lett.*, B716:30–61, 2012. doi: 10.1016/j.physletb.2012.08.021.
- 1850 [30] Observation of $H \rightarrow b\bar{b}$ decays and VH production with the ATLAS detector. Technical Report
1851 ATLAS-CONF-2018-036, CERN, Geneva, Jul 2018. URL <http://cds.cern.ch/record/2630338>.
- 1852 [31] Observation of Higgs boson decay to bottom quarks. Technical Report arXiv:1808.08242. CMS-
1853 HIG-18-016-003, CERN, Geneva, Aug 2018. URL <https://cds.cern.ch/record/2636067>. *
1854 Temporary entry *.
- 1855 [32] A. M. Sirunyan et al. Observation of the Higgs boson decay to a pair of τ leptons with the CMS
1856 detector. *Phys. Lett.*, B779:283–316, 2018. doi: 10.1016/j.physletb.2018.02.004.
- 1857 [33] A. M. Sirunyan et al. Observation of $t\bar{t}H$ production. *Phys. Rev. Lett.*, 120:231801, 2018. doi:
1858 10.1103/PhysRevLett.120.231801.
- 1859 [34] M. Aaboud et al. Observation of Higgs boson production in association with a top quark pair at
1860 the LHC with the ATLAS detector. 2018.
- 1861 [35] Measurement of the Higgs boson mass in the $H \rightarrow ZZ^* \rightarrow 4\ell$ and $H \rightarrow \gamma\gamma$ channels with
1862 $\sqrt{s}=13\text{TeV}$ pp collisions using the ATLAS detector. Technical Report ATLAS-CONF-2017-046,
1863 CERN, Geneva, Jul 2017. URL <http://cds.cern.ch/record/2273853>.
- 1864 [36] G. Aad et al. Combined Measurement of the Higgs Boson Mass in pp Collisions at $\sqrt{s} = 7$
1865 and 8 TeV with the ATLAS and CMS Experiments. *Phys. Rev. Lett.*, 114:191803, 2015. doi:
1866 10.1103/PhysRevLett.114.191803.
- 1867 [37] M. Aaboud et al. Measurement of the W -boson mass in pp collisions at $\sqrt{s} = 7$ TeV with the
1868 ATLAS detector. *Eur. Phys. J.*, C78(2):110, 2018. doi: 10.1140/epjc/s10052-017-5475-4.

- 1869 [38] R. Nisius. Measurements of the top quark mass with the ATLAS detector. *PoS*, EPS-HEP2017:
1870 453, 2017. doi: 10.22323/1.314.0453.
- 1871 [39] Measurement of the top quark mass with muon+jets final states in pp collisions at $\sqrt{s} = 13$ TeV.
1872 Technical Report CMS-PAS-TOP-16-022, CERN, Geneva, 2017. URL <http://cds.cern.ch/record/2255834>.
- 1873 [40] CERN. The high-luminosity lhc. <http://cds.cern.ch/record/2114693>, 2015. Accessed
1874 2018/01/11.
- 1876 [41] T. Koffas. ATLAS Higgs physics prospects at the high luminosity LHC. *PoS*, ICHEP2016:426,
1877 2017.
- 1878 [42] A. M. Henriques Correia. The ATLAS Tile Calorimeter. Technical Report ATL-TILECAL-PROC-
1879 2015-002, CERN, Geneva, Mar 2015. URL <https://cds.cern.ch/record/2004868>.
- 1880 [43] ATLAS liquid argon calorimeter: Technical design report. 1996.
- 1881 [44] M. Cacciari, G. P. Salam, and G. Soyez. The Catchment Area of Jets. *JHEP*, 04:005, 2008. doi:
1882 10.1088/1126-6708/2008/04/005.
- 1883 [45] Optimisation of the ATLAS b -tagging performance for the 2016 LHC Run. Technical Report ATL-
1884 PHYS-PUB-2016-012, CERN, Geneva, Jun 2016. URL <https://cds.cern.ch/record/2160731>.
- 1885 [46] Commissioning of the ATLAS high-performance b -tagging algorithms in the 7 TeV collision data.
1886 Technical Report ATLAS-CONF-2011-102, CERN, Geneva, Jul 2011. URL <https://cds.cern.ch/record/1369219>.
- 1888 [47] G. Aad et al. Expected Performance of the ATLAS Experiment - Detector, Trigger and Physics.
1889 2009.
- 1890 [48] A. Ruiz-Martinez and A. Collaboration. The Run-2 ATLAS Trigger System. Technical Report ATL-
1891 DAQ-PROC-2016-003, CERN, Geneva, Feb 2016. URL <https://cds.cern.ch/record/2133909>.
- 1892 [49] S. D. Ellis and D. E. Soper. Successive combination jet algorithm for hadron collisions. *Phys. Rev.*,
1893 D48:3160–3166, 1993. doi: 10.1103/PhysRevD.48.3160.
- 1894 [50] M. Wobisch and T. Wengler. Hadronization corrections to jet cross-sections in deep inelastic
1895 scattering. In *Monte Carlo generators for HERA physics. Proceedings, Workshop, Hamburg,*
1896 *Germany, 1998-1999*, pages 270–279, 1998. URL https://inspirehep.net/record/484872/files/arXiv:hep-ph_9907280.pdf.
- 1898 [51] M. Cacciari, G. P. Salam, and G. Soyez. The Anti- $k(t)$ jet clustering algorithm. *JHEP*, 04:063,
1899 2008. doi: 10.1088/1126-6708/2008/04/063.
- 1900 [52] A. Altheimer et al. Boosted objects and jet substructure at the LHC. Report of BOOST2012, held
1901 at IFIC Valencia, 23rd-27th of July 2012. *Eur. Phys. J.*, C74(3):2792, 2014. doi: 10.1140/epjc/s10052-014-2792-8.

- 1903 [53] G. A. et al. Performance of jet substructure techniques for large- r jets in proton-proton collisions
 1904 at $\sqrt{s} = 7$ tev using the atlas detector. *Journal of High Energy Physics*, 2013(9), Sep 2013. doi:
 1905 10.1007/JHEP09(2013)076. URL [https://doi.org/10.1007/JHEP09\(2013\)076](https://doi.org/10.1007/JHEP09(2013)076).
- 1906 [54] J. Thaler and K. Van Tilburg. Identifying Boosted Objects with N-subjettiness. *JHEP*, 03:015,
 1907 2011. doi: 10.1007/JHEP03(2011)015.
- 1908 [55] C. Chen. New approach to identifying boosted hadronically-decaying particle using jet substruc-
 1909 ture in its center-of-mass frame. *Phys. Rev.*, D85:034007, 2012. doi: 10.1103/PhysRevD.85.
 1910 034007.
- 1911 [56] J. M. Butterworth, A. R. Davison, M. Rubin, and G. P. Salam. Jet substructure as a new Higgs
 1912 search channel at the LHC. *Phys. Rev. Lett.*, 100:242001, 2008. doi: 10.1103/PhysRevLett.100.
 1913 242001.
- 1914 [57] I. Hinchliffe, A. Kotwal, M. L. Mangano, C. Quigg, and L.-T. Wang. Luminosity goals for a 100-TeV
 1915 pp collider. *Int. J. Mod. Phys.*, A30(23):1544002, 2015. doi: 10.1142/S0217751X15440029.
- 1916 [58] N. Arkani-Hamed, T. Han, M. Mangano, and L.-T. Wang. Physics opportunities of a 100 TeV
 1917 protonproton collider. *Phys. Rept.*, 652:1–49, 2016. doi: 10.1016/j.physrep.2016.07.004.
- 1918 [59] C. Helsens. Fcc/he-lhc physics/performance studies towards the cdr. URL: https://indico.cern.ch/event/675588/contributions/2765045/attachments/1572548/2484309/Clement_FCC.pdf, 2017.
- 1921 [60] T. an FCC-hh Detector Magnet System. E. bielert, 2018. URL <https://ep-news.web.cern.ch/content/towards-fcc-hh-detector-magnet-system>.
- 1923 [61] J. Faltova. Electromagnetic calorimeter using lar technology for fcc-hh. URL: https://indico.cern.ch/event/556692/contributions/2465166/attachments/1468150/2272205/ecal_fccBerlin.pdf, 2017.
- 1926 [62] A. Zaborowska. Electromagnetic calorimetry based on liquid argon for the fcc-hh experi-
 1927 ments. URL: https://indico.cern.ch/event/656491/contributions/2923535/attachments/1631506/2601159/FCChh_LArCalo_Zaborowska.pdf, 2018.
- 1929 [63] C. Neubser. Performance studies and requirements on the calorimeters for a fcc-hh ex-
 1930 periment. URL: <https://indico.ihep.ac.cn/event/6387/session/14/contribution/117/material/slides/0.pdf>, 2017.
- 1932 [64] J. Baglio, A. Djouadi, R. Grber, M. M. Mhlleitner, J. Quevillon, and M. Spira. The measurement
 1933 of the Higgs self-coupling at the LHC: theoretical status. *JHEP*, 04:151, 2013. doi: 10.1007/
 1934 JHEP04(2013)151.
- 1935 [65] M. Aaboud et al. Search for pair production of Higgs bosons in the $b\bar{b}b\bar{b}$ final state using proton–
 1936 proton collisions at $\sqrt{s} = 13$ TeV with the ATLAS detector. *Phys. Rev.*, D94(5):052002, 2016. doi:
 1937 10.1103/PhysRevD.94.052002.

- 1938 [66] A. M. Sirunyan et al. Search for a massive resonance decaying to a pair of Higgs bosons in the
 1939 four b quark final state in proton-proton collisions at $\sqrt{s} = 13$ TeV. 2017.
- 1940 [67] G. Aad et al. Searches for Higgs boson pair production in the $hh \rightarrow bb\tau\tau, \gamma\gamma WW^*, \gamma\gamma bb, bbbb$
 1941 channels with the ATLAS detector. *Phys. Rev.*, D92:092004, 2015. doi: 10.1103/PhysRevD.92.
 1942 092004.
- 1943 [68] A. M. Sirunyan et al. Search for Higgs boson pair production in events with two bottom quarks and
 1944 two tau leptons in proton-proton collisions at $\sqrt{s} = 13$ TeV. 2017.
- 1945 [69] M. Aaboud et al. A search for resonant and non-resonant Higgs boson pair production in the
 1946 $b\bar{b}\tau^+\tau^-$ decay channel in pp collisions at $\sqrt{s} = 13$ TeV with the ATLAS detector . Technical Report
 1947 arXiv:1808.00336, CERN, Geneva, Aug 2018. URL <https://cds.cern.ch/record/2632994>. *
 1948 Temporary entry *.
- 1949 [70] V. Khachatryan et al. Search for two Higgs bosons in final states containing two photons and
 1950 two bottom quarks in proton-proton collisions at 8 TeV. *Phys. Rev.*, D94(5):052012, 2016. doi:
 1951 10.1103/PhysRevD.94.052012.
- 1952 [71] G. Aad et al. Search For Higgs Boson Pair Production in the $\gamma\gamma b\bar{b}$ Final State using pp Collision
 1953 Data at $\sqrt{s} = 8$ TeV from the ATLAS Detector. *Phys. Rev. Lett.*, 114(8):081802, 2015. doi:
 1954 10.1103/PhysRevLett.114.081802.
- 1955 [72] A. M. Sirunyan et al. Search for resonant and nonresonant Higgs boson pair production in the
 1956 $bb\lnu\lnu$ final state in proton-proton collisions at $\sqrt{s} = 13$ TeV. 2017.
- 1957 [73] M. Aaboud et al. Combination of searches for heavy resonances decaying into bosonic and
 1958 leptonic final states using 36 fb^{-1} of proton-proton collision data at $\sqrt{s} = 13$ TeV with the ATLAS
 1959 detector. 2018.
- 1960 [74] G. Aad and t. . others.
- 1961 [75] J. K. Behr, D. Bortoletto, J. A. Frost, N. P. Hartland, C. Issever, and J. Rojo. Boosting Higgs pair
 1962 production in the $b\bar{b}b\bar{b}$ final state with multivariate techniques. *Eur. Phys. J.*, C76(7):386, 2016. doi:
 1963 10.1140/epjc/s10052-016-4215-5.
- 1964 [76] S. Banerjee, C. Englert, M. L. Mangano, M. Selvaggi, and M. Spannowsky. $hh + \text{jet}$ production at
 1965 100 TeV. *Eur. Phys. J.*, C78(4):322, 2018. doi: 10.1140/epjc/s10052-018-5788-y.
- 1966 [77] N. P. Hartland. Double Higgs production from $HH \rightarrow (b\bar{b})(b\bar{b})$ at a 100 TeV hadron collider. *PoS*,
 1967 DIS2016:115, 2016.
- 1968 [78] S. V. Chekanov, M. Beydler, A. V. Kotwal, L. Gray, S. Sen, N. V. Tran, S. S. Yu, and J. Zuzelski.
 1969 Initial performance studies of a general-purpose detector for multi-TeV physics at a 100 TeV pp
 1970 collider. *JINST*, 12(06):P06009, 2017. doi: 10.1088/1748-0221/12/06/P06009.

- 1971 [79] S. Chekanov. Boosted jets in high-granularity calorimeter at a 100 TeV pp collider. BOOST 2017,
 1972 2017.
- 1973 [80] S. Chekanov. Physics requirements for a Hadron Calorimeter for a 100 TeV proton-proton collider.
 1974 FCC week 2015, 2015.
- 1975 [81] S. Chekanov. Simulation of a high-granular hadronic calorimeter for multi-TeV physics. FCC week
 1976 2016, 2016.
- 1977 [82] J. Alwall, M. Herquet, F. Maltoni, O. Mattelaer, and T. Stelzer.
- 1978 [83] T. Sjostrand, S. Mrenna, and P. Z. Skands. A Brief Introduction to PYTHIA 8.1. *Comput. Phys.*
 1979 *Commun.*, 178:852–867, 2008. doi: 10.1016/j.cpc.2008.01.036.
- 1980 [84] J. de Favereau, C. Delaere, P. Demin, A. Giammanco, V. Lematre, A. Mertens, and M. Selvaggi.
 1981 DELPHES 3, A modular framework for fast simulation of a generic collider experiment. *JHEP*, 02:
 1982 057, 2014. doi: 10.1007/JHEP02(2014)057.
- 1983 [85] E. Boos et al. Generic user process interface for event generators. In *Physics at TeV colliders.*
 1984 *Proceedings, Euro Summer School, Les Houches, France, May 21-June 1, 2001*, 2001. URL
 1985 <http://lss.fnal.gov/archive/preprint/fermilab-conf-01-496-t.shtml>.
- 1986 [86] M. Cacciari, G. P. Salam, and G. Soyez. FastJet User Manual. *Eur. Phys. J.*, C72:1896, 2012. doi:
 1987 10.1140/epjc/s10052-012-1896-2.
- 1988 [87] D. Buskulic et al. Performance of the ALEPH detector at LEP. *Nucl. Instrum. Meth.*, A360:481–506,
 1989 1995. doi: 10.1016/0168-9002(95)00138-7.
- 1990 [88] Particle-Flow Event Reconstruction in CMS and Performance for Jets, Taus, and MET. Technical
 1991 Report CMS-PAS-PFT-09-001, CERN, Geneva, Apr 2009. URL <http://cds.cern.ch/record/1194487>.
- 1993 [89] FCC study group. Fccsw. <https://github.com/HEP-FCC/FCCSW>, 2018.
- 1994 [90] G. Barrand et al. GAUDI - A software architecture and framework for building HEP data processing
 1995 applications. *Comput. Phys. Commun.*, 140:45–55, 2001. doi: 10.1016/S0010-4655(01)00254-5.
- 1996 [91] F. Gaede, B. Hegner, and P. Mato. Podio: An event-data-model toolkit for high energy physics
 1997 experiments. *Journal of Physics: Conference Series*, 898(7):072039, 2017. URL <http://stacks.iop.org/1742-6596/898/i=7/a=072039>.
- 1999 [92] FCC-hh study group. Eventproducer. <https://github.com/FCC-hh-framework/EventProducer>,
 2000 2018.
- 2001 [93] N. D. Christensen and C. Duhr. FeynRules - Feynman rules made easy. *Comput. Phys. Commun.*,
 2002 180:1614–1641, 2009. doi: 10.1016/j.cpc.2009.02.018.

- 2003 [94] T. general Two-Higgs-Doublet Model. C. degrande, c. duhr, m. herquet, 2018. URL <http://feynrules.irmpl.ac.be/wiki/2HDM>.
- 2004
- 2005 [95] C. Degrande. Automatic evaluation of UV and R2 terms for beyond the Standard Model La-
2006 grangians: a proof-of-principle. *Comput. Phys. Commun.*, 197:239–262, 2015. doi: 10.1016/j.
2007 cpc.2015.08.015.
- 2008 [96] H. E. Haber and O. Stl. New LHC benchmarks for the \mathcal{CP} -conserving two-Higgs-doublet
2009 model. *Eur. Phys. J.*, C75(10):491, 2015. doi: 10.1140/epjc/s10052-015-3697-x, 10.1140/epjc/
2010 s10052-016-4151-4. [Erratum: Eur. Phys. J.C76,no.6,312(2016)].
- 2011 [97] D. de Florian et al. Handbook of LHC Higgs Cross Sections: 4. Deciphering the Nature of the
2012 Higgs Sector. 2016. doi: 10.23731/CYRM-2017-002.
- 2013 [98] M. Grazzini, G. Heinrich, S. Jones, S. Kallweit, M. Kerner, J. M. Lindert, and J. Mazzitelli. Higgs
2014 boson pair production at NNLO with top quark mass effects. *JHEP*, 05:059, 2018. doi: 10.1007/
2015 JHEP05(2018)059.
- 2016 [99] C. Patrignani et al. Review of Particle Physics. *Chin. Phys.*, C40(10):100001, 2016. doi: 10.1088/
2017 1674-1137/40/10/100001.
- 2018 [100] M. Aaboud et al. Search for pair production of Higgs bosons in the $b\bar{b}b\bar{b}$ final state using proton-
2019 proton collisions at $\sqrt{s} = 13$ TeV with the ATLAS detector. 2018.
- 2020 [101] C. Helsens. Heavy resonances at 100tev, 2018. URL https://indico.cern.ch/event/704428/contributions/2957537/attachments/1627728/2594323/Resonances_FCC_hh_helsens.pdf.
- 2021

2022 Appendix A

2023 Jet radius discussion

2024 It is important to discuss if the radius of the jet that is used to reconstruct the boosted Higgs boson
 2025 candidates ($R = 0.8$) is the appropriate one. The question arises because in ATLAS boosted objects
 2026 with $p_T \sim 200$ GeV are reconstructed using $R = 1.0$ jets. In this work, we work with a CM energy of 100
 2027 TeV and require that the two leading jets have $p_T > 200$ GeV and use jets with $R = 0.8$. It is necessary
 2028 to understand if these jets are large enough to fully reconstruct the Higgs candidates.

2029 As a first approximation we compute the angle between the b quarks produced by the decay of
 2030 a Higgs boson. We assume that the b quarks are massless and that the Higgs moves only in the
 2031 transverse plane (perpendicular to the beam pipe) such that it has no longitudinal momentum and the
 2032 angle between the b quarks is given by $\Delta\phi$. For $p_T(\text{Higgs}) = 200$ GeV, we get $\Delta\phi(b, \bar{b}) = 1.1$ which is
 2033 smaller than the jet's diameter (1.6) and therefore the two b quarks can both be contained inside the jet
 2034 and the Higgs boson fully reconstructed.

2035 Another test we can make is to compute the
 2036 ΔR between the b quarks coming from the lead-
 2037 ing Higgs candidate with p_T larger than a given
 2038 value using truth level information. In figure A.1
 2039 we show the distribution of $\Delta R(b, \bar{b})$ for p_T of
 2040 the leading Higgs candidate larger than 200 GeV
 2041 (solid blue) and 300 GeV (solid black). To obtain
 2042 the dashed histograms we apply the p_T to both
 2043 Higgs candidates. The integral of the histograms
 2044 between 0 and 1.6 gives an estimate of the frac-
 2045 tion of signal we keep if we apply these p_T cuts.
 2046 For $p_T(h_1) > 200(300)$ GeV we get that 93(98) %
 2047 of the signal has b quarks with $\Delta R < 1.6$ and
 2048 therefore can be fully reconstructed using a jet with $R = 0.8$.

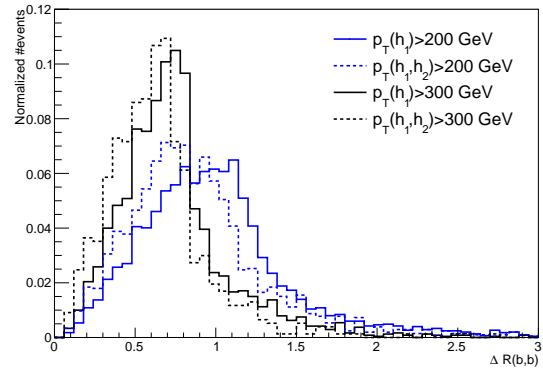


Figure A.1: $\Delta R(b, \bar{b})$ distributions for $p_T(h_1) > 200/300$ GeV (solid blue/black) and for $p_T(h_1, h_2) > 200/300$ GeV (dashed blue/black).

2049 **Appendix B**

2050 **Additional background processes**

2051 In this section we discuss the importance of additional background processes and estimate how they
2052 influence the analysis. In particular, we investigate backgrounds involving Higgs bosons. We consider
2053 the $t\bar{t}h$ and $h + 0/1/2 j$ processes. The effective cross section, efficiency and expected number of events
2054 for an integrated luminosity of $\mathcal{L} = 30 \text{ ab}^{-1}$ are summarized in table B.1. Including these backgrounds
2055 in the analysis leads to a decrease in the significance of 0.26%, which we consider to be a very small
2056 effect. Therefore, neglecting these backgrounds is a safe assumption.

Table B.1: Effective cross section ($\sigma \times \text{BR} \times \text{k-factor}$), efficiency and expected number of events for $\mathcal{L} = 30 \text{ ab}^{-1}$ for the $t\bar{t}h + 0/1 j(h \rightarrow b\bar{b})$ and $h + 0/1/2 j(h \rightarrow b\bar{b})$ backgrounds.

Process	$\sigma \times \text{BR} \times \text{k-factor} [\text{pb}]$	Efficiency [%]	Expected nb. events ($\mathcal{L} = 30 \text{ ab}^{-1}$)
$t\bar{t}h + 0/1 j(h \rightarrow b\bar{b})$	31.86	0.089	8.5×10^5
$h + 0/1/2 j(h \rightarrow b\bar{b})$	1286.52	0.0041	1.6×10^6

2057 In addition, we also estimate the error associated with not considering the a sample of $4b + j$ with
2058 $p_T(j) < 200 \text{ GeV}$. In order to do so, we generate a sample with 110k events of $4b + j$ with $(30 < p_T(j) <$
2059 $200) \text{ GeV}$. The cross section is $\sigma = 7450 \text{ pb}$. No event goes through the cuts $p_T(\text{leading jet}) > 300$
2060 GeV and $p_T(\text{Higgs pair}) > 100 \text{ GeV}$. However, if we assume that 1 events goes through the cuts (which
2061 corresponds to a very conservative $9.09 \times 10^{-4}\%$ efficiency) we have an expected number of events of
2062 2.03×10^6 for an integrated luminosity of $\mathcal{L} = 30 \text{ ab}^{-1}$. If we include this background, the significance
2063 decreases by 0.22% which is a very small effect. Therefore, it is safe to neglect this background.

2064 **Appendix C**

2065 **Softdrop mass**

2066 It is noticeable in the softdrop mass spectrum of both Higgs candidates (for signal and backgrounds) the
2067 existence an atypical peak close to zero. In this section we explain the origin of this feature.

2068 We believe that the peak close to zero corresponds to Higgs candidates ($R = 0.8$ jets) that do not
2069 contain both b quarks from the Higgs decay. The plot that support this conclusion is shown in figure
2070 C.1. It shows the correlation between the maximum ΔR between the Higgs candidate jet and one of
2071 the b quarks (y axis) and the jet's mass (x axis). The horizontal line corresponds to $\Delta R = 0.8$. For
2072 small masses (< 80 GeV) the maximum ΔR is usually larger than 0.8 which means that at least one
2073 of the b quarks is not contained in the jet's cone. When applying the soft drop procedure to these jets,
2074 soft radiation is removed and we are left with a single b quark. The mass of b quarks is ~ 5 GeV and
2075 therefore we get a peak at this mass.

2076 In practice, this does not affect our analysis because we place a mass window cut around the Higgs
2077 boson mass and therefore the low mass peak is removed. Nonetheless, the study presented here is
2078 extremely important because it helps rule out possible malfunctions of the soft drop algorithm and gives
2079 us confidence that we understand exactly what is happening.

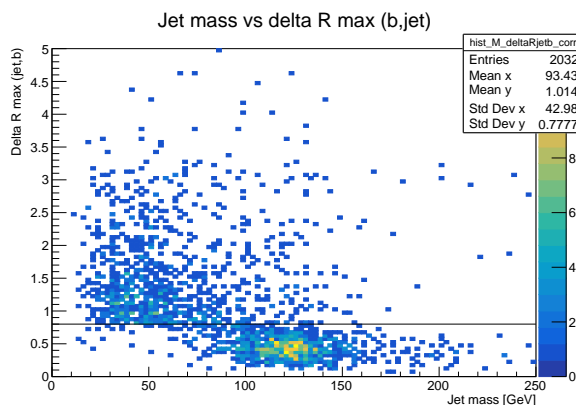


Figure C.1: Correlation between the maximum ΔR between the Higgs candidate jet and one of the b quarks (y axis) and the jet's mass (x axis). The horizontal line corresponds to $\Delta R = 0.8$.

2080 **Appendix D**

2081 **Samples generation: parameters**

2082 In this appendix we provide we list the values of parameters used in MadGraph (section D.1) and Pythia
2083 (section D.2) to generate the samples used in this work.

2084 **D.1 MadGraph**

2085 The MadGraph5 level cuts are summarized in table D.1. We show only the most relevant cuts for this
2086 analysis: the minimum p_T of light and b quarks, $p_{T,j}^{\min}$ and $p_{T,b}^{\min}$, the maximum pseudorapidity range for
2087 light and b quarks, η_j^{\max} and η_b^{\max} and the ΔR separation between two light quarks, $\Delta R(jj)$, two b
2088 quarks, $\Delta R(bb)$, and between a light and b quarks, $\Delta R(jb)$. The $xqcut$ parameter is a measure of the
2089 required parton separation at Madgraph level. Whenever MadGraph produces two partons, i and j ,
2090 we define the distance between them as $\sqrt{2 * \min(p_{T,i}, p_{T,j}) [\cosh(\eta_i - \eta_j) - \cos(\phi_i - \phi_j)]}$. If the value
2091 of this expression is smaller than the specified value of $xqcut$ then we do not generate the event. The
2092 $bwcutoff$ parameter defines what is considered to be on-shell s-channel resonances. The H_T variable
2093 is the scalar sum of the p_T of all truth level partons, including b quarks.

2094 **D.2 Pythia**

2095 The settings for jet matching can be found in table D.2 under the corresponding samples' columns. We
2096 perform the jet matching procedure (merge=on) using the MLM matching scheme and the appropriate
2097 algorithm for a parton level process generated in MadGraph (scheme=1). We do not read the matching
2098 parameters from the MadGraph file (setMad=off) because this option is not available for these files. The
2099 size of the cone drawn around the jet's center, the maximum pseudorapidity and the maximum number
2100 of jets to be matched are given by coneRadius, etaJetMax and nJetMax, respectively. The cone radius
2101 is set to one. The maximum allowed pseudorapidity of jets is ten which is a much loser cut than the
2102 acceptance of any current detector. The maximum number of jets is set to four for the jj+0/1/2 j and to
2103 two for the $t\bar{t}$ +0/1/2 j. The qCut parameter defines the k_T scale for merging shower products into jets.

Table D.1: Generator (MadGraph5) level cuts for the signal and background samples.

MadGraph5	SM ($h \rightarrow b\bar{b}$) & BSM hh	hh & 4b+j (QCD)	4b+j (QCD+EWK)	4b+j (EWK)	jj+0/1/2 j	tt+0/1/2 j
$p_{T,j}^{\min}, p_{T,b}^{\min}$ [GeV]	0	200; 30 500; 30	20; 15	20; 15	20; 5	5; 5
$\eta_j^{\max}, \eta_b^{\max}$	—	5; 5	5; 3	5; 3	8; 8	8; 8
$\Delta R(jj), \Delta R(bb), \Delta R(jb)$	0.001	0.4; 0.1; 0.3	0.4; 0.2; 0.4	0.4; 0.2; 0.4	0; 0.001; 0.001	0.001
xqcut [GeV]	0	0	0	0	20	60
bwcutoff [GeV]	30	15	15	15	30	30
H_T	—	—	—	—	0 – 500 500 – 1k 1k – 2k 2k – 4k 4k – 7.2k 7.2k – 15k 15k – 25k 25k – 35k 35k – 100k	—

Table D.2: Pythia settings for the signal and background samples.

Pythia	hh ($h \rightarrow b\bar{b}$)	4b+j	jj+0/1/2 j	tt+0/1/2 j
Relevant settings	25:onMode=off 25:onIfAny= 5 -5	—	Jet matching: merge=on scheme=1 setMad=off coneRadius=1.0 etaJetMax=10 nJetMax=4 qCut=30	Jet matching: merge=on scheme=1 setMad=off coneRadius=1.0 etaJetMax=10 nJetMax=2 qCut=60
Description	Turn on the $h \rightarrow b\bar{b}$ decay for the undecayed Higgs, in the case of the SM sample, or for both Higgs in the case of the BSM samples.	—	Set the parameters for jet matching (a detailed description can be found in the text).	

2104 **Appendix E**

2105 **Cutflow tables**

2106 In this appendix we collect the cutflow tables for the baseline and optimized analysis, for particle flow
2107 and calorimeter jets and for all detector configurations that were tested. The efficiencies of the cuts are
2108 shown for all cuts. The expected number of events for an integrated luminosity of $\mathcal{L} = 30 \text{ ab}^{-1}$ is also
2109 shown for some key cuts.

Table E.1: oi

Configuration	PF jets		HCAL jets	
	Baseline	Optimized	Baseline	Optimized
ATLAS				
ATLAS gran.				
ATLAS gran. $\eta \times 4$				
FCC gran. $\phi/2$				
FCC				
FCC gran. $\eta, \phi \times 2$				

Table E.2: α_i

Selection [ATLAS]	$hh \rightarrow b\bar{b}b\bar{b}$ (SM)	$hh \rightarrow b\bar{b}b\bar{b}$ (DM mediator)	$hh \rightarrow b\bar{b}b\bar{b}$ (2HDM)	$4b + j$	$jj + 0/1/2j$	$t\bar{t}$
Gen level	100	100	100	100	100	100
N(b-tags)						
$p_T(j_1, j_2) \geq 200$ GeV						
$p_T(j_1) \geq 400$ GeV						
$p_T(j_2) \geq 350$ GeV						
$p_T(j_1 + j_2) \geq 100$ GeV						
$\tau_{21}(j_1) < 0.55$						
$\tau_{21}(j_2) < 0.55$						
$FW2(j_1) > 0.2$						
$(100 < M_{SD}(j1) < 135)$ GeV						
$(100 < M_{SD}(j2) < 135)$ GeV						

2110 **Appendix F**

2111 **Extra plots**

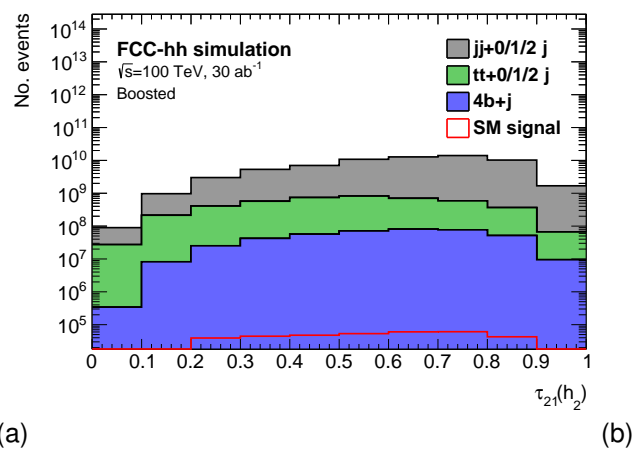


Figure F.1: . The histograms are normalized to $\mathcal{L} = 30 \text{ ab}^{-1}$.